UNIVERSITY
OF MICHIGAN
JUN 11 1956
CHEMISTRY
LIBRARY

Journal of Research

of the

National Bureau of Standards

APRIL 1956

VOLUME 56 NUMBER 4

U. S. DEPARTMENT OF COMMERCE
Sinclair Weeks, Secretary
NATIONAL BUREAU OF STANDARDS
A. V. Astin, Director

APRIL • 1953
VOLUME • 50
NUMBER • 4

JOURNAL OF RESEARCH
of the
NATIONAL BUREAU OF STANDARDS

PERIODICALS OF THE NATIONAL BUREAU OF STANDARDS
(Published monthly)

The National Bureau of Standards is engaged in fundamental and applied research in physics, chemistry, mathematics, and engineering. Projects are conducted in fifteen fields: electricity and electronics, optics and metrology, heat and power, atomic and radiation physics, chemistry, mechanics, organic and fibrous materials, metallurgy, mineral products, building technology, applied mathematics, data processing systems, cryogenic engineering, radio propagation, and radio standards. The Bureau has custody of the national standards of measurement and conducts research leading to the improvement of scientific and engineering standards and of techniques and methods of measurement. Testing methods and instruments are developed; physical constants and properties of materials are determined; and technical processes are investigated.

JOURNAL OF RESEARCH

The Journal presents research papers by authorities in the specialized fields of physics, mathematics, chemistry, and engineering. Complete details of the work are presented, including laboratory data, experimental procedures, and theoretical and mathematical analyses. Annual subscription: domestic, $4.00; $1.25 additional for foreign mailing.

TECHNICAL NEWS BULLETIN

Summaries of current research at the National Bureau of Standards are published each month in the Technical News Bulletin. The articles are brief, with emphasis on the results of research, chosen on the basis of their scientific or technologic importance. Lists of all Bureau publications during the preceding month are given, including Research Papers, Handbooks, Applied Mathematics Series, Building Materials and Structures Reports, Miscellaneous Publications, and Circulars. Each issue contains 12 or more two-column pages; illustrated. Annual subscription: domestic, $1.00; 35 cents additional for foreign mailing.

BASIC RADIO PROPAGATION PREDICTIONS

The Predictions provide the information necessary for calculating the best frequencies for communication between any two points in the world at any time during the given month. The data are important to all users of long-range radio communications and navigation, including broadcasting, airline, steamship, and wireless services, as well as to investigators of radio propagation and ionosphere. Each issue, covering a period of one month, is released three months in advance and contains 16 large pages, including pertinent charts, drawings, and tables. Annual subscription: domestic, $1.00; 25 cents additional for foreign mailing.

Order all publications from the Superintendent of Documents
U. S. Government Printing Office, Washington 25, D. C.

The printing of this publication has been approved by the Director of the Bureau of the Budget, May 12, 1953.

Journal of Research of the National Bureau of Standards Vol. 56, No. 4, April 1956 Research Paper 2663

New Descriptions and Analyses of the Third and Fourth Spectra of Zirconium, Zr III and Zr IV

C. C. Kiess

Recent observations of the spectra emitted by ionized zirconium atoms have added many new lines to the descriptions of these spectra and have led to revisions and extensions of their term structures. The low, even terms of Zr III arise in the electron configurations $4d^2$, $4d\ 5s$, and $5s^2$. Excitation of these states leads to higher terms of the $4d\ 5p$, $5s\ 5p$, $4d\ 5d$, $4d\ 6s$, $4d\ 4f$, $5s\ 5d$, $4d\ 6p$, $5s\ 6s$, $5s\ 4f$, and $5s\ 5g$ configurations. Most of the singlet and triplet terms from these configurations have now been established. Zeeman patterns from Massachusetts Institute of Technology plates have confirmed and corrected some of the classifications of earlier work. From the series-forming terms of Zr III the separation of the ground states of Zr III and Zr IV is calculated as 198590 cm^{-1}, corresponding to an ionization potential of 24.6 electron volts for the ion Zr^{2+}. In the doublet spectrum of Zr IV, which arises from the migration of the single electron outside the krypton shell, the terms from the $7s$, $6p$, $6d$, $5f$, $6f$, $5g$, and $6g$ electrons have been added to those already known. A mean value of 276970 cm^{-1} for the separation of the ground states of Zr IV and Zr V has been derived from three accordant values calculated from series of ^2S, $^2F°$, and ^2G terms. This corresponds to an ionization potential of 34.33 electron volts for Zr^{3+}.

1. Introduction

The new descriptions of the third and fourth spectra of zirconium, presented in this paper, have led to a reexamination of the analyses of their term structures published 25 years ago by Kiess and Lang [1].[1] Recent observations have more than doubled the number of lines known for these spectra at that time, and studies of the Zeeman effect have given unmistakable information about the classification of some of the lines. Preliminary reports [2] on the application of the new results to optical and astrophysical problems have already been made, and a paper has been published [3] with the new additions to and interpretations of the second spectrum, Zr II.

2. Experimental Procedure

Spectra of neutral and ionized zirconium atoms were obtained with a concave-grating spectrograph at the National Bureau of Standards, down to 1920 A in the ultraviolet. The grating, of 21-ft radius of curvature, was ruled by R. W. Wood [4] with 30,000 lines per inch. It is set up in a Wadsworth mounting and gives uniformly bright spectra throughout the accessible first and second orders, with a dispersion of 2 A/mm in the first order. The spectra were emitted by arcs and condensed-spark discharges in air between electrodes of the same zirconium metal that was used in the earlier work. Although of high purity this metal was found to contain very small amounts of silicon, titanium, iron, and hafnium. The arcs were operated at about 5 amp from 220-volt d-c mains. The sparks were excited by a battery of condensers, of 0.006-μf capacitance, charged from the high-voltage side of a transformer that stepped-up 110 volts a-c to 30,000 volts. The plates used to record the spectra were coated with EK 33 and SWR emulsions. Each exposure to a zirconium spectrum was juxtaposed to an exposure of the iron arc or to the spark between copper-silver electrodes to secure the necessary standards for the wavelength calculations.

For the extreme ultraviolet region of the spectra two sets of spectrograms were available for measurement, one obtained with the Carnegie vacuum spectrograph by J. C. Boyce while he was at the Massachusetts Institute of Technology, the other by A. G. Shenstone with the Princeton vacuum spectrograph. Both of these instruments have the same optical dimensions and produce spectra with dispersions of 4.25 A/mm in the first order from concave gratings ruled with 30,000 lines per inch. The results from these new measurements have confirmed and supplemented the descriptions of the ultraviolet spectra of Zr supplied by R. J. Lang for the Bureau's work of 25 years ago.

The MIT spectrograms were obtained from exposures to an arc operated at 8 amp between Zr-Ag electrodes in an atmosphere of commercial N_2, and cover the region from 2500 A down to 1100 A. The recorded spectra are mixtures of lines of zirconium, silver, nitrogen, carbon, and hafnium. The Princeton plates cover the region from 2200 A down to 513 A with exposures to a condensed-spark discharge between Zr electrodes in vacuum. On both sets of spectrograms appear lines of Zr I, Zr II, Zr III, and Zr IV. On the MIT plates the lines all exhibit uniform distributions of illumination along the slit of the spectrograph and differ only in their intensities and qualities of sharpness and diffuseness. On the Princeton plates, however, the lines exhibit distinctive differences of illumination along the slit of the spectrograph that permit them to be grouped according to the degree of ionization of their emitters: those of uniform intensity along the slit belong mostly to Zr I; lines of Zr II generally show illumination along the full length of the slit but are stronger

[1] Figures in brackets indicate the literature references at the end of this paper.

near the electrodes than in the zone midway between them; lines strong at the electrodes and directed like spear-points toward the center of the slit are characteristic of Zr III; while lines strong at the electrodes but tapering outward along the slit belong to Zr IV, and perhaps to Zr V. There are about 50 lines of this latter kind in the region between 900 and 600 A for which there is no place in Zr IV. It is very likely that they represent the excitation of the Kr-shell of the zirconium atom.

Preliminary values of the wavelengths derived from measurement of the MIT and Princeton plates were based on standards selected from lines of N, O, C, and H that appear as impurities in the spectra. These wavelengths were of sufficient accuracy to allow assignment of many of the lines to their multiplet structures. With more accurate values for energy levels calculated from lines longer than 2000 A, which were measured against better standards than those in the vacuum region, corrections were derived for the preliminary wavelengths longer than 1200 A. Nearly all the strong lines with wavelengths shorter than 1200 A appeared in the second and third orders, overlapping the first order from 2400 to 1000 A. Their apparent wavelengths, after being corrected as just described, were then divided by the appropriate factor to give the adopted values in the first-order spectrum.

There were also available for measurement plates of the Zeeman effect obtained under the direction of G. R. Harrison at MIT. Although most of the magnetic patterns appearing on these plates are of Zr I and Zr II lines, yet a few of them belong to lines of Zr III. These serve to verify and correct some of the earlier classifications. The results of the measurements are given below.

3. Results

3.1. Spectrum of Trebly Ionized Zirconium, Zr IV

In its unexcited state the neutral zirconium atom has four valence electrons in the configuration $4d^2\ 5s^2$ outside the krypton shell. The loss of three of these electrons through successive ionizations leaves a single 4*d*-electron to determine the term-structure of Zr IV. The early work on the analysis of Zr IV is summarized in the paper by Kiess and Lang cited above. The terms listed therein account for 12 lines of the spectrum if the term designated there as 7*s*, and now known to be incorrect, is excluded. In the present analysis the 39 lines given in table 1 are classified as combinations among the 21 terms recorded in table 2, and include all lines classified in the earlier investigations.

The terms of Zr IV, in table 2, are listed in the order of increasing energy indicated by the relative term-values in the second column and shown graphically in figure 1. In the fourth and fifth columns are given the absolute values of the terms, and the Rydberg denominators that were used in the simple Ritz formula $16R/[m+\alpha+(\beta/m^2)]^2$ to evaluate the running terms and the limits of the several series. Inspection of the table shows that three members have been found for the ^2S, ^2D, and $^2F^\circ$ series, and two members for the $^2P^\circ$ and ^2G series. The terms of the three-member series are accurately represented by the above formula with the appropriate values of α and β introduced into it. For the two-member series the terms were interpolated from the Princeton table for Rydberg's formula [5]. Table 3 shows that the values for the ground state $4p\ ^2D_{1\frac{1}{2}}$ of Zr IV given by the ^2S, $^2F^\circ$, and the nearly hydrogenic ^2G series are in close agreement, whereas the $^2P^\circ$ and ^2D series give much larger values. It is known from other spectra that series terms from

TABLE 1. *Classified lines of* Zr IV

Wavelengths longer than 2000 A, air values; vacuum values shorter than 2000 A.

Wavelengths	Intensities	Wave numbers	Term combinations
A		$K(cm^{-1})$	
2849. 19	10	35087. 41	$6p\ ^2P^\circ_{1\frac{1}{2}} - 6d\ ^2D_{1\frac{1}{2}}$
2832. 82	15	35290. 15	$6p\ ^2P^\circ_{1\frac{1}{2}} - 6d\ ^2D_{2\frac{1}{2}}$
2770. 44	5	36084. 72	$6p\ ^2P^\circ_{0\frac{1}{2}} - 6d\ ^2D_{1\frac{1}{2}}$
2286. 68	200	43718. 01	$5s\ ^2S_{0\frac{1}{2}} - 5p\ ^2P^\circ_{1\frac{1}{2}}$
2163. 63	500	46204. 06	$5s\ ^2S_{0\frac{1}{2}} - 5p\ ^2P^\circ_{1\frac{1}{2}}$
2125. 29	25	47037. 48	$4f\ ^2F^\circ_{2\frac{1}{2}} - 6d\ ^2D_{2\frac{1}{2}}$
2092. 40	150	47776. 76	$4f\ ^2F^\circ_{3\frac{1}{2}} - 5g\ ^2G_{4\frac{1}{2}}$
2091. 49	125	47797. 54	$4f\ ^2F^\circ_{2\frac{1}{2}} - 5g\ ^2G_{3\frac{1}{2}}$
1848. 06	10	54110. 8	$5d\ ^2D_{2\frac{1}{2}} - 5f\ ^2F^\circ_{3\frac{1}{2}}$
1846. 42	100	54158. 9	$5d\ ^2D_{2\frac{1}{2}} - 5f\ ^2F^\circ_{3\frac{1}{2}}$
1836. 14	100	54462. 1	$5d\ ^2D_{1\frac{1}{2}} - 5f\ ^2F^\circ_{2\frac{1}{2}}$
1607. 99	100	62189. 4	$5p\ ^2P^\circ_{1\frac{1}{2}} - 5d\ ^2D_{1\frac{1}{2}}$
1598. 98	200	62539. 9	$5p\ ^2P^\circ_{1\frac{1}{2}} - 5d\ ^2D_{2\frac{1}{2}}$
1546. 19	150	64675. 1	$5p\ ^2P^\circ_{0\frac{1}{2}} - 5d\ ^2D_{1\frac{1}{2}}$
1469. 50	100	68050. 4	$5p\ ^2P^\circ_{1\frac{1}{2}} - 6s\ ^2S_{0\frac{1}{2}}$
1441. 11	20	69391. 0	$4f\ ^2F^\circ_{3\frac{1}{2}} - 6g\ ^2G_{4\frac{1}{2}}$
1440. 68	18	69411. 7	$4f\ ^2F^\circ_{2\frac{1}{2}} - 6g\ ^2G_{3\frac{1}{2}}$
1417. 73	75	70535. 3	$5p\ ^2P^\circ_{0\frac{1}{2}} - 6s\ ^2S_{0\frac{1}{2}}$
1291. 77	1	77413. 1	$5d\ ^2D_{2\frac{1}{2}} - 6f\ ^2F^\circ_{3\frac{1}{2}}$
1290. 60	20	77483. 3	$5d\ ^2D_{2\frac{1}{2}} - 6f\ ^2F^\circ_{3\frac{1}{2}}$
1285. 94	15	77764. 1	$5d\ ^2D_{1\frac{1}{2}} - 6f\ ^2F^\circ_{2\frac{1}{2}}$
1219. 85	150	81977. 3	$4d\ ^2D_{1\frac{1}{2}} - 5p\ ^2P^\circ_{0\frac{1}{2}}$
1201. 77	250	83210. 6	$4d\ ^2D_{2\frac{1}{2}} - 5p\ ^2P^\circ_{1\frac{1}{2}}$
1183. 96	100	84462. 3	$4d\ ^2D_{1\frac{1}{2}} - 5p\ ^2P^\circ_{1\frac{1}{2}}$
864. 61	8	115659	$5p\ ^2P^\circ_{1\frac{1}{2}} - 7s\ ^2S_{0\frac{1}{2}}$
846. 42	4	118145	$5p\ ^2P^\circ_{0\frac{1}{2}} - 7s\ ^2S_{0\frac{1}{2}}$
823. 50	20	121433	$5p\ ^2P^\circ_{1\frac{1}{2}} - 6d\ ^2D_{1\frac{1}{2}}$
822. 09	20	121647	$5p\ ^2P^\circ_{1\frac{1}{2}} - 6d\ ^2D_{2\frac{1}{2}}$
806. 98	20	123919	$5p\ ^2P^\circ_{0\frac{1}{2}} - 6d\ ^2D_{1\frac{1}{2}}$
760. 18	8	131548	$5s\ ^2S_{0\frac{1}{2}} - 6p\ ^2P^\circ_{0\frac{1}{2}}$
754. 42	10	132552	$5s\ ^2S_{0\frac{1}{2}} - 6p\ ^2P^\circ_{1\frac{1}{2}}$
633. 66	20	157813	$4d\ ^2D_{2\frac{1}{2}} - 4f\ ^2F^\circ_{3\frac{1}{2}}$
633. 58	100	157833	$4d\ ^2D_{2\frac{1}{2}} - 4f\ ^2F^\circ_{3\frac{1}{2}}$
628. 68	100	159063	$4d\ ^2D_{1\frac{1}{2}} - 4f\ ^2F^\circ_{2\frac{1}{2}}$
589. 75			
588. 89	25	169563	$4d\ ^2D_{2\frac{1}{2}} - 6p\ ^2P^\circ_{1\frac{1}{2}}$
585. 43	20	169811	$4d\ ^2D_{1\frac{1}{2}} - 6p\ ^2P^\circ_{0\frac{1}{2}}$
	5	170815	$4d\ ^2D_{1\frac{1}{2}} - 6p\ ^2P^\circ_{1\frac{1}{2}}$
500. 22			
497. 12	2	199910	$4d\ ^2D_{2\frac{1}{2}} - 5f\ ^2F^\circ_{3\frac{1}{2}}$
	1	201117	$4d\ ^2D_{1\frac{1}{2}} - 5f\ ^2F^\circ_{2\frac{1}{2}}$

the p and d electrons usually lead to limits that are too large; but the difference of 18000 cm^{-1} between the values for the limit from the ^2D and ^2S series of Zr IV appears to be excessively large. The value adopted, therefore, for the ground state of Zr IV is the mean of the three accordant determinations, namely, 276970 cm^{-1}. It yields an ionization potential of 34.33 ev for the Zr^{3+} ion.

TABLE 2. *Terms of* Zr IV

Term designations	Relative term values	Term separations	Absolute term values	Rydberg denominators
$4d\,{}^2D_{1\frac{1}{2}}$	0	1250	276970	2. 5171
$4d\,{}^2D_{2\frac{1}{2}}$	1250		275720	2. 5228
$5s\,{}^2S_{0\frac{1}{2}}$	38258		238712	2. 7113
$5p\,{}^2P^\circ_{0\frac{1}{2}}$	81977	2484	194993	2. 9999
$5p\,{}^2P^\circ_{1\frac{1}{2}}$	84461		192509	3. 0192
$5d\,{}^2D_{1\frac{1}{2}}$	146651	350	130319	3. 6696
$5d\,{}^2D_{2\frac{1}{2}}$	147001		129969	3. 6745
$6s\,{}^2S_{0\frac{1}{2}}$	152511		124459	3. 7550
$4f\,{}^2F^\circ_{2\frac{1}{2}}$	159063	20	117907	3. 8579
$4f\,{}^2F^\circ_{3\frac{1}{2}}$	159083		117887	3. 8582
$6p\,{}^2P^\circ_{0\frac{1}{2}}$	169805	1005	107165	4. 0466
$6p\,{}^2P^\circ_{1\frac{1}{2}}$	170810		106160	4. 0657
$7s\,{}^2S_{0\frac{1}{2}}$	200121		76849	4. 7786
$5f\,{}^2F^\circ_{2\frac{1}{2}}$	201112	48	75858	4. 8097
$5f\,{}^2F^\circ_{3\frac{1}{2}}$	201160		75810	4. 8112
$6d\,{}^2D_{1\frac{1}{2}}$	205896	206	71074	4. 9689
$6d\,{}^2D_{2\frac{1}{2}}$	206102		70868	4. 9762
$5g\,{}^2G_{4\frac{1}{2},\,3\frac{1}{2}}$	206860		70110	5. 0030
$6f\,{}^2F^\circ_{2\frac{1}{2}}$	224415	69	52555	5. 7785
$6f\,{}^2F^\circ_{3\frac{1}{2}}$	224484		52486	5. 7823
$6g\,{}^2G_{4\frac{1}{2},\,3\frac{1}{2}}$	228474		48496	6. 0154

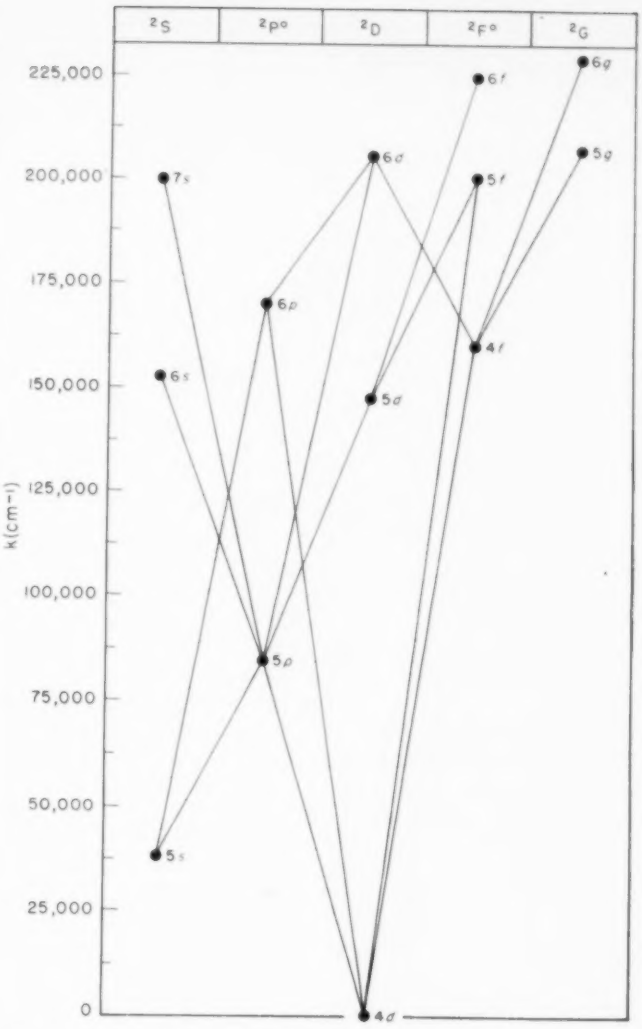

FIGURE 1. *Grotrian diagram of the terms and combinations of* Zr IV.

TABLE 3. *Series of* Zr IV

Evaluation of limit	Series				
	^2S	$^2P^\circ$	^2D	$^2F^\circ$	^2G
Limit term	$5p\,{}^2P^\circ$	$4d\,{}^2D$	$5p\,{}^2P^\circ$	$4d\,{}^2D$	$4f\,{}^2F^\circ$
Value of limit term	194735	281340	212850	276734	118396
Separation of limit term from ground state	81977	0	81977	0	159063
Absolute value of $4p\,{}^2D_{1\frac{1}{2}}$	276712	281340	294827	276734	277459
α	−2. 1364		−1. 5558	−0. 2577	
β	−3. 7706		−0. 0730	+1. 9133	

Adopted mean separation of the ground states of Zr V − Zr IV = **276970** cm^{-1}.
Ionization potential of Zr^{3+} = **34.33** ev.

TABLE 4. *Theoretical terms of* Zr III

Electron configurations	Terms												Limit in Zr IV
$4d\ 4d$	^1S		^1D		^1G			^3P		^3F			^2D
$4d\ 5s$			^1D						^3D				^2D
$5s\ 5s$	^1S												^2S
$4d\ 5p$		$^1P^\circ$	$^1D^\circ$	$^1F^\circ$				$^3P^\circ$	$^3D^\circ$	$^3F^\circ$			^2D
$5s\ 5p$		$^1P^\circ$						$^3P^\circ$					^2S
$4d\ 5d$	^1S	^1P	^1D	^1F	^1G		^3S	^3P	^3D	^3F	^3G		^2D
$4d\ 6s$			^1D						^3D				^2D
$4d\ 4f$		$^1P^\circ$	$^1D^\circ$	$^1F^\circ$	$^1G^\circ$	$^1H^\circ$		$^3P^\circ$	$^3D^\circ$	$^3F^\circ$	$^3G^\circ$	$^3H^\circ$	^2D
$5p\ 5p$	^1S		^1D					^3P					^2P
$5s\ 5d$			^1D						^3D				^2S
$5s\ 6s$	^1S						^3S						^2S
$4d\ 6p$		$^1P^\circ$	$^1D^\circ$	$^1F^\circ$				$^3P^\circ$	$^3D^\circ$	$^3F^\circ$			^2D
$5s\ 4f$				$^1F^\circ$						$^3F^\circ$			^2S
$5s\ 5g$					^1G						^3G		^2S

3.2. Spectrum of Doubly Ionized Zirconium, Zr

The term structure of the third spectrum of zirconium presented in the earlier work pertains only to that portion that is derived by addition of *ns*, *np*, *nd*, and *nf* electrons to the ground term $4d\ ^2D$ of Zr IV. However, other terms are to be expected from the addition of similar and also *ng* electrons to the excited states $5s\ ^2S$ and $5p\ ^2P^\circ$ of Zr IV. All of such theoretical terms that have been found in the present investigation are given in table 4, along with the previously known terms. The level-values of these terms are given in table 5, and all the lines classified as allowed transitions among the levels are listed in table 6. The relative positions of the Zr III terms are shown in figure 2. For some of the classified lines of Zr III, Zeeman patterns were found on the MIT spectrograms of zirconium. Although few in number these patterns verify some and correct other classifications of lines in the earlier work. They are given in table 7.

Among the terms in table 5 are several pairs that are parts of Rydberg series. No sequence of three or more members of a series has been found in Zr III. Nine such pairs of terms and their absolute values, as interpolated from the Princeton table, are recorded in table 8. By adding to each its distance above the ground state $4d\ ^3F_2$ of Zr III, a value for the gound state may be derived. Inspection of the table shows that also with Zr III the terms from configurations containing *p*-electrons give higher values for the ground state than do the others. The values for $4d\ ^3F_2$ from configurations with running *ns* and *nd* electrons are in good agreement, and have been averaged to give a mean value of 198590 cm^{-1} for the separation of the ground state of Zr III from that of Zr IV. This corresponds to an ionization potential of 24.6 ev.

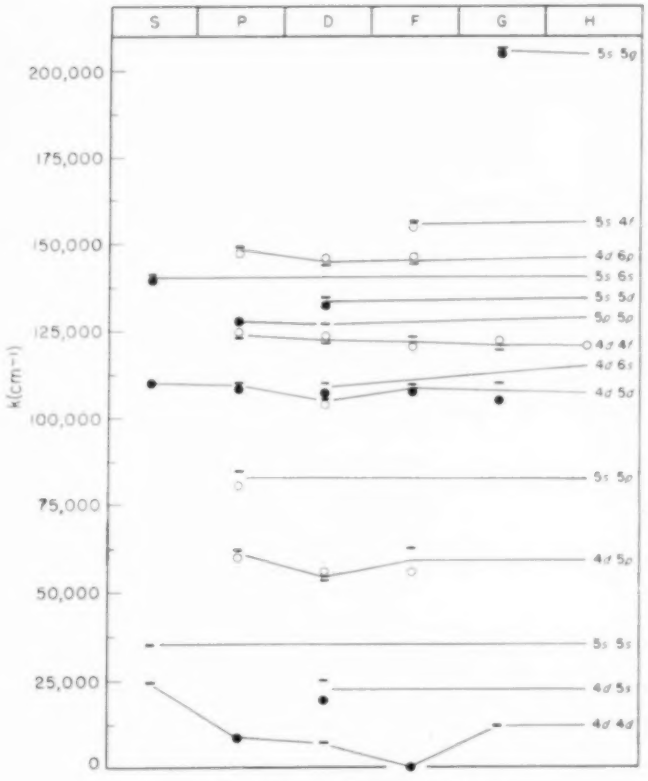

FIGURE 2. *Term diagram of* Zr III.

●, Even triplet terms; ○, odd triplet terms; —, singlet terms.

TABLE 5. *Terms of* Zr III

Electron configuration	Term	Relative term value	Term separation
$4d(^2D)4d$	$^3F_2$	0. 0	680. 5
	$^3F_3$	680. 5	805. 2
	$^3F_4$	1485. 7	
	^1D	5740. 9	
	$^3P_0$	8061. 50	263. 42
	$^3P_1$	8324. 92	512. 53
	$^3P_2$	8837. 45	
	$^1G_4$	11047. 90	
	$^1S_0$	23976. 48	

TABLE 5. *Terms of* Zr III—Continued

Electron configuration	Term	Relative term value	Term separation	Electron configuration	Term	Relative term value	Term separation
$4d(^2D)5s$	$^3D_1$	18397. 85	403. 97	$4d(^2D)4f$	$^3F^o_2$	120555	234
	$^3D_2$	18801. 82	730. 50		$^3F^o_3$	120789	485
	$^3D_3$	19532. 32			$^3F^o_4$	121274	
	$^1D_2$	25065. 04			$^3H^o_4$	120660	359
$5s(^2S)5s$	$^1S_0$	35500. 8			$^3H^o_5$	121019	
					$^3H^o_6$	-------	
$4d(^2D)5p$	$^3F^o_2$	55554. 78	519. 46		$^3G^o_3$	122017	584
	$^3F^o_3$	56074. 24	1606. 56		$^3G^o_4$	122601	292
	$^3F^o_4$	57680. 80			$^3G^o_5$	122893	
	$^3D^o_1$	55613. 40	821. 25		$^3D^o_1$	123336	68
	$^3D^o_2$	56434. 65	911. 18		$^3D^o_2$	123404	555
	$^3D^o_3$	57345. 83			$^3D^o_3$	123959	
	$^3P^o_0$	59944. 10	−247. 80		$^3P^o_0$	124800	
	$^3P^o_1$	59696. 30	659. 00		$^3P^o_1$	124683	−221
	$^3P^o_2$	60355. 30			$^3P^o_2$	124462	
	$^1D^o_2$	53646. 25			$^1H^o_5$	119791	
	$^1P^o_1$	62113. 90			$^1G^o_4$	119970	
	$^1F^o_3$	62587. 50			$^1D^o_2$	122081	
$5s(^2S)5p$	$^3P^o_0$	79436. 7	666. 3		$^1F^o_3$	123303	
	$^3P^o_1$	80103. 0	1450. 6		$^1P^o_1$	123906	
	$^3P^o_2$	81553. 6		$5p(^2P)5p$	$^3P_0$	125992	859
	$^1P^o_1$	83772. 2			$^3P_1$	126851	1746
$4d(^2D)5d$	$^3D_1$	103759. 4	346. 5		$^3P_2$	128597	
	$^3D_2$	104105. 9	772. 2		$^1D_2$	126558	
	$^3D_3$	104878. 1			$^1S_0$		
	$^3G_3$	104632. 4	556. 3	$5s(^2S)5d$	$^3D_1$	136792	211
	$^3G_4$	105188. 7	775. 8		$^3D_2$	137003	−4
	$^3G_5$	105964. 5			$^3D_3$	136999	
	$^3F_2$	107252. 5	567. 1		$^1D_2$	139441	
	$^3F_3$	107819. 6	494. 4		$^3S_1$	139377	
	$^3F_4$	108314. 0		$5s(^2S)6s$	$^1S_0$	141743	
	$^3P_0$	107634. 6	721. 9		$^3F^o_2$	144846	510
	$^3P_1$	108356. 5	911. 5		$^3F^o_3$	145356	−45
	$^3P_2$	109268. 0			$^3F^o_4$	145311	
	$^3S_1$	109597. 7			$^3D^o_1$	146112	281
	$^1D_2$	106499. 2			$^3D^o_2$	146393	514
	$^1F_3$	109095. 4			$^3D^o_3$	146907	
	$^1P_1$	109150. 9		$4d(^2D)6p$	$^3P^o_0$	147030	88
	$^1G_4$	110627. 0			$^3P^o_1$	147118	577
	$^1S_0$				$^3P^o_2$	147695	
$4d(^2D)6s$	$^3D_1$	105006. 3	313. 9		$^1D^o_2$	143945	
	$^3D_2$	105320. 2	980. 6		$^1F^o_3$	144175	
	$^3D_3$	106300. 8			$^1P^o_1$	148082	
	$^1D_2$	110134. 0		$5s(^2S)4f$	$^3F^o_2$	155174	
					$^3F^o_3$	155222	48
					$^3F^o_4$	155278	56
					$^1F^o_3$	156146	
				$5s(^2S)5g$	$^3G_3$	205290	
					$^3G_4$	205300	10
					$^3G_5$	205315	15
					$^1G_4$	206402	

TABLE 6. *Classified lines of* Zr III

Wavelength	Intensity	Wave number	Term combination	Wavelength	Intensity	Wave number	Term combination
A		*K* (cm^{-1})		*A*		*K* (cm^{-1})	
3497. 78	15	28581. 41	$4d\ 5s\ ^1D_2$—$4d\ 5p\ ^1D^\circ_2$	2220. 25	18	45025. 91	$4d\ 4d\ ^1G_4$—$4d\ 5p\ ^3F^\circ_3$
3278. 86	40	30489. 65	$4d\ 5s\ ^1D_2$—$4d\ 5p\ ^3F^\circ_2$	2218. 48	15	45061. 83	$4d\ 5p\ ^3P^\circ_0$—$4d\ 6s\ ^3D_1$
3223. 95	20	31008. 92	$4d\ 5s\ ^1D_2$—$4d\ 5p\ ^3F^\circ_3$	2206. 97	40	45296. 82	$5s\ 5p\ ^3P^\circ_2$—$5p\ 5p\ ^3P_1$
3160. 00	7	31636. 44	$4d\ 4d\ ^1S_0$—$4d\ 5p\ ^3D^\circ_1$	2206. 33	60	45309. 96	$4d\ 5p\ ^3P^\circ_1$—$4d\ 6s\ ^3D_1$
3096. 95	5	32280. 50	$4d\ 5s\ ^1D_2$—$4d\ 5p\ ^3D^\circ_3$	2192. 05	35	45605. 09	
2978. 72	5	35720. 11	$4d\ 4d\ ^1S_0$—$4d\ 5p\ ^3P^\circ_1$	2191. 15	100	45623. 83	$4d\ 5p\ ^3P^\circ_1$—$4d\ 6s\ ^3D_2$
2886. 70	15	34631. 50	$4d\ 5s\ ^1D_2$—$4d\ 5p\ ^3P^\circ_1$	2186. 20	1	45727. 12	$4d\ 5p\ ^1F^\circ_3$—$4d\ 5d\ ^3F_4$
2869. 06	20	34844. 42	$4d\ 5s\ ^3D_2$—$4d\ 5p\ ^1D^\circ_2$	2180. 12	22	45854. 61	
2836. 18	40	35248. 35	$4d\ 5s\ ^3D_1$—$4d\ 5p\ ^1D^\circ_2$	2178. 49	20	45888. 93	$5s\ 5p\ ^3P^\circ_1$—$5p\ 5p\ ^3P_0$
2832. 81	20	35290. 28	$4d\ 5s\ ^1D_2$—$4d\ 5p\ ^3P^\circ_2$	2175. 80	100	45945. 66	$4d\ 5p\ ^3P^\circ_2$—$4d\ 6s\ ^3D_3$
2775. 23	25	36022. 43	$4d\ 5s\ ^3D_3$—$4d\ 5p\ ^3F^\circ_3$	2166. 38	22	46145. 42	$4d\ 5p\ ^3P^\circ_2$—$4d\ 5d\ ^1D_2$
2735. 76	75	36542. 12	$4d\ 5s\ ^3D_3$—$4d\ 5p\ ^3F^\circ_3$	2162. 20	40	46234. 62	
2720. 07	40	36752. 89	$4d\ 5s\ ^3D_2$—$4d\ 5p\ ^3F^\circ_2$	2159. 24	40	46297. 99	$4d\ 4d\ ^1G_4$—$4d\ 5p\ ^3D^\circ_3$
2715. 76	45	36811. 22	$4d\ 5s\ ^3D_2$—$4d\ 5p\ ^3D^\circ_1$	2151. 98	15	46454. 17	$5s\ 5p\ ^3P^\circ_1$—$5p\ 5p\ ^1D_2$
2709. 05	50	36902. 39	$4d\ 5s\ ^3D_3$—$4d\ 5p\ ^3D^\circ_2$	2149. 45	10	46508. 94	$4d\ 5p\ ^1F^\circ_3$—$4d\ 5d\ ^1F_3$
2698. 31	60	37049. 26	$4d\ 5s\ ^1D_2$—$4d\ 5p\ ^1P^\circ_1$	2143. 72	12	46633. 13	$4d\ 4d\ ^1G_4$—$4d\ 5p\ ^3F^\circ_4$
2690. 49	70	37156. 94	$4d\ 5s\ ^3D_1$—$4d\ 5p\ ^3F^\circ_2$	2139. 85	25	46717. 47	$4d\ 4d\ ^3P_2$—$4d\ 5p\ ^3F^\circ_2$
2686. 28	75	37215. 17	$4d\ 5s\ ^3D_1$—$4d\ 5p\ ^3D^\circ_1$	2138. 45	35	46748. 05	$5s\ 5p\ ^3P^\circ_1$—$5p\ 5p\ ^3P_1$
2682. 16	100	37272. 47	$4d\ 5s\ ^3D_2$—$4d\ 5p\ ^3F^\circ_3$	2137. 90	35	46760. 07	$4d\ 5p\ ^3D^\circ_3$—$4d\ 5d\ ^3D_2$
2664. 26	150	37522. 73	$4d\ 5s\ ^1D_2$—$4d\ 5p\ ^1F^\circ_3$	2135. 92	10	46803. 41	$4d\ 5p\ ^3P^\circ_1$—$4d\ 5d\ ^1D_2$
2656. 46	100	37632. 90	$4d\ 5s\ ^3D_2$—$4d\ 5p\ ^3D^\circ_2$				
2643. 79	200	37813. 24	$4d\ 5s\ ^3D_3$—$4d\ 5p\ ^3D^\circ_3$	2131. 61	4	46898. 03	$4d\ 5p\ ^3P^\circ_2$—$4d\ 5d\ ^3F_2$
2628. 26	60	38036. 65	$4d\ 5s\ ^3D_1$—$4d\ 5p\ ^3D^\circ_2$	2125. 29	15	47037. 48	$4d\ 5p\ ^1P^\circ_1$—$4d\ 5d\ ^1P_1$
2621. 28	50	38137. 93	$4d\ 4d\ ^1S_0$—$4d\ 5p\ ^1P^\circ_1$	2125. 06	40	47042. 57	$5s\ 5p\ ^3P^\circ_2$—$5p\ 5p\ ^3P_2$
2620. 56	250	38148. 41	$4d\ 5s\ ^3D_3$—$4d\ 5p\ ^3F^\circ_4$	2120. 05	4	47153. 72	$4d\ 5p\ ^1P^\circ_1$—$4d\ 5d\ ^3P_2$
2593. 64	100	38544. 33	$4d\ 5s\ ^3D_2$—$4d\ 5p\ ^3D^\circ_3$	2116. 63	18	47229. 90	$4d\ 4d\ ^3P_1$—$4d\ 5p\ ^3F^\circ_2$
2448. 86	100	40822. 96	$4d\ 5s\ ^3D_3$—$4d\ 5p\ ^3P^\circ_2$	2116. 30	18	47237. 27	$4d\ 4d\ ^3P_2$—$4d\ 5p\ ^3F^\circ_3$
2444. 58	50	40894. 42	$4d\ 5s\ ^3D_2$—$4d\ 5p\ ^3P^\circ_1$	2114. 10	35	47286. 42	$4d\ 5p\ ^3D^\circ_3$—$4d\ 5d\ ^3G_3$
2438. 70	25	40993. 02		2113. 98	40	47289. 10	$4d\ 4d\ ^3P_1$—$4d\ 5p\ ^3D^\circ_1$
2420. 65	75	41298. 67	$4d\ 5s\ ^3D_1$—$4d\ 5p\ ^3P^\circ_1$	2112. 40	5	47324. 47	$4d\ 5p\ ^3D^\circ_2$—$4d\ 5d\ ^3D_1$
				2108. 37	7	47414. 90	$5s\ 5p\ ^3P^\circ_0$—$5p\ 5p\ ^3P_1$
2406. 21	40	41546. 48	$4d\ 5s\ ^3D_1$—$4d\ 5p\ ^3P^\circ_0$				
2405. 81	35	41553. 39	$4d\ 5s\ ^3D_2$—$4d\ 5p\ ^3P^\circ_2$	2106. 18	3, Hf?	47464. 21	$4d\ 5p\ ^3P^\circ_2$—$4d\ 5d\ ^3F_3$
2389. 32	10	41840. 15		2105. 33	1	47483. 37	$4d\ 5p\ ^1F^\circ_3$—$4d\ 5d\ ^3S_1$
2382. 65	10	41957. 26	$4d\ 5s\ ^3D_1$—$4d\ 5p\ ^3P^\circ_2$	2104. 23	25	47508. 19	$4d\ 5p\ ^3F^\circ_4$—$4d\ 5d\ ^3G_4$
2336. 50	10	42785. 92	$5s\ 5p\ ^1P^\circ_1$—$5p\ 5p\ ^1D_2$	2103. 16	50	47532. 36	$4d\ 5p\ ^3D^\circ_3$—$4d\ 5d\ ^3D_3$
				2102. 30	40	47551. 80	$4d\ 4d\ ^3P_0$—$4d\ 5p\ ^3D^\circ_1$
2321. 89	7	43055. 11	$4d\ 5s\ ^3D_3$—$4d\ 5p\ ^1F^\circ_3$				
2308. 12	75	43311. 95	$4d\ 5s\ ^3D_2$—$4d\ 5p\ ^1P^\circ_1$	2100. 29	10	47597. 30	$4d\ 4d\ ^3P_2$—$4d\ 5p\ ^3D^\circ_2$
2301. 60	100	43434. 64		2097. 03	40	47671. 28	$4d\ 5p\ ^3D^\circ_2$—$4d\ 5d\ ^3D_2$
2286. 78	20	43716. 05	$4d\ 5s\ ^3D_1$—$4d\ 5p\ ^1P^\circ_1$	2089. 50	40	47843. 06	$4d\ 5p\ ^3D^\circ_3$—$4d\ 5d\ ^3G_4$
2283. 15	20	43785. 59	$4d\ 5s\ ^3D_2$—$4d\ 5p\ ^1F^\circ_3$	2086. 78	200	47905. 41	$4d\ 4d\ ^1D_2$—$4d\ 5p\ ^1D^\circ_2$
				2085. 35	25	47938. 25	$4d\ 5p\ ^3P^\circ_1$—$4d\ 5d\ ^3P_0$
2281. 60	20	43815. 34	$4d\ 5p\ ^3P^\circ_0$—$4d\ 5d\ ^3D_1$	2083. 77	7, Hf?	47974. 60	$4d\ 5p\ ^3D^\circ_3$—$4d\ 6s\ ^3D_2$
2281. 43	30	43818. 60		2082. 61	20	48001. 32	$4d\ 5p\ ^3P^\circ_2$—$4d\ 5d\ ^3P_1$
2280. 07	8	43844. 74		2081. 81	30	48019. 76	$4d\ 5p\ ^1P^\circ_1$—$4d\ 6s\ ^1D_2$
2276. 66	15	43910. 40	$4d\ 5p\ ^1F^\circ_3$—$4d\ 5d\ ^1D_2$	2080. 99	100	48038. 68	$4d\ 5p\ ^1F^\circ_3$—$4d\ 5d\ ^1G_4$
2257. 83	40	44276. 57	$4d\ 5p\ ^3P^\circ_2$—$4d\ 5d\ ^3G_3$	2077. 92	100	48109. 64	$4d\ 4d\ ^3P_1$—$4d\ 5p\ ^3D^\circ_2$
2254. 26	15	44346. 68					
2252. 37	20	44383. 89	$4d\ 5p\ ^1P^\circ_1$—$4d\ 5d\ ^1D_2$	2076. 37	10	48145. 55	$4d\ 5p\ ^3D^\circ_1$—$4d\ 5d\ ^3D_1$
2251. 14	25	44408. 14	$4d\ 5p\ ^3P^\circ_1$—$4d\ 5d\ ^3D_2$	2074. 12	50	48197. 77	$4d\ 5p\ ^3D^\circ_2$—$4d\ 5d\ ^3G_3$
2245. 36	50	44522. 44	$4d\ 5p\ ^3P^\circ_2$—$4d\ 5d\ ^3D_3$	2073. 81	?	48207. 00	$4d\ 5p\ ^3F^\circ_2$—$4d\ 5d\ ^3D_1$
2241. 33	2	44602. 48	$5s\ 5s\ ^1S_0$—$5s\ 5p\ ^3P^\circ_1$	2070. 96	45, Hf?	48271. 31	$5s\ 5s\ ^1S_0$—$5s\ 5p\ ^1P^\circ_1$
				2070. 43	125	48283. 66	$4d\ 5p\ ^3F^\circ_4$—$4d\ 5d\ ^3G_5$
2238. 26	5	44663. 65					
2231. 00	30	44808. 98	$4d\ 4d\ ^3P_2$—$4d\ 5p\ ^1D^\circ_2$	2064. 93	10	48412. 25	$4d\ 5p\ ^3P^\circ_0$—$4d\ 5d\ ^3P_1$
2228. 10	20	44867. 30		2061. 47	50	48493. 49	$5s\ 5p\ ^3P^\circ_1$—$5p\ 5p\ ^3P_2$ / $4d\ 5p\ ^3D^\circ_1$—$4d\ 5d\ ^3D_2$
2223. 31	10	44963. 95	$4d\ 5p\ ^3P^\circ_2$—$4d\ 6s\ ^3D_2$				
2221. 36	20	45003. 42	$5s\ 5p\ ^3P^\circ_2$—$5p\ 5p\ ^1D_2$	2060. 83	75	48508. 55	$4d\ 4d\ ^3P_2$—$4d\ 5p\ ^3D^\circ_3$

TABLE 6. *Classified lines of* Zr III—Continued

Wavelength	Intensity	Wave number	Term combination
A		*K* (cm^{-1})	
2059.01	12	48551.42	$4d\ 5p\ {}^3F_2^\circ - 4d\ 5d\ {}^3D_2$
2058.73	40	48558.03	$4d\ 5p\ {}^3F_3^\circ - 4d\ 5d\ {}^3G_3$
2058.14	20	48571.94	$4d\ 5p\ {}^3D_2^\circ - 4d\ 6s\ {}^3D_1$
2056.13	75	48619.42	$4d\ 5p\ {}^3F_4^\circ - 4d\ 6s\ {}^3D_3$
2048.40	3	48802.87	$4d\ 5p\ {}^3F_3^\circ - 4d\ 5d\ {}^3D_3$
2043.79	20	48912.94	$4d\ 5p\ {}^3P_2^\circ - 4d\ 5d\ {}^3P_2$
2042.04	20	48954.85	$4d\ 5p\ {}^3D_3^\circ - 4d\ 6s\ {}^3D_3$
2036.92	50	49077.88	$4d\ 5p\ {}^3F_2^\circ - 4d\ 5d\ {}^3G_3$
2035.42	100	49114.04	$4d\ 5p\ {}^3F_3^\circ - 4d\ 5d\ {}^3G_4$
2033.76	12	49154.12	$5s\ 4f\ {}^1F_3^\circ - 5s\ 5g\ {}^3G_4$ $4d\ 5p\ {}^3D_3^\circ - 4d\ 5d\ {}^1D_2$
2030.12	8	49242.25	$4d\ 5p\ {}^3P_2^\circ - 4d\ 5d\ {}^3S_1$
2029.94	10	49246.61	$4d\ 5p\ {}^3F_3^\circ - 4d\ 6s\ {}^3D_2$
2026.78	60	49323.38	$4d\ 5p\ {}^3F_2^\circ - 4d\ 5d\ {}^3D_3$
2023.88	7	49394.05	$4d\ 5p\ {}^3D_1^\circ - 4d\ 6s\ {}^3D_1$
2021.52	30	49451.70	$4d\ 5p\ {}^3F_2^\circ - 4d\ 6s\ {}^3D_1$
2016.63	35	49571.60	$4d\ 5p\ {}^3P_1^\circ - 4d\ 5d\ {}^3P_2$
2013.30	30	49653.58	$4d\ 5p\ {}^3P_0^\circ - 4d\ 5d\ {}^3S_1$
2011.13	2	49707.14	$4d\ 5p\ {}^3D_1^\circ - 4d\ 6s\ {}^3D_2$
2008.26	12	49778.17	$4d\ 5p\ {}^3P_2^\circ - 4d\ 6s\ {}^1D_2$
2006.82	100	49813.88	$4d\ 4d\ {}^1D_2 - 4d\ 5p\ {}^3F_2^\circ$
2004.69	8	49866.80	$4d\ 5p\ {}^3D_2^\circ - 4d\ 6s\ {}^3D_3$
2004.45	7	49872.77	$4d\ 4d\ {}^1D_2 - 4d\ 5p\ {}^3D_1^\circ$
2003.26	8	49902.40	$4d\ 5p\ {}^3P_1^\circ - 4d\ 5d\ {}^3S_1$
2002.00	55, Hf?	49933.80	
2001.96	20	49935.80	
2000.23	45	49994.25	
1999.09	3	50022.8	$5s\ 4f\ {}^3F_4^\circ - 5s\ 5g\ {}^3G_4$
1998.51	6	50037.3	$5s\ 4f\ {}^3F_4^\circ - 5s\ 5g\ {}^3G_5$
1997.30	3	50067.6	$5s\ 4f\ {}^3F_3^\circ - 5s\ 5g\ {}^3G_3$
1996.92	15	50077.1	$5s\ 4f\ {}^3F_3^\circ - 5s\ 5g\ {}^3G_4$
1995.36	15	50116.3	$5s\ 4f\ {}^3F_2^\circ - 5s\ 5g\ {}^3G_3$
1994.46	30	50138.9	$4d\ 5p\ {}^3F_4^\circ - 4d\ 5d\ {}^3F_3$
1990.95	30	50227.3	$4d\ 5p\ {}^3F_3^\circ - 4d\ 6s\ {}^3D_3$
1989.83	50	50255.5	$5s\ 4f\ {}^1F_3^\circ - 5s\ 5g\ {}^1G_4$
1986.75	20	50333.5	$4d\ 4d\ {}^1D_2 - 4d\ 5p\ {}^3F_3^\circ$
1983.14	40	50425.1	$4d\ 5p\ {}^3F_3^\circ - 4d\ 5d\ {}^1D_2$
1982.61	12	50438.6	$4d\ 5p\ {}^3P_1^\circ - 4d\ 6s\ {}^1D_2$
1981.67	20	50462.5	$4d\ 5p\ {}^1D_2^\circ - 4d\ 5d\ {}^3D_2$
1981.21	20	50474.2	$4d\ 5p\ {}^3D_3^\circ - 4d\ 5d\ {}^3F_3$
1974.99	60	50633.2	$4d\ 5p\ {}^3F_4^\circ - 4d\ 5d\ {}^3F_4$
1972.63	22	50693.7	$4d\ 4d\ {}^1D_2 - 4d\ 5p\ {}^3D_2^\circ$
1967.81	25	50817.9	$4d\ 5p\ {}^3D_2^\circ - 4d\ 5d\ {}^3F_2$
1966.22	85	50859.0	$4d\ 4d\ {}^3P_2 - 4d\ 5p\ {}^3P_1^\circ$
1965.18	20	50885.9	$4d\ 5p\ {}^3D_1^\circ - 4d\ 5d\ {}^1D_2$
1962.92	40	50944.5	$4d\ 5p\ {}^3F_2^\circ - 4d\ 5d\ {}^1D_2$
1962.01	100	50968.1	$4d\ 5p\ {}^3D_3^\circ - 4d\ 5d\ {}^3F_4$
1961.32	50	50986.1	$4d\ 5p\ {}^1D_2^\circ - 4d\ 5d\ {}^3G_3$
1956.03	10	51124.0	$5s\ 4f\ {}^3F_4^\circ - 5s\ 5g\ {}^1G_4$
1953.95	100	51178.4	$4d\ 5p\ {}^3F_3^\circ - 4d\ 5d\ {}^3F_2$
1951.86	8	51233.2	$4d\ 5p\ {}^1D_2^\circ - 4d\ 5d\ {}^3D_3$
1946.99	50	51361.3	$4d\ 5p\ {}^1D_2^\circ - 4d\ 6s\ {}^3D_1$
1946.61	80	51371.4	$4d\ 4d\ {}^3P_1 - 4d\ 5p\ {}^3P_1^\circ$
1946.12	25	51384.3	$4d\ 5p\ {}^3D_2^\circ - 4d\ 5d\ {}^3F_3$
1945.00	20	51413.9	$4d\ 5p\ {}^3F_4^\circ - 4d\ 5d\ {}^1F_3$
1941.08	100	51517.7	$4d\ 4d\ {}^3P_2 - 4d\ 5p\ {}^3P_2^\circ$
A		*K* (cm^{-1})	
1940.25	200	51539.8	$4d\ 4d\ {}^1G_4 - 4d\ 5p\ {}^1F_3^\circ$
1937.81	12	51604.6	$4d\ 4d\ {}^1D_2 - 4d\ 5p\ {}^3D_3^\circ$
1937.27	80	51619.0	$4d\ 4d\ {}^3P_1 - 4d\ 5p\ {}^3P_0^\circ$
1936.67	75	51635.0	$4d\ 4d\ {}^3P_0 - 4d\ 5p\ {}^3P_1^\circ$
1936.48	75	51640.1	$4d\ 5p\ {}^3D_1^\circ - 4d\ 5d\ {}^3F_2$
1935.20	40	51674.2	$4d\ 5p\ {}^1D_2^\circ - 4d\ 6s\ {}^3D_2$
1934.32	50	51697.8	$4d\ 5p\ {}^3F_2^\circ - 4d\ 5d\ {}^3F_2$
1932.54	75	51745.4	$4d\ 5p\ {}^3F_3^\circ - 4d\ 5d\ {}^3F_3$
1925.98	15	51921.6	$4d\ 5p\ {}^3D_2^\circ - 4d\ 5d\ {}^3P_1$
1925.88	12	51924.3	$4d\ 5p\ {}^3D_3^\circ - 4d\ 5d\ {}^3P_2$
1922.26	6	52022.1	$4d\ 5p\ {}^3D_1^\circ - 4d\ 5d\ {}^3P_0$
1921.96	75	52030.2	$4d\ 4d\ {}^3P_1 - 4d\ 5p\ {}^3P_2^\circ$
1914.25	65	52239.8	$4d\ 5p\ {}^3F_3^\circ - 4d\ 5d\ {}^3F_4$
1913.34	18	52264.6	$4d\ 5p\ {}^3F_2^\circ - 4d\ 5d\ {}^3F_3$
1894.36	20	52788.3	$4d\ 5p\ {}^3D_3^\circ - 4d\ 6s\ {}^1D_2$
1892.07	50	52852.2	$4d\ 5p\ {}^1D_2^\circ - 4d\ 5d\ {}^1D_2$
1888.70	2	52946.5	$4d\ 5p\ {}^3F_4^\circ - 4d\ 5d\ {}^1G_4$
1881.02	20	53162.6	$4d\ 5p\ {}^3D_2^\circ - 4d\ 5d\ {}^3S_1$
1879.92	10	53193.8	$4d\ 5p\ {}^3F_3^\circ - 4d\ 5d\ {}^3P_2$
1878.56	10	53232.3	$5s\ 5p\ {}^1P_1^\circ - 5s\ 5d\ {}^3D_2$
1877.00	35	53276.5	$4d\ 4d\ {}^3P_2 - 4d\ 5p\ {}^1P_1^\circ$
1867.76	15	53540.1	$4d\ 5p\ {}^3F_2^\circ - 4d\ 5d\ {}^1F_3$
1865.83	18	53595.4	$4d\ 5p\ {}^3F_2^\circ - 4d\ 5d\ {}^1P_1$
1865.45	30	53606.4	$4d\ 5p\ {}^1D_2^\circ - 4d\ 5d\ {}^3F_2$
1864.06	75	53646.3	$4d\ 4d\ {}^3F_2 - 4d\ 5p\ {}^1D_2^\circ$
1861.77	25	53712.3	$4d\ 5p\ {}^3F_2^\circ - 4d\ 5d\ {}^3P_2$
1860.47	25	53749.9	$4d\ 4d\ {}^3P_2 - 4d\ 5p\ {}^1F_3^\circ$
1859.12	30	53788.9	$4d\ 4d\ {}^3P_1 - 4d\ 5p\ {}^1P_1^\circ$
1853.38	40	53955.5	$4d\ 4d\ {}^1D_2 - 4d\ 5p\ {}^3P_1^\circ$
1850.35	12	54043.8	$4d\ 5p\ {}^3F_2^\circ - 4d\ 5d\ {}^3S_1$
1850.06	40	54052.3	$4d\ 4d\ {}^3P_0 - 4d\ 5p\ {}^1P_1^\circ$
1849.84	1	54058.7	$4d\ 5p\ {}^3F_3^\circ - 4d\ 6s\ {}^1D_2$
1833.09	15	54552.7	$4d\ 5p\ {}^3F_3^\circ - 4d\ 5d\ {}^1G_4$
1832.16	22	54580.4	$4d\ 5p\ {}^3F_2^\circ - 4d\ 6s\ {}^1D_2$
1831.89	35	54588.4	$4d\ 4d\ {}^3F_4 - 4d\ 5p\ {}^3F_3^\circ$
1822.35	10	54874.2	$4d\ 4d\ {}^3F_3 - 4d\ 5p\ {}^3F_3^\circ$
1805.26	100	55393.7	$4d\ 4d\ {}^3F_3 - 4d\ 5p\ {}^3F_3^\circ$
1803.57	18	55445.6	$5s\ 5p\ {}^3P_2^\circ - 5s\ 5d\ {}^3D_3$
1803.46	12	55449.0	$5s\ 5p\ {}^3P_2^\circ - 5s\ 5d\ {}^3D_2^\circ$ $4d\ 5p\ {}^1D_2^\circ - 4d\ 5d\ {}^1F_3$
1801.67	25	55504.1	$4d\ 5p\ {}^1D_2^\circ - 4d\ 5d\ {}^1P_1$
1800.03	75	55554.6	$4d\ 4d\ {}^3F_2 - 4d\ 5p\ {}^3F_2^\circ$
1798.36	18	55606.2	$5s\ 5p\ {}^1P_1^\circ - 5s\ 6s\ {}^3S_1$
1798.13	125	55613.3	$4d\ 4d\ {}^3F_2 - 4d\ 5p\ {}^3D_1^\circ$
1796.36	15	55668.1	$5s\ 5p\ {}^1P_1^\circ - 5s\ 5d\ {}^1D_2$
1793.59	150	55754.1	$4d\ 4d\ {}^3F_3 - 4d\ 5p\ {}^3D_2^\circ$
1790.19	200	55860.0	$4d\ 4d\ {}^3F_4 - 4d\ 5p\ {}^3D_3^\circ$
1783.35	40	56074.2	$4d\ 4d\ {}^3F_2 - 4d\ 5p\ {}^3F_3^\circ$
1779.51	100	56195.2	$4d\ 4d\ {}^3F_4 - 4d\ 5p\ {}^3F_4^\circ$
1773.90	40	56373.0	$4d\ 4d\ {}^1D_2 - 4d\ 5p\ {}^1P_1^\circ$
1771.96	30	56434.7	$4d\ 4d\ {}^3F_2 - 4d\ 5p\ {}^3D_2^\circ$
1770.35	4	56486.0	$4d\ 5s\ {}^1D_2 - 5s\ 5p\ {}^3P_2^\circ$
1770.28	20	56488.2	$4d\ 5p\ {}^1D_2^\circ - 4d\ 6s\ {}^1D_2$
1764.75	30	56665.2	$4d\ 4d\ {}^3F_3 - 4d\ 5p\ {}^3D_3^\circ$
1763.99	20	56689.7	$5s\ 5p\ {}^3P_1^\circ - 5s\ 5d\ {}^3D_1$

TABLE 6. *Classified lines of* Zr III—Continued

Wavelength	Intensity	Wave number	Term combination	Wavelength	Intensity	Wave number	Term combination
A		$K(cm^{-1})$		A		$K(cm^{-1})$	
1759. 12	35	56846. 6	$4d\ 4d\ {}^1D_2 - 4d\ 5p\ {}^1F^\circ_3$	919. 59	25	108744	$4d\ 4d\ {}^1G_4 - 4d\ 4f\ {}^1H^\circ_5$
1757. 48	20	56899. 7	$5s\ 5p\ {}^3P^\circ_1 - 5s\ 5d\ {}^3D_2$	918. 06	20	108925	$4d\ 4d\ {}^1G_4 - 4d\ 4f\ {}^1G^\circ_4$
1754. 38	40	57000. 2	$4d\ 4d\ {}^3F_2 - 4d\ 5p\ {}^3F^\circ_3$	912. 28	3	109616	$4d\ 4d\ {}^1G_4 - 4d\ 4f\ {}^3H^\circ_4$
1743. 55	20	57354. 2	$5s\ 5p\ {}^3P^\circ_0 - 5s\ 5d\ {}^3D_1$	911. 22	1	109743	$4d\ 4d\ {}^1G_4 - 4d\ 4f\ {}^3F^\circ_3$
1729. 38	6	57824. 2	$5s\ 5p\ {}^3P^\circ_2 - 5s\ 6s\ {}^3S_1$	909. 32	8	109972	$4d\ 4d\ {}^1G_4 - 4d\ 4f\ {}^3H^\circ_5$
1727. 46	3	57888. 5	$5s\ 5p\ {}^3P^\circ_2 - 5s\ 5d\ {}^1D_2$	907. 18	15	110232	$4d\ 4d\ {}^1G_4 - 4d\ 4f\ {}^3F^\circ_4$
1725. 03	40	57970. 0	$5s\ 5p\ {}^1P^\circ_1 - 5s\ 6s\ {}^1S_0$	901. 15	2	110969	$4d\ 4d\ {}^1G_4 - 4d\ 4f\ {}^3G^\circ_5$
1703. 36	40	58707. 5	$4d\ 5s\ {}^1D_2 - 5s\ 5p\ {}^1P^\circ_1$	896. 45	1	111551	$4d\ 4d\ {}^1G_4 - 4d\ 4f\ {}^3G^\circ_4$
1687. 14	3	59271. 9	$5s\ 5p\ {}^3P^\circ_1 - 5s\ 6s\ {}^3S_1$	894. 08	2	111847	$4d\ 4d\ {}^1G_4 - 4d\ 4f\ {}^3G^\circ_3$
1675. 75	35	59674. 8	$4d\ 4d\ {}^3F_3 - 4d\ 5p\ {}^3P^\circ_2$	893. 22	4	111954	$4d\ 4d\ {}^3P_2 - 4d\ 4f\ {}^3F^\circ_3$
1675. 06	35	59699. 4	$4d\ 4d\ {}^3F_2 - 4d\ 5p\ {}^3P^\circ_1$	891. 00	1	112233	$4d\ 4d\ {}^3P_1 - 4d\ 4f\ {}^3F^\circ_2$
1672. 35	15	59796. 1	$4d\ 4d\ {}^1S_0 - 5s\ 5p\ {}^1P^\circ_1$	890. 78	6	112261	$4d\ 4d\ {}^1G_4 - 4d\ 4f\ {}^1F^\circ_3$
1668. 35	8	59939. 5	$5s\ 5p\ {}^3P^\circ_0 - 5s\ 6s\ {}^3S_1$	885. 66	15	112910	$4d\ 4d\ {}^1G_4 - 4d\ 4f\ {}^3D^\circ_3$
1638. 33	50	61037. 8	$4d\ 5s\ {}^3D_1 - 5s\ 5p\ {}^3P^\circ_0$	883. 52	2	113184	$4d\ 4d\ {}^3P_2 - 4d\ 4f\ {}^3G^\circ_3$
1636. 61	20	61101. 9	$4d\ 4d\ {}^3F_4 - 4d\ 5p\ {}^1F^\circ_3$	879. 04	5	113760	$4d\ 4d\ {}^3P_1 - 4d\ 4f\ {}^1D^\circ_2$
1631. 31	75	61300. 4	$4d\ 5s\ {}^3D_2 - 5s\ 5p\ {}^3P^\circ_1$	873. 61	18	114468	$4d\ 4d\ {}^3P_2 - 4d\ 4f\ {}^1F^\circ_3$
1628. 04	15	61423. 6	$4d\ 5p\ {}^1P^\circ_1 - 5p\ 5p\ {}^1S_0$	873. 36	6	114500	$4d\ 4d\ {}^3P_2 - 4d\ 4f\ {}^3D^\circ_1$
1622. 23	1	61643. 5	$5s\ 5p\ {}^3P^\circ_1 - 5s\ 6s\ {}^1S_0$	872. 76	12	114579	$4d\ 4d\ {}^3P_2 - 4d\ 4f\ {}^3D^\circ_2$
1620. 62	50	61704. 8	$4d\ 5s\ {}^3D_1 - 5s\ 5p\ {}^3P^\circ_1$	870. 93	5	114820	$4d\ 4d\ {}^1D_2 - 4d\ 4f\ {}^3F^\circ_2$
1615. 33	15	61906. 8	$4d\ 4d\ {}^3F_3 - 4d\ 5p\ {}^1F^\circ_3$	869. 47	12	115013	$4d\ 4d\ {}^3P_1 - 4d\ 4f\ {}^3D^\circ_1$
1612. 38	100	62020. 1	$4d\ 5s\ {}^3D_3 - 5s\ 5p\ {}^3P^\circ_2$	869. 18	2	115043	$4d\ 4d\ {}^1D_2 - 4d\ 4f\ {}^3F^\circ_3$
1609. 94	20	62114. 1	$4d\ 4d\ {}^3F_2 - 4d\ 5p\ {}^1P^\circ_1$	868. 99	25	115076	$4d\ 4d\ {}^3P_1 - 4d\ 4f\ {}^3D^\circ_2$
1593. 59	40	62751. 4	$4d\ 5s\ {}^3D_2 - 5s\ 5p\ {}^3P^\circ_2$	868. 64	25	115122	$4d\ 4d\ {}^3P_2 - 4d\ 4f\ {}^3D^\circ_3$
1583. 39	20	63155. 6	$4d\ 5s\ {}^3D_1 - 5s\ 5p\ {}^3P^\circ_2$	867. 50	20	115274	$4d\ 4d\ {}^3P_0 - 4d\ 4f\ {}^3D^\circ_1$
1566. 35	1	63842. 7	$4d\ 5p\ {}^3P^\circ_1 - 5p\ 5p\ {}^1S_0$	865. 19	4	115582	$4d\ 4d\ {}^3P_1 - 4d\ 4f\ {}^1P^\circ_1$
1565. 45	10	63879. 4	$4d\ 5p\ {}^1P^\circ_1 - 5p\ 5p\ {}^3P_0$	864. 86	30	115626	$4d\ 4d\ {}^3P_2 - 4d\ 4f\ {}^3P^\circ_2$
1563. 24	25	63969. 7	$4d\ 5p\ {}^1F^\circ_3 - 5p\ 5p\ {}^1D_2$	863. 23	15	115844	$4d\ 4d\ {}^3P_2 - 4d\ 4f\ {}^3P^\circ_1$
1539. 07	3	64974. 3	$4d\ 5s\ {}^3D_2 - 5s\ 5p\ {}^1P^\circ_1$				$4d\ 4d\ {}^3P_0 - 4d\ 4f\ {}^1P^\circ_1$
1514. 93	8	66009. 6	$4d\ 5p\ {}^1F^\circ_3 - 5p\ 5p\ {}^3P_2$	860. 04	7	116274	$4d\ 4d\ {}^1D_2 - 4d\ 4f\ {}^3G^\circ_3$
1510. 52	10	66202. 4	$4d\ 5p\ {}^3P^\circ_2 - 5p\ 5p\ {}^1D_2$	859. 56	25	116339	$4d\ 4d\ {}^1D_2 - 4d\ 4f\ {}^1D^\circ_2$
1508. 38	5	66296. 3	$4d\ 5p\ {}^3P^\circ_1 - 5p\ 5p\ {}^3P_0$	859. 42	12	116358	$4d\ 4d\ {}^3P_1 - 4d\ 4f\ {}^3P^\circ_1$
1503. 87	6	66495. 1	$4d\ 5p\ {}^3P^\circ_2 - 5p\ 5p\ {}^3P_1$	858. 56	4	116474	$4d\ 4d\ {}^3P_1 - 4d\ 4f\ {}^3P^\circ_0$
1495. 66	2	66860. 1	$4d\ 5p\ {}^3P^\circ_1 - 5p\ 5p\ {}^1D_2$	857. 49	4	116619	$4d\ 4d\ {}^3P_0 - 4d\ 4f\ {}^3P^\circ_1$
1494. 67	10	66904. 4	$4d\ 5p\ {}^3P^\circ_0 - 5p\ 5p\ {}^3P_1$	850. 61	30	117563	$4d\ 4d\ {}^1D_2 - 4d\ 4f\ {}^1F^\circ_3$
1489. 13	12	67153. 3	$4d\ 5p\ {}^3P^\circ_1 - 5p\ 5p\ {}^3P_1$	849. 92	3	117658	$4d\ 4d\ {}^1D_2 - 4d\ 4f\ {}^3D^\circ_3$
1465. 44	25	68238. 9	$4d\ 5p\ {}^3P^\circ_2 - 5p\ 5p\ {}^3P_2$	845. 89	18	118219	$4d\ 4d\ {}^1D_2 - 4d\ 4f\ {}^3D^\circ_2$
1451. 40	8	68899. 0	$4d\ 5p\ {}^3P^\circ_1 - 5p\ 5p\ {}^3P_2$	845. 26	8	118307	$4d\ 4d\ {}^3F_4 - 4d\ 4f\ {}^1H^\circ_5$
1444. 88	20	69209. 9	$4d\ 5p\ {}^3D^\circ_3 - 5p\ 5p\ {}^1D_2$	844. 00	3	118483	$4d\ 4d\ {}^3F_4 - 4d\ 4f\ {}^1G^\circ_4$
1426. 11	5	70120. 8	$4d\ 5p\ {}^3D^\circ_2 - 5p\ 5p\ {}^1D_2$	842. 33	2	118718	$4d\ 4d\ {}^1D_2 - 4d\ 4f\ {}^3P^\circ_2$
1420. 87	25	70379. 4	$4d\ 5p\ {}^3D^\circ_1 - 5p\ 5p\ {}^3P_0$	840. 77	1	118939	$4d\ 4d\ {}^1D_2 - 4d\ 4f\ {}^3P^\circ_1$
1420. 12	35	70416. 6	$4d\ 5p\ {}^3D^\circ_2 - 5p\ 5p\ {}^3P_1$	839. 55	12	119111	$4d\ 4d\ {}^3F_3 - 4d\ 4f\ {}^1H^\circ_5$
1418. 81	6	70481. 6	$4d\ 5p\ {}^3F^\circ_3 - 5p\ 5p\ {}^1D_2$	839. 12	5	119172	$4d\ 4d\ {}^3F_4 - 4d\ 4f\ {}^3H^\circ_4$
1408. 40	15	71002. 6	$4d\ 5p\ {}^3F^\circ_2 - 5p\ 5p\ {}^1D_2$	838. 31	4	119288	$4d\ 4d\ {}^3F_3 - 4d\ 4f\ {}^1G^\circ_4$
1403. 74	20	71238. 3	$4d\ 5p\ {}^3D^\circ_1 - 5p\ 5p\ {}^3P_1$	838. 20	7	119303	$4d\ 4d\ {}^3F_4 - 4d\ 4f\ {}^3F^\circ_4$
1403. 48	40	71251. 5	$4d\ 5p\ {}^3D^\circ_3 - 5p\ 5p\ {}^3P_2$	836. 60	18	119531	$4d\ 4d\ {}^3F_4 - 4d\ 4f\ {}^3H^\circ_5$
1402. 62	4	71295. 1	$4d\ 5p\ {}^3F^\circ_2 - 5p\ 5p\ {}^3P_1$	834. 85	20	119782	$4d\ 4d\ {}^3F_4 - 4d\ 4f\ {}^3F^\circ_4$
1393. 20	6	71777. 2	$4d\ 4d\ {}^3P_1 - 5s\ 5p\ {}^3P^\circ_1$	834. 19	8	119877	$4d\ 4d\ {}^3F_3 - 4d\ 4f\ {}^3F^\circ_2$
1385. 75	18	72163. 1	$4d\ 5p\ {}^3D^\circ_2 - 5p\ 5p\ {}^3P_2$	833. 51	10	119975	$4d\ 4d\ {}^3F_3 - 4d\ 4f\ {}^3H^\circ_4$
1378. 93	30	72520. 0	$4d\ 5p\ {}^3F^\circ_3 - 5p\ 5p\ {}^3P_2$	832. 59	15	120107	$4d\ 4d\ {}^3F_3 - 4d\ 4f\ {}^3F^\circ_3$
1375. 13	25	72720. 4	$4d\ 4d\ {}^3P_2 - 5s\ 5p\ {}^3P^\circ_2$				
1371. 50	20	72912. 9	$4d\ 5p\ {}^1D^\circ_2 - 5p\ 5p\ {}^1D_2$	829. 50	25	120555	$4d\ 4d\ {}^3F_2 - 4d\ 4f\ {}^3F^\circ_2$
1369. 07	4	73042. 3	$4d\ 5p\ {}^3F^\circ_3 - 5p\ 5p\ {}^3P_2$	829. 24	15	120592	$4d\ 4d\ {}^3F_3 - 4d\ 4f\ {}^3F^\circ_4$
1320. 81	30	75711. 1	$4d\ 4d\ {}^3P_0 - 5s\ 5p\ {}^1P^\circ_1$	827. 90	20	120788	$4d\ 4d\ {}^3F_2 - 4d\ 4f\ {}^3F^\circ_3$
1281. 53	1	78031. 7	$4d\ 4d\ {}^1D_2 - 5s\ 5p\ {}^1P^\circ_1$	825. 65	18	121117	$4d\ 4d\ {}^3F_4 - 4d\ 4f\ {}^3G^\circ_5$
1000. 72	6	99928	$4d\ 4d\ {}^1S_0 - 4d\ 4f\ {}^1P^\circ_1$	824. 16	20	121336	$4d\ 4d\ {}^3F_3 - 4d\ 4f\ {}^3G^\circ_3$

TABLE 6. *Classified lines of* Zr III—Continued

Wavelength	Intensity	Wave number	Term combination	Wavelength	Intensity	Wave number	Term combination
A		$K(cm^{-1})$		*A*		$K(cm^{-1})$	
823.69	35	121405	$4d\ 4d\ {}^3F_4 - 4d\ 4f\ {}^3G^\circ_5$	719.16	1	139051	$4d\ 4d\ {}^3P_0 - 4d\ 6p\ {}^3P^\circ_1$
820.91	8	121816	$4d\ 4d\ {}^3F_4 - 4d\ 4f\ {}^1F^\circ_3$	717.53	3	139367	$4d\ 4d\ {}^3P_1 - 4d\ 6p\ {}^3P^\circ_2$
820.21	30	121920	$4d\ 4d\ {}^3F_3 - 4d\ 4f\ {}^3G^\circ_4$	716.28	7	139610	$4d\ 4d\ {}^1D_2 - 4d\ 6p\ {}^3F^\circ_3$
819.59	25	122012	$4d\ 4d\ {}^3F_2 - 4d\ 4f\ {}^3G^\circ_3$	715.53	7	139756	$4d\ 4d\ {}^3P_1 - 4d\ 6p\ {}^1P^\circ_1$
819.14	1	122079	$4d\ 4d\ {}^3F_2 - 4d\ 4f\ {}^1D^\circ_2$	714.18	6	140020	$4d\ 4d\ {}^3P_0 - 4d\ 6p\ {}^1P^\circ_1$
816.53	6	122470	$4d\ 4d\ {}^3F_4 - 4d\ 4f\ {}^3D^\circ_3$	710.98	10	140651	$4d\ 4d\ {}^1D_2 - 4d\ 6p\ {}^3D^\circ_2$
815.53	5	122620	$4d\ 4d\ {}^3F_3 - 4d\ 4f\ {}^1F^\circ_3$	708.40	8	141163	$4d\ 4d\ {}^1D_2 - 4d\ 6p\ {}^3D^\circ_3$
814.89	12	122716	$4d\ 4d\ {}^3F_3 - 4d\ 4f\ {}^3D^\circ_2$	700.80	2	142694	$4d\ 4d\ {}^3F_4 - 4d\ 6p\ {}^1F^\circ_3$
811.00	6	123305	$4d\ 4d\ {}^3F_2 - 4d\ 4f\ {}^1F^\circ_3$	696.91	4	143491	$4d\ 4d\ {}^3F_3 - 4d\ 6p\ {}^1F^\circ_3$
810.80	6	123335	$4d\ 4d\ {}^3F_2 - 4d\ 4f\ {}^3D^\circ_1$	695.29	12	143825	$4d\ 4d\ {}^3F_4 - 4d\ 6p\ {}^3F^\circ_4$
807.88	2	123781	$4d\ 4d\ {}^3F_3 - 4d\ 4f\ {}^3P^\circ_2$	695.06	10	143872	$4d\ 4d\ {}^3F_4 - 4d\ 6p\ {}^3F^\circ_3$
802.00	4	124688	$4d\ 4d\ {}^3F_2 - 4d\ 4f\ {}^3P^\circ_1$	694.69	8	143949	$4d\ 4d\ {}^3F_2 - 4d\ 6p\ {}^1D^\circ_2$
762.90	20	131079	$4d\ 5s\ {}^1D_2 - 5s\ 4f\ {}^1F^\circ_3$	693.65	2	144165	$4d\ 4d\ {}^3F_3 - 4d\ 6p\ {}^3F^\circ_2$
751.16	5	133127	$4d\ 4d\ {}^1G_4 - 4d\ 6p\ {}^1F^\circ_3$	691.42	15	144630	$4d\ 4d\ {}^3F_3 - 4d\ 6p\ {}^3F^\circ_4$
744.58	4	134304	$4d\ 4d\ {}^1G_4 - 4d\ 6p\ {}^3F^\circ_3$	691.19	10	144678	$4d\ 4d\ {}^3F_3 - 4d\ 6p\ {}^3F^\circ_3$
736.97	4	135691	$4d\ 5s\ {}^3D_3 - 5s\ 4f\ {}^3F^\circ_3$	690.39	50	144846	$4d\ 4d\ {}^3F_2 - 4d\ 6p\ {}^3F^\circ_2$
736.67	20	135746	$4d\ 5s\ {}^3D_3 - 5s\ 4f\ {}^3F^\circ_4$	687.95	12	145359	$4d\ 4d\ {}^3F_2 - 4d\ 6p\ {}^3F^\circ_3$
733.29	4	136372	$4d\ 5s\ {}^3D_2 - 5s\ 4f\ {}^3F^\circ_2$	687.64	25	145425	$4d\ 4d\ {}^3F_4 - 4d\ 6p\ {}^3D^\circ_3$
733.03	18	136420	$4d\ 5s\ {}^3D_2 - 5s\ 4f\ {}^3F^\circ_3$	686.28	4	145713	$4d\ 4d\ {}^3F_3 - 4d\ 6p\ {}^3D^\circ_2$
731.98	2	136616	$4d\ 5s\ {}^3D_3 - 5s\ 4f\ {}^1F^\circ_3$	684.38	2	146118	$4d\ 4d\ {}^3F_2 - 4d\ 6p\ {}^3D^\circ_1$
731.12	10	136776	$4d\ 5s\ {}^3D_1 - 5s\ 4f\ {}^3F^\circ_2$	683.09	5	146394	$4d\ 4d\ {}^3F_2 - 4d\ 6p\ {}^3D^\circ_2$
726.99	5	137554	$4d\ 4d\ {}^3P_2 - 4d\ 6p\ {}^3D^\circ_2$	680.69	3	146910	$4d\ 4d\ {}^3F_2 - 4d\ 6p\ {}^3D^\circ_3$
724.40	12	138045	$4d\ 4d\ {}^3P_0 - 4d\ 6p\ {}^3D^\circ_1$				
724.30	15	138064	$4d\ 4d\ {}^3P_2 - 4d\ 6p\ {}^3D^\circ_3$; $4d\ 4d\ {}^3P_1 - 4d\ 6p\ {}^3D^\circ_2$				
723.59	15	138200	$4d\ 4d\ {}^1D_2 - 4d\ 6p\ {}^1D^\circ_2$				
723.13	4	138288	$4d\ 4d\ {}^3P_2 - 4d\ 6p\ {}^3P^\circ_1$				
720.96	2	138704	$4d\ 4d\ {}^3P_1 - 4d\ 6p\ {}^3P^\circ_0$				
720.50	5	138792	$4d\ 4d\ {}^3P_1 - 4d\ 6p\ {}^3P^\circ_1$				
720.15	3	138860	$4d\ 4d\ {}^3P_2 - 4d\ 6p\ {}^3P^\circ_2$				

TABLE 7. *Zeeman patterns of* Zr III *lines*

A=shaded outward /|\; *B*=shaded inward |\/|.

Wavelengths	Term combinations	Observed Zeeman patterns	Derived *g*-values
A			
3497.78	$5s\ {}^1D_2 - 5p\ {}^1D^\circ_2$	(0.128) 0.993	1.070; 0.914
2836.18	$5s\ {}^3D_1 - 5p\ {}^1D^\circ_2$	(**0.000**, 0.422) . . . **1.336**	0.495; 0.914
2735.76	$5s\ {}^3D_3 - 5p\ {}^3F^\circ_3$	(0.438, **0.684**) 0.878, **1.104**, 1.345, 1.552	1.345; 1.104
2715.76	$5s\ {}^3D_2 - 5p\ {}^3D^\circ_1$	(0.000) 1.824	1.162; 0.500
2698.31	$5s\ {}^1D_2 - 5p\ {}^1P^\circ_1$	(0.000) 0.972	1,070; 1.266
2690.49	$5s\ {}^3D_1 - 5p\ {}^3F^\circ_2$	(**0.000**, 0.281) 0.791, **1.074**	0.495; 0.792
2686.28	$5s\ {}^3D_1 - 5p\ {}^3D^\circ_1$	(0.000) 0.506	0.495; 0.500
2682.16	$5s\ {}^3D_2 - 5p\ {}^3F^\circ_3$	(0.000) 1.040 *A*	1.162; 1.104
2664.26	$5s\ {}^1D_2 - 5p\ {}^1F^\circ_3$	(0.000) 1.020	1.070; 1.045
2656.46	$5s\ {}^3D_2 - 5p\ {}^3D^\circ_2$	(0.000) 1.166	1.162; 1.136
2643.79	$5s\ {}^3D_3 - 5p\ {}^3D^\circ_3$	(0.000) 1.341	1.345; 1.364
2628.26	$5s\ {}^3D_1 - 5p\ {}^3D^\circ_2$	(**0.000**, 0.666) 1.150, **1.788**	0.495; 1.136
2620.56	$5s\ {}^3D_3 - 5p\ {}^3F^\circ_4$	(0.000) 1.042 *A*	1.345; 1.224
2593.64	$5s\ {}^3D_2 - 5p\ {}^3D^\circ_3$	(0.000 *w*) 1.566 *B*	1.162; 1.364

TABLE 8. *Series terms of* Zr III

Terms	Limits in Zr IV	Relative term-values	Term separations	Distances to limits	Distances to ground state of Zr III	Distances between ground states of Zr III–Zr IV
		cm^{-1}	*cm*$^{-1}$	*cm*$^{-1}$	*cm*$^{-1}$	
$4d\ 4d\ {}^1G_4$	$4d\ {}^2D_{2\frac{1}{2}}$	11048	99579	192085	+9798	201883
$4d\ 5d\ {}^1G_4$		110627		92505		
$4d\ 4d\ {}^3F_2$	$4d\ {}^2D_{1\frac{1}{2}}$	0	107252	203530	0	203530
$4d\ 5d\ {}^3F_2$		107252		96278		
$4d\ 5s\ {}^1D_2$	$4d\ {}^2D_{2\frac{1}{2}}$	25065	85069	169981	+23815	193796
$4d\ 6s\ {}^1D_2$		110134		84912		
$4d\ 5s\ {}^3D_1$	$4d\ {}^2D_{1\frac{1}{2}}$	18398	86608	172357	+18398	190755
$4d\ 6s\ {}^3D_1$		105006		85749		
$4d\ 5p\ {}^1D_2^\circ$	$4d\ {}^2D_{2\frac{1}{2}}$	53646	90299	178028	+52396	230424 [a]
$4d\ 6p\ {}^1D_2^\circ$		143945		87725		
$4d\ 5p\ {}^3F_2^\circ$	$4d\ {}^2D_{1\frac{1}{2}}$	55555	89291	176479	+55555	230034 [a]
$4d\ 6p\ {}^3F_2^\circ$		144846		87188		
$5s\ 5s\ {}^1S_0$	$5s\ {}^2S_{0\frac{1}{2}}$	35501	106242	202031	−2757	199274
$5s\ 6s\ {}^1S_0$		141743		95789		
$5s\ 4d\ {}^1D_2$	$5s\ {}^2S_{0\frac{1}{2}}$	25065	114376	214028	−13193	200835
$5s\ 5d\ {}^1D_2$		139441		99652		
$5s\ 4d\ {}^3D_1$	$5s\ {}^2S_{0\frac{1}{2}}$	18398	118394	219902	−19860	200043
$5s\ 5d\ {}^3D_1$		136792		101507		

Mean Zr III–Zr IV = **198590**

Ionization potential = $198590 \times 1.2395 \times 10^{-4}$ = **24.6** ev

[a] Not included in the mean.

4. Discussion

The terms of Zr IV and Zr III recorded in tables 2 and 5 conform almost without exception to those required theoretically for atoms with 1 and 2 valence electrons. It is usually difficult to establish singlet terms with certainty if Zeeman patterns and inter-system combinations are missing. This is particularly true of the $^1S_0$ terms of Zr III for which, at most, only a few combinations can occur in the spectrum. It is always possible to find, in a complex spectrum, pairs of lines that exhibit wave-number separations in approximate agreement with the separations of established levels. If any such pairs are physically real, they should satisfy further requirements relative to the intensities of the lines and the way in which they fit into series. The $^1S_0$ terms in table 5 have been selected on the basis of such tests in the absence of the more convincing testimony of Zeeman observations.

A singlet term of Zr III that should be accepted with reserve is the one in table 5 designated as $4d\ 4f\ {}^1H_5^\circ$. It combines with the same levels as does $4d\ 4f\ {}^1G_4^\circ$ from which it is separated by only 180 cm^{-1}. Thus, it would violate the selection rule for inner quantum numbers if the assigned designation is correct. However, in the theoretical term-structure of the $4d\ 4f$ electron-configuration there is no room for an additional term with $J=4$. Careful combing of the spectrum for another term with $J=5$ has proved fruitless. We are left, therefore, with a choice of one of three possibilities: (1) the term labeled $^1H_5^\circ$ is correctly designated and violates the ΔJ rule; (2) it should be accepted as an unexplained level $^1X_4^\circ$; (3) the line at 839.55 A designated as $4d\ {}^3F_3-4f\ {}^1H_5^\circ$ should be regarded as fortuitously and not physically represented by this designation. If interpretation (3) is correct this line, with appearance similar to that of nearby lines of the $4d-4f$ group, would be left unexplained. Choice (2) does not seem warranted. In favor of the first choice is the fact that violations of the ΔJ rule are not unkown in other spectra as, for example, Paschen [6] pointed out in the case of the Hg II line at 2814.9 A.

Of the isoelectronic spectra Sr I, Y II, Zr III, Nb IV, and Mo V, the first is the only one in which series of three or more members have been found. In the other spectra of this sequence not more than two members of a series are known. The series limits that have been reported for the spectra following Sr I have been determined either with the Rydberg formula or with the irregular-doublet law. The

values of the limits thus derived with the one method are likely to be too high, and too low with the other. Although the limits of Zr III given in table 8 are undoubtedly too large, the amount by which they should be reduced can, at present, be only a matter of conjecture. Therefore, it is deemed preferable to offer these values only as provisional ones subject to revision when future data become available.

In the isoelectronic sequence of spectra from Rb I to Mo VI the only one with series of more than two members, following Rb I and Sr II, is Zr IV. As stated above the ^2S, $^2F°$, and ^2G series give concordant results in placing the ground state $4p\ ^2D_{1\frac{1}{2}}$ of Zr IV 276970 cm^{-1} from the ground state $^2S_0$ of Zr V, whereas the ^2D series gives a value about 18000 cm^{-1} greater. The series of Y III, Nb V, and Mo VI each consist of only two members. Although these series terms can be accurately represented with a simple Rydberg formula yet the limits calculated by this method are greater than those derived from application of the irregular-doublet rule to similar series of Rb I, Sr II, and Zr IV. It seems reasonable, therefore, to adopt for the limits provisional values that are means between the extreme values given by the different methods. When this is done and the results are compared with limits derived from the ^2D series, as in table 9, the differences between the convergences of the series are clearly revealed. These findings confirm Russell's statement that "Series involving changes in a *d* electron are usually very regular, except for the lowest term, when this involves the binding of the electron as part of an incomplete shell. In this case the energy of binding is considerably increased, and the application of a single Rydberg formula puts the limit a great deal too high."

The results presented in this paper could not have been achieved without the observational material supplied by Professors A. G. Shenstone, J. C. Boyce, and G. R. Harrison, as described above. To them I express my appreciation for their friendly cooperation, and also to C. H. Corliss, W. R. Bozman, and Miss Marion M. Harvey, of the Spectroscopy Section of the National Bureau of Standards, who assisted me with various phases of the observational and computational work of this investigation.

TABLE 9. *Absolute term values of* $^2D_{1\frac{1}{2}}$

Spectrum	From ^2S or $^2F°$ series	From ^2D series	Differences
Rb I	14336	14310 [a] 19780 [b]	−26 +5440
Sr II	74408	74428 [a] 76970 [b]	+20 +2560
Y III	168400	175080	+6680
Zr IV	276970	294850	+17880
Nb V	407700	433730	+26030
Mo VI	549000	589630	+40630

[a] Calculated with high series members (Rydberg formula).
[b] Calculated with first two series members (Rydberg formula).

5. References

[1] C. C. Kiess and R. J. Lang, BS J. Research **5,** 305 (1930) RP202.
[2] C. C. Kiess, J. Opt. Soc. Am. **44,** 823 (1954); Astron. J. **58,** 219 (1953).
[3] C. C. Kiess, J. Opt. Soc. Am. **43,** 1024 (1953).
[4] R. W. Wood, Nature **140,** 723 (1937).
[5] A. G. Shenstone, J. C. Boyce, and H. N. Russell, Rydberg interpolation table (Princeton University, 1934).
[6] F. Paschen, Akad. Wiss., Berlin, Sitz.-ber., Parts 31–33, p. 536 (1928).
[7] H. N. Russell, Astrophys. J. **66,** 233 (1927).

WASHINGTON, November 8, 1955.

Journal of Research of the National Bureau of Standards Vol. 56, No. 4, April 1956 Research Paper 2664

Frequency Conversion With Positive Nonlinear Resistors

Chester H. Page

A nonlinear resistor subject to an almost periodic voltage will absorb power at some frequencies, and supply power at other frequencies. Necessary and sufficient relations among these powers are found. Among the practical consequences are the results: (1) modulation efficiency cannot exceed unity, (2) subharmonics are not produced, and (3) the efficiency of generating an nth harmonic cannot exceed $1/n^2$.

1. Introduction

Positive nonlinear resistors are here defined as two-terminal devices through which the current (I) is a real finite single-valued nondecreasing function of the voltage (V) across the terminals, with the added condition that $I(0)=0$. The function $I(V)$ may have simple discontinuities.

The voltage is assumed to be uniformly almost periodic, i. e., a bounded continuous function of time representable by a uniformly convergent trigonometric series.

The resistor will absorb power, P_n (positive or negative), at each of the frequencies (ω_n) in the voltage. Relations among the P_n are of practical and theoretical interest.

The voltage can be thought of as supplied by a series-connected set of generators, some of which are real, whereas others represent the effects of voltage drop across the remaining passive elements of the network. Generators associated with positive P_n are called "sources"; those associated with negative P_n, "sinks." Continuity of $V(t)$ is provided physically by the inevitable shunt capacitance, however small, of the resistor.

$$V \equiv \sum_1^\infty V_n = \sum_1^\infty a_n \cos(\omega_n t + \theta_n). \tag{1}$$

The current through the resistor will be S^2 almost periodic,[1] as is shown in the appendix. It is given almost everywhere by

$$I(t) = \text{l. i. m.} \sum_1^\infty b_n \cos(\omega_n t + \varphi_n). \tag{2}$$

The frequencies ω_n may include some not required for the representation of V; these are included in eq (1) with vanishing coefficients. We denote the average power *absorbed* by the resistor at frequency ω_n by

$$P_n = \langle V_n I[V(t)] \rangle_t \equiv \lim_{T\to\infty} \frac{1}{2T} \int_{-T}^{T} V_n(t) I(t)\, dt. \tag{3}$$

2. Modulation

Partition the total voltage into two parts, a "carrier" (V_1) and the combination of signal and modulation products, such that

$$V = V_1 + V_2$$
$$\langle V_2 I[V_1] \rangle = 0 \tag{4}$$

defining as modulation products all frequencies (other than the signal) appearing in V but not in the current that obtains in the absence of signal.

[1] Representability by eq (2) is essentially what is meant by Stepanoff almost periodicity. See A. S. Besicovitch, Almost periodic functions, ch. II, sections 2 and 3 (Dover Publications, New York, N. Y., 1954).

THEOREM. *The sources in V_2 supply at least as much power as is absorbed by the sinks in V_2.* The total power supplied by the sources and sinks of V_2 is

$$\langle V_2 I[V_1+V_2]\rangle_t=\langle V_2\{I[V_1+V_2]-I[V_1]\}\rangle_t+\langle V_2 I[V_1]\rangle_t\geq 0. \tag{5}$$

The first term on the right is nonnegative by the nondecreasing property of I, and the second term vanishes by the definition of V_2.

The total power available in all modulation products is therefore not greater than that supplied by the signal source, or modulation efficiency cannot exceed unity.

3. Necessary Relations Among P_n

The total power absorbed by the resistor is

$$P=\langle VI\rangle_t\geq 0$$

as VI is a nonnegative function of t. Now

$$0\leq P=\langle VI\rangle_t=\langle \Sigma V_n I\rangle_t=\Sigma\langle V_n I\rangle_t=\Sigma P_n \tag{6}$$

by virtue of uniform convergence. Further,

$$P_n=\langle a_n\cos(\omega_n t+\theta_n)\Sigma b_m\cos(\omega_m t+\phi_m)\rangle_t=\tfrac{1}{2}a_n b_n\cos(\phi_n-\theta_n)$$

so that

$$|P_n|\leq\tfrac{1}{2}|a_n b_n|$$

making

$$\Sigma|P_n|\leq\tfrac{1}{2}\Sigma|a_n b_n|\leq\sqrt{(\tfrac{1}{2}\Sigma a_n^2)(\tfrac{1}{2}\Sigma b_n^2)}=\sqrt{\langle V^2\rangle\langle I^2\rangle}<\infty \tag{7}$$

using Schwarz's inequality and the boundedness of V and I. Similarly

$$\Sigma P_n^2\leq\tfrac{1}{4}\Sigma a_n^2 b_n^2\leq\tfrac{1}{4}(\Sigma|a_n b_n|)^2\leq\tfrac{1}{4}\Sigma a_n^2\Sigma b_n^2<\infty. \tag{8}$$

The final condition follows from the nondecreasing behavior of I:

$$\theta(x)\equiv\langle\{V(t)-V(t-x)\}\{I[V(t)]-I[V(t-x)]\}\rangle_t\geq 0. \tag{9}$$

Now

$$\begin{aligned}V(t)-V(t-x)&=\Sigma a_n\{\cos(\omega_n t+\theta_n)-\cos(\omega_n t-\omega_n x+\theta_n)\}\\&=\Sigma a_n\{[1-\cos\omega_n x]\cos(\omega_n t+\theta_n)-\sin\omega_n x\sin(\omega_n t+\theta_n)\}\end{aligned}$$

with a similar expression for $I(t)-I(t-x)$, making

$$\begin{aligned}\theta(x)&=\Sigma\tfrac{1}{2}a_n b_n\cos(\phi_n-\theta_n)\{(1-\cos\omega_n x)^2-\sin^2\omega_n x\}\\&=2\Sigma P_n(1-\cos\omega_n x).\end{aligned} \tag{10}$$

These results can be collected as the four conditions:

(a) $\Sigma P_n\geq 0$
(b) $\Sigma|P_n|<\infty$
(c) $\Sigma P_n^2<\infty$
(d) $\Sigma P_n(1-\cos\omega_n x)\geq 0$ all x.

4. Sufficiency

The above necessary conditions are also sufficient; given a set of ω_n and P_n satisfying $(a)-(d)$, there exists at least one combination of allowed voltage and resistor producing a set of P_n arbitrarily close to the specified values.

For consider the voltage

$$V=A^2\Sigma P_n \cos \omega_n t. \tag{11}$$

Condition (c) guarantees the Parseval equation and (b) makes V uniformly almost periodic. Condition (d) shows that V never exceeds its value at $t=0 (V_0=A^2\Sigma P_n)$ and condition (a) makes V_0 positive. Let V be applied across the resistor described by

$$I=\begin{cases} 0, & V\leq V_0-\delta \\ 1, & V>V_0-\delta \end{cases} \tag{12}$$

where δ is a small positive constant. There is a theorem [2] that V possesses translation numbers such that

$$|\omega_n \tau|<\epsilon \pmod{2\pi} \qquad \text{for } n<N; \tag{13}$$

hence a relatively dense set of time intervals for which $V_0-\delta<V<V_0$, yielding unit current. By setting $1/A^2$ equal to the fraction of the time that the current is unity, the power at ω_n is given by

$$P_n'=P_n \int_{I=1} \cos \omega_n t \, dt \Big/ \int_{I=1} dt, \tag{14}$$

that is, P_n'/P_n is equal to the average value of $\cos \omega_n t$ on the time intervals of unit current. This ratio can be made as close to unity as desired for any number (N) of frequencies, by reducing δ, for the continuity of V in eq (11) provides a continuous reduction of the intervals of integration. For $n>N$, the arithmetic error $P_n'-P_n$ can be made arbitrarily small by a sufficiently large choice of N, because by eq (14), $|P_n'/P_n|\leq 1$, and $\Sigma|P_n|$ converges.

5. Practical Theorems

Three practical theorems can be deduced directly from the necessary and sufficient relations among the P_n. For the modulation theorem, we consider a sinusoidal carrier and signal, so that all ω_n are of the form $n\omega_c+m\omega_s$, $(-\infty<n, m<\infty)$. Condition (d) yields

$$\Sigma\Sigma P_{nm}[1-\cos (n\omega_c+m\omega_s)x]\geq 0. \tag{15}$$

For $x=2\pi k/\omega_c$, k an integer, this becomes

$$\Sigma\Sigma P_{nm}[1-\cos 2\pi mk\omega_s/\omega_c]\geq 0 \tag{16}$$

and we can choose k to make the cosine less than ϵ for $m<M$ excepting the values $m=l\omega_c/\omega_s$, for which the cosine becomes unity. Therefore $\Sigma\Sigma P_{nm}\geq 0$, summing over all frequencies that are not harmonics of the carrier.

The second theorem states that subharmonics cannot be generated. Let τ be the least common period of the sources (or in general the least translation number of the source voltage). Then $P_n(1-\cos \omega_n\tau)$ vanishes for all positive P_n, and condition (d) requires this expression to vanish for each of the negative P_n. Hence all sinks have the period τ; all generated frequencies are harmonics of difference frequencies.

The third theorem limits the efficiency of harmonic generation to $1/n^2$. For

$$P_1(1-\cos \omega x)-|P_n|(1-\cos n\omega x)\geq 0$$

making

$$\frac{|P_n|}{P_1}\leq \frac{1-\cos \omega x}{1-\cos n\omega x}=\frac{\sin^2 \omega x/2}{\sin^2 n\omega x/2}. \tag{17}$$

[2] A. S. Besicovitch, Almost periodic functions, p. 53 (Dover Publications, New York, N. Y., 1954).

As $x \to 0$, the ratio of sines squared goes to its minimum value of $1/n^2$.

The positive definite form (d) can be generalized:

THEOREM. *If* $g(\omega) = \omega \int_0^\infty \varphi(x) \sin \omega x \, dx$, *where* $\varphi(x)$ *is a nonincreasing positive function, and the integral is summed in the Cesàro sense, then* $J[g] \equiv \Sigma g(\omega_n) P_n$ *is positive definite.*

For

$$g(\omega) = \lim_{\lambda \to \infty} \int_0^\lambda (1 - x/\lambda) \varphi(x) d(1 - \cos \omega x)$$

$$= \lim_{\lambda \to \infty} \left\{ \frac{1}{\lambda} \int_0^\lambda \varphi(x)(1 - \cos \omega x) dx + \int_0^\lambda (1 - x/\lambda)(1 - \cos \omega x)(-d\varphi) \right\} \tag{18}$$

upon integrating by parts. Then

$$J[g] = \lim \frac{1}{\lambda} \int_0^\lambda \varphi(x) \Sigma P_n (1 - \cos \omega_n x) dx + \lim \int_0^\lambda (1 - x/\lambda) \Sigma P_n (1 - \cos \omega_n x)(-d\varphi) \tag{19}$$

using the uniform convergence of (d). By (d) and the restrictions on φ, there are no negative terms on the right, so

$$J[g] \geq 0. \tag{20}$$

COROLLARY:

$$J(\alpha) \equiv \Sigma \omega_n^\alpha P_n \geq 0 \qquad \text{for } 0 \leq \alpha < 2.$$

In this range of α, J vanishes only for the trivial case of all P_n zero. The closure $J(2)$ is positive semidefinite; it vanishes for $V = \sin^3 \omega t$, $I(V) = 0$ for $V \leq 0$, $I(V) = 1$ for $V > 0$.

6. Appendix

Let $I(V)$ have only a finite number of simple discontinuities in any finite range of V. Let these be at the points V_i. Let $0 < \delta <$ g.l.b. $|V_i - V_j|$ and let l.u.b. $|I(V+\delta) - I(V)| = B$ so that for any $0 < \epsilon < \delta$, $|I(V+\epsilon) - I(V)| \leq B$. For $|V - V_i| > \delta$, I is continuous in the interval $[V, V \pm \epsilon]$, and ϵ can be chosen to make $|I(V \pm \epsilon) - I(V)| < \zeta$, where ζ is any assigned positive number. Therefore,

$$|I(V \pm \epsilon) - I(V)| \leq \begin{cases} \zeta, & |V - V_i| > \delta \\ B, & |V - V_i| \leq \delta. \end{cases}$$

Now if $V(t)$ is uniformly almost periodic, but not periodic, we can choose δ so that on the interval $t_0 \leq t \leq t_0 + l$, the measure of t for which $|V - V_i| \leq \delta$ is less than $l\zeta^2$.
Then

$$\frac{1}{l} \int_{t_0}^{t_0+l} |I[V(t) \pm \epsilon] - I[V(t)]|^2 dt \leq B^2 \zeta^2 + \zeta^2$$

and

$$\text{l.u.b.}_{-\infty < t_0 < \infty} \left\{ \frac{1}{l} \int_{t_0}^{t_0+l} |I[V(t) \pm \epsilon] - I[V(t)]|^2 dt \right\}^{1/2} < \zeta \sqrt{B^2 + 1}$$

Now the translation numbers τ of $V(t)$ make $|V(t+\tau) - V(t)| < \epsilon$ so that

$$\text{l.u.b.} \left\{ \frac{1}{l} \int_{t_0}^{t_0+l} |I[V(t+\tau)] - I[V(t)]|^2 dt \right\}^{1/2} < \zeta \sqrt{B^2 + 1}$$

and $I(t)$ is Stepanoff almost periodic, with a Fourier Series which converges to $I(t)$ in the mean square.

If $V(t)$ is periodic, then $I(t)$ is also periodic, hence Stepanoff a. p. a fortiori.

WASHINGTON, December 19, 1955.

Journal of Research of the National Bureau of Standards Vol. 56, No. 4, April 1956 Research Paper 2665

Electrical Resistivity of Vitreous Ternary Lithium-Sodium Silicates

Simon W. Strauss[1]

Resistivities of vitreous lithium disilicate, sodium disilicate, and selected ternary lithium-sodium silicates were measured in the range 150° to 230° C. The resulting data are given as log resistivity-composition isotherms. A correlation between heats of activation and composition is also presented. The composition containing approximately equimolar quantities of lithium oxide and sodium oxide showed a maximum value on the resistivity-composition isotherms as well as on the heat of activation-composition curve. The resistivities of the glasses were interpreted in terms of the structure of glass.

1. Introduction

Developments in electronic and related fields have emphasized the need for electrical insulating materials that can be used at elevated temperatures. Results of an investigation conducted in this laboratory showed that ceramic coatings merit serious consideration in the field of high-temperature electrical insulation [1].[2] From the standpoint of high electrical resistivity, alkali-free ceramic coatings are preferable to those containing alkali ions. In some cases, however, where the fusion point of the frit is high, some alkali ions are added in order to obtain workable coatings. In these instances it would be desirable to add alkali ions in such proportions as to minimize their effect upon resistivity and still yield a workable coating.

Some investigators have conducted studies on the electrical properties of glasses containing two species of alkali ions [2,3,4,5]. Their data indicated that when a mixture of two alkali ions was substituted for the same mole percent of either one, values for dielectric constant or loss when plotted against composition showed a minimum on the curve. Electrode potential and resistivity showed a maximum value on a property-composition curve. Dale, Pegg, and Stanworth [2] studied the electrical properties of five compositions in the system $50SiO_2$:-$18B_2O_3$:$5Al_2O_3$:$(27-x)Li_2O$:xNa_2O. Their data on the room-temperature resistivities indicated that the glass that contained equimolar quantities of sodium oxide and lithium oxide showed a maximum value on the resistivity-composition curve. It was considered desirable to study a three-component, lithium-sodium silicate system instead of a five-component system such as the one cited, because any effects produced by the presence of additional oxides would be eliminated. The data obtained on a three-component system should therefore lend themselves more readily to interpretation. The present paper describes results obtained on glasses in the system xLi_2O:$(1-x)Na_2O$:$2SiO_2$ whose resistivities were measured in the range 150° to 230° C.

2. Experimental

The materials used were reagent grade lithium carbonate and sodium carbonate, and quartz crystals [6] pulverized to pass a U. S. Standard No. 40 sieve. The batch compositions of the glasses are given in table 1. The method of preparing the experimental batches, the test equipment used to measure the resistivities of the glass specimens, and the method of test have been described in detail elsewhere [6]. Measurements were made at 10 deg C intervals in the range 150° to 230° C. A 200-v battery line was used as the emf source. The resistivity values were calculated from the current, voltage, and dimensions of the specimens. Values for heats of activation, ΔH^*, were calculated from the slopes of curves obtained by plotting log resistivity against the reciprocal of the absolute temperature.

TABLE 1. *Batch compositions of glasses in the system* xLi_2O:$(1-x)Na_2O$:$2SiO_2$

Composition No.	Oxide		
	Li_2O	Na_2O	SiO_2
	Mole	*Mole*	*Mole*
1	1.00	0.00	2.00
2	.90	.10	2.00
3	.85	.15	2.00
4	.80	.20	2.00
5	.75	.25	2.00
6	.70	.30	2.00
7	.65	.35	2.00
8	.60	.40	2.00
9	.55	.45	2.00
10	.50	.50	2.00
11	.45	.55	2.00
12	.40	.60	2.00
13	.35	.65	2.00
14	.30	.70	2.00
15	.25	.75	2.00
16	.20	.80	2.00
17	.10	.90	2.00
18	.00	1.00	2.00

[1] Present address Naval Research Laboratory, Washington, D. C.
[2] Figures in brackets indicate the literature references at the end of this paper.

3. Results and Discussion

Figure 1 gives resistivity-composition isotherms at 150, 200, and 230° C for vitreous lithium disilicate, sodium disilicate, and selected lithium-sodium silicates. A heat-of-activation–composition curve for these glasses is given in figure 2. These curves show that resistivities and heats of activation of the ternary compositions are higher than those of the binary glasses, the values, in each case, reaching a maximum for a glass containing approximately equimolar quantities of lithium oxide and sodium oxide. The position of the resistivity maximum is close to that reported for the five-component lithium-sodium-aluminum borosilicate [2]. The data show that two compositions, one on each side of the maximum on the curve, can yield glasses having a given resistivity. This observation holds true for compositions whose resistivity values are equal to or greater than that of lithium disilicate.

The fact that the resistivities of the ternary compositions were higher than those of the binary glasses, even though the total number of ions was kept constant for all glasses, suggests that a tightening of the structure probably occurred in the ternary glasses. Smyth [3], in discussing the distribution of size of interstices in glass, states: "Because of the irregularity of the vitreous structure there should be quite a wide spread in size of the interstices." As a first approximation, Smyth assumes a Gaussian distribution. Applying such reasoning to explain why a mixture of two alkali ions in a glass gives much lower dielectric losses than the same concentration of one alkali, he stated: "When a mixture of two ions is substituted for the same mole percent of either one, the smaller quantities of each separate ion can find interstices which come close to fitting them and the number left in interstices too large for them is much smaller than when either single ion is used." In this connection Stevels [5], in discussing dielectric losses in glasses, stated: "If in a glass containing only one kind of network modifier, some of these ions are replaced by other network modifiers having a different radius, then a more compact network can be obtained." Hence, both Smyth and Stevels suggested that a more compact structure results when a mixture of two alkali ions is substituted for the same mole percent of either one. The more compact packing in a lithium-sodium silicate over that in a binary silicate may be expected to increase the activation energy and make it more difficult for the ions to migrate through the structure. This assumption is consistent with the data presented in figures 1 and 2. Following the reasoning presented by Smyth and by Stevels, the maxima on both the resistivity-composition and heat-of-activation–composition curves suggest that a lithium-sodium silicate containing approximately equimolar quantities of lithium oxide and sodium oxide has a more compact structure than that of any other composition in the system $x\mathrm{Li_2O}:(1-x)\mathrm{Na_2O}:2\mathrm{SiO_2}$.

Because ternary lithium-sodium silicates had higher resistivities than the binary compositions, the question arises whether quaternary alkali silicates would have still higher resistivities. By analogy with Smyth's reasoning, it might be expected that when a mixture of three alkali ions is substituted for any of the three, the smaller quantities of each separate ion should find interstices that come close to fitting them, and the number left in interstices too large for them should be smaller than when

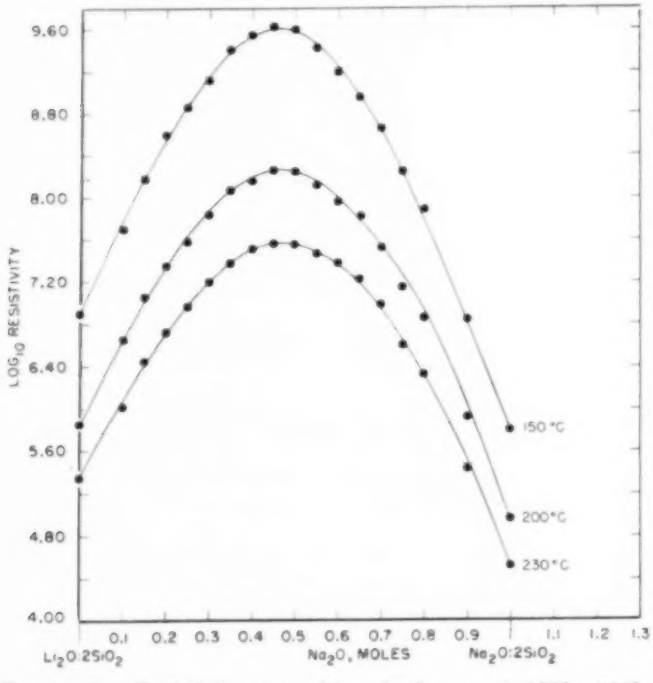

FIGURE 1. *Resistivity-composition isotherms at 150°, 200°, and 230° C for glasses in the system* $x\mathrm{Li_2O}:(1-x)\mathrm{Na_2O}:2\mathrm{SiO_2}$ *where x ranges from 0 to 1.*

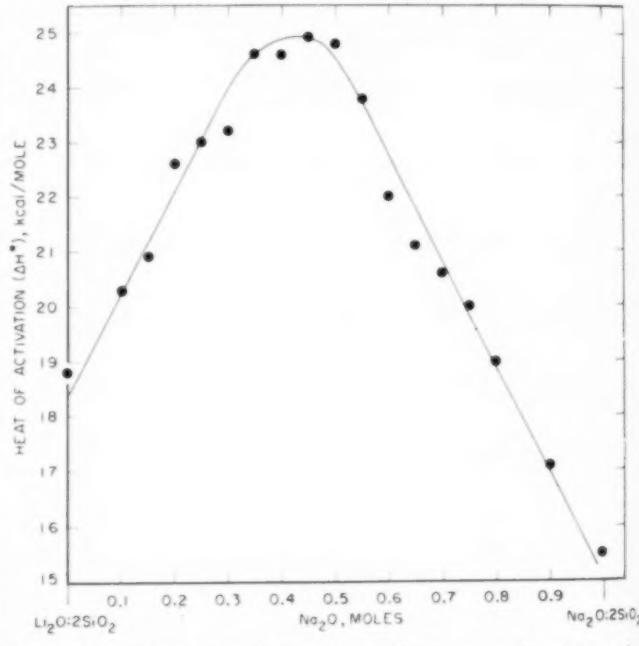

FIGURE 2. *Heat of activation-composition curve for glasses in the system* $x\mathrm{Li_2O}:(1-x)\mathrm{Na_2O}:2\mathrm{SiO_2}$ *where x ranges from 0 to 1.*

either single ion is used or when two alkali ions are used. Results obtained on glasses in a system such as $xLi_2O{:}yNa_2O{:}(1-x-y)K_2O{:}2SiO_2$ should clarify this point. Such a study should yield information that would be useful not only in the elucidation of the structure of glass but also in the design of glasses and ceramic coatings of specified resistivities. In this connection it would also be desirable to study systematically the resistivities of alkali-free glasses in which a nonalkali ion is replaced by the same mole percent of two or more isovalent ions.

4. Summary

Resistivity data were presented for sodium disilicate, lithium disilicate, and a series of 16 ternary lithium-sodium silicates prepared by the substitution of sodium oxide for lithium oxide in a base composition $Li_2O{:}\ 2SiO_2$.

The results were interpreted on the basis that the substitution of two alkali ions for the same mole percent of either one leads to a more compact structure which decreases ionic migration.

The variation in resistivity with change in composition was found to be similar to that reported by Dale, Pegg, and Stanworth [2] in their study of five compositions in the five-component lithium-sodium-aluminum borosilicate system. In addition, it was found in the present investigation that the heats of activation varied with change in composition in the same manner as did the resistivity.

5. References

[1] S. W. Strauss, L. E. Richards, and D. G. Moore, Effect of temperature on the electrical resistivity of several ceramic and silicone-type coatings, ASTM Sp. Tech. Publ. No. 153, 101–8 (1953).

[2] A. E. Dale, E. F. Pegg, and J. E. Stanworth, The electrical properties of some lithia containing glasses, J. Soc. Glass Technol. **35,** 136 (1951)..

[3] H. T. Smyth, Dielectric losses in glass, Tech. Rept. No. 9 (Rutgers University, 1955).

[4] M. Tashiro, Measurement and evaluation of electrical potentials between glasses, ONR Tech. Rept. No. 60 (1954).

[5] J. M. Stevels, Dielectric losses in glasses, Philips Tech. Rev. **13** [2], 365 (1952).

[6] S. W. Strauss, D. G. Moore, W. N. Harrison, and L. E. Richards, Fundamental factors controlling electrical resistivity in vitreous ternary lead silicates, J. Research NBS **56,** 135 (1956) RP2658.

Washington, December 23, 1955.

Journal of Research of the National Bureau of Standards Vol. 56, No. 4, April 1956 Research Paper 2666

Isothermal Compressibilities of Alkaline Earth Oxides at 21° C

C. E. Weir

Compression measurements were made by the piston-displacement method on powdered alkaline earth oxides at 21° C at 1,000-atmosphere intervals for pressures between 2,000 and 10,000 atmospheres. Pressure volume data are linear within experimental error. Compressibilities, β, and standard deviations of compressibilities, σ, in units of 10^{-6} per atmosphere are as follows: BeO, $\beta=0.27$, $\sigma=0.04$; MgO, $\beta=0.60$, $\sigma=0.12$; CaO, $\beta=0.89$, $\sigma=0.04$; SrO, $\beta=0.84$, $\sigma=0.10$; BaO, $\beta=1.76$, $\sigma=0.05$. Some abnormality in compressibility behavior for CaO and SrO is noted. This is probably related to a similar abnormality in densities.

1. Introduction

In a recent study [1][1] of the behavior of the binary alkaline earth borate glasses under high pressures, it was noted that data on the compressibilities of the alkaline earth oxides were largely unavailable. Bridgman [2] has reported data on the compressibility of a large crystal of MgO and on compacted powders of MgO and CaO. Measurements on the powders were made without a confining liquid, pressure being applied directly on the compacted powder. The result for powdered MgO was much greater than for the single crystal; thus, the validity of the data for powdered CaO is doubtful. Madelung and Fuchs reported earlier on MgO [3].

As all the alkaline earth oxides except BeO form cubic crystals, the system is of considerable theoretical interest and has been treated by Mayer and Maltbie [4], using the methods developed by Born and Mayer [5] and by Sherman [6]. Because compressibility data were unavailable, Mayer and Maltbie assumed a repulsion term similar to that found in the alkali halides [5]. Their calculations then led to negative electron affinities for oxygen and sulfur. Compressibility data on the alkaline earth sulfides, selenides, and tellurides, also generally cubic, have been reported by Bridgman [7].

The present report describes the results of measurements of compressibilities of the alkaline earth oxides at 21° C at pressures up to 10,000 atm.

2. Experimental Method and Materials

Methods used in measuring compressions have been described in detail in an earlier paper [8]. All oxides were in powder form and were contained in a small stainless-steel cylinder that was open at one end. The reference run was made using the same cylinder, containing a steel bar having a volume similar to that of the powdered oxides.

All oxides except BaO were prepared at temperatures of at least 1,000° C and were cooled in a sealed container to minimize absorption of moisture from the atmosphere. The weighed cylinder was packed with oxide in the partly opened container, and the oxide was compacted in the cylinder with a steel ram rod. Early attempts to perform these operations in a dry box showed that the necessary manipulations could not be conveniently carried out under such conditions. The tube was reweighed after packing with oxide and immediately subjected to a vacuum (approximately 0.1 mm of Hg) produced by a mechanical pump. Following at least 4 hr under vacuum, a sufficient quantity of a light petroleum distillate (Varsol) to completely cover the tube was admitted to the evacuated system. The liquid used had previously been dried with the particular oxide under study. The specimen was permitted to remain under liquid for 1 hr at 1 atm, to assure penetration of the voids by the liquid before compression measurements were conducted. Following compression, the tube and contents were weighed in dry liquid to permit calculation of the volume of the powder. Each oxide was studied in at least two separate measurements, using freshly prepared material for each run.

Immediately after the cylinder had been packed with the compression specimen, a portion of the residual oxide was taken for quantitative analysis for anion impurities. This specimen was expected to contain more moisture and CO_2 than the one used for compression, because it was exposed for a longer period. Analyses on all specimens were conducted volumetrically. Approximately 0.1 g of oxide was weighed out and treated with 100 ml of water. Excess standard sulfuric acid was added and the mixture digested several days on a steam bath with frequent agitation, more acid being added if required to maintain an acid solution. Following digestion the excess acid was back titrated with standard alkali and the weight of the specimen as oxide was calculated. The ratio of calculated to measured weights was considered to give an estimate of the purity.

[1] Figures in brackets indicate the literature references at the end of this paper.

2.1. Preparation and Analysis of Oxides

BeO—Beryllium oxide was a commercial material of fluorescent grade and was fired at 1,000° C for 16 hr in platinum prior to use. No analysis was performed because of the high purity of this specimen and the relative inertness of BeO toward water and carbon dioxide.

MgO—Reagent grade MgO was fired at 1,000° C for 16 hr in platinum. Analysis showed 97.5 percent of MgO.

CaO—Reagent grade $CaCO_3$ was fired at 1,200° C for 24 hr in platinum to prepare CaO. Analysis showed 97.8 percent of CaO.

SrO—Strontium oxide was prepared by firing $Sr(IO_3)_2$ for 1 week in porcelain. Starting temperature was 600° C and the final firing was at 1,000° C for 72 hr. $Sr(IO_3)_2$ was prepared from reagent grade $SrCl_2$ and I_2O_5. Analysis gave 98.0 percent of SrO. One impurity was $Sr(IO_3)_2$ in very small quantity because the iodine liberated from excess KI by 0.2 g of the specimen was discharged by 1 drop of 0.1 N thiosulfate.

BaO—High-purity barium oxide was not prepared. All attempts to prepare this material gave relatively impure products originating from the attack of the highly corrosive barium compounds on the containers. The specimen studied was obtained commercially and was observed to contain small amounts of sulfides and colored cations. Analysis showed 98.4 percent of BaO.

3. Results and Discussion

The average experimental compression data for each oxide are given in table 1. Individual measurements usually agreed to approximately ±0.0004 in.$-\Delta V/V_0$ [9] but many instances of deviations of greater magnitude were observed. These may be attributed to the small quantity of specimen used, approximately 4 cm^3, and the relatively low compressibility of the specimens. In the more incompressible oxides, some tendency for compression values to decrease at the higher pressures is observed. A similar behavior is to be noted in the experimental data obtained on diamond by Adams [10], but the cause of this behavior is not known. It is probably to be attributed to experimental errors inherent in measuring such small compressions.

TABLE 1. *Compression data for alkaline earth oxides*

Pressure	Compression, $-\Delta V/V_0$				
	BeO [a]	MgO [b]	CaO [a]	SrO [b]	BaO [a]
atm					
10,000	0.00190	0.00614	0.00768	0.00666	0.01426
9,000	.00155	.00405	.00635	.00654	.01277
8,000	.00228	.00472	.00576	.00528	.01113
7,000	.00199	.00389	.00492	.00474	.00952
6,000	.00122	.00319	.00399	.00367	.00750
5,000	.00068	.00246	.00290	.00260	.00564
4,000	.00036	.00193	.00226	.00190	.00393
3,000	.00018	.00083	.00123	.00119	.00196
2,000	.00000	.00000	.00000	.00000	.00000

[a] Average of 2 runs.
[b] Average of 3 runs.

Compressibilities were not determined from the average data of table 1, but were obtained by averaging the compressibilities, obtained from each measurement. To each set of experimental data a linear equation of the form $-\Delta V/V_0=a+b\ (P-2{,}000)$ was assumed to apply, and the value of b was determined by the method of least squares. A simple linear equation with no curvature term was considered to represent the data within the precision of the measurements. Individual values of b, the compressibility, were averaged for each oxide, and these results are shown in table 2 together with their standard deviations.

TABLE 2. *Compressibilities of alkaline earth oxides*

Oxide	Compressibility, average	Standard deviation of compressibility [a]
	atm^{-1}	atm^{-1}
BeO	[b] 0.27×10^{-6}	0.04×10^{-6}
MgO	[c] .50	.12
CaO	[b] .89	.04
SrO	[c] .84	.10
BaO	[b] 1.76	.05

[a] Computed from the formula $\sqrt{\Sigma(b-\bar{b})^2/(n-1)}$.
[b] Average of 2 slopes.
[c] Average of 3 slopes.

The only values in table 2 previously measured are those for MgO and CaO. Bridgman's value for single crystal MgO [2] is 0.59×10^{-6}/kg/cm^2 which agrees reasonably well with the value in table 2. However, his value of 4.57×10^{-6}/kg/cm^2 for compacted powdered CaO [2] is many times larger than that given in table 2. Madelung and Fuchs [3] reported 0.71×10^{-6}/megabar for MgO which is somewhat larger than found here. In general, it may be concluded that the low compressibilities shown in table 2 are what might be expected for these highly refractory oxides. The low compressibility of BeO is worthy of note. This low value is in concordance with the hardness of BeO as tabulated by Norton [11]. The compressibility of BeO is only slightly greater than diamond [10] and less than that of sapphire [12].

Mayer and Maltbie [4] in their discussion of the lattice energies of the alkaline earth oxides and sulfides concluded that the only available compressibility data for the oxides at that time [3] produced a repulsive exponent, ρ, which was somewhat too high. Accordingly they used a value of $\rho=0.345\times10^{-8}$ cm, which had been found by Born and Mayer [5] as the average value for the alkali halides. Born and Mayer, using an exponential repulsion term, deduced the following relationship for determining ρ:

$$-a\left(1+\frac{c_1}{c_2}e^{-2\delta/\rho}\right)\frac{M'c_2}{2M}e^{\left(\frac{\delta}{r_o}+1-\sigma\right)\frac{r_o}{\rho}}=\frac{\frac{r_o}{\rho}\frac{\tau}{\sigma}-1}{a\frac{r_o}{\rho}\frac{\tau}{\sigma}-1} \quad (1)$$

where a is the ratio of the distances of the next nearest to the nearest neighbors, c_1 and c_2 are constants in the repulsion potential defined by the equations

$$c_1=1+\frac{2Z_1}{N_1} \text{ and } c_2=1-\frac{2Z_2}{N_2}$$

where Z_1 and Z_2 are the electronic charges on the positive and negative ions and N_1 and N_2 the number of electrons in the exterior shells of positive and negative ions respectively, M' the number of nearest neighbors and M the number of next nearest neighbors, r_o is the lattice separation of the ions, δ is the difference in ionic radii $(r_{--}-r_{++})$, and τ and σ are defined by the equations

$$\tau=r_o\frac{dA(r_o)}{dr}-\frac{3T}{N\beta}\left(\frac{\partial V}{\partial T}\right)_P \tag{2}$$

and

$$\sigma=-r_o^2\frac{d^2A(r_o)}{dr^2}+\frac{9V}{N\beta}\left[1+\frac{T}{\beta}\left(\frac{\partial\beta}{\partial T}\right)_P + \frac{T}{\beta^2V}\left(\frac{\partial V}{\partial T}\right)_P\left(\frac{\partial\beta}{\partial P}\right)_T+\frac{2T}{3V}\left(\frac{\partial V}{\partial T}\right)_P\right]. \tag{3}$$

In eq (2) and (3), in addition to the customary terms, $A(r_o)$ is the coulomb attractive potential energy, N is Avogadro's number, β is the compressibility, and V is the molar volume. For these oxides $1/\beta(\partial\beta/\partial T)_p$ and $1/V(\partial V/\partial T)_P$ are all very small, and the last three terms in the bracket of eq (3) are neglected in comparison with unity. Using known values for the Madelung constant in $A(r_o)$, the values of β in table 2, and available values for the expansivities [13,14], τ and σ can be calculated. These values were substituted in eq (1), which was solved graphically to give the values for ρ shown in table 3. In solving eq (1), the ionic radii of Pauling [15] were used together with NBS values for the quantity r_o [16,17] for all oxides except BaO, for which data of Wykoff were taken [18].

TABLE 3. *Values of the repulsive exponent* ρ

Oxide	ρ
	cm
MgO	0.425×10^{-8}
CaO	.407
SrO	.337
BaO	.515
Avg	.421

Except for the value for SrO, the data for ρ in table 3 deviate considerably from the 0.345×10^{-8} cm assumed by Mayer and Maltbie [4]. However, the total repulsion energy of the crystals is rather small [4], and recalculation with the present data is not expected to change the data of Mayer and Maltbie [4] in any material manner.

Examination of the compressibilities of table 2 reveals an unexpected anomaly associated with CaO or SrO. It is anticipated that with increased atomic volume of cation, the compressibility should increase provided the anion remains constant and the crystals are isomorphic. Although the standard deviations of table 2 preclude an unequivocal conclusion that SrO is less compressible than CaO, it is certain that some irregularity in behavior exists. This irregularity is probably associated with an unexpectedly low density for CaO [16] compared with that of the other oxides [16,17]. Bridgman's earlier data on the sulfides [2] are also indicative of some nonuniformity in behavior, while Madelung and Fuch's [3] data on the compressibility of the isomorphic sulfates of calcium, strontium, and barium also show a minimum compressibility associated with strontium sulfate.

That an anomaly exists is shown by the fact that a similar minimum in density occurs at calcium throughout the isomorphic series of oxides, sulfides, selenides, and tellurides of the alkaline earths. That this behavior is in some manner associated with the position of calcium in the periodic system is indicated by the fact that a similar minimum density occurs for all alkaline earth sulfides, all alkali chlorides and all potassium halides. The sulfide, chloride, calcium, and potassium ions are all isoelectronic. The very high compressibility of potassium metal has been attributed by Bridgman [19] to an unusually open electronic structure. Presumably a similar explanation is to be sought for the ion itself and the other ions of an isoelectronic nature.

4. References

[1] C. E. Weir and L. Shartsis (in preparation).
[2] P. W. Bridgman, Proc. Am. Acad. Arts Sci. **67,** 345 (1932).
[3] E. Madelung and R. Fuchs, Ann. Physik **65,** 289 (1921).
[4] J. E. Mayer and M. McC. Maltbie, Z. Physik **75,** 748 (1932).
[5] M. Born and J. E. Mayer, Z. Physik **75,** 1 (1932).
[6] J. Sherman, Chem. Rev. **11,** 93 1932).
[7] P. W. Bridgman, Proc. Am. Acad. Arts Sci. **74,** 2 (1940).
[8] C. E. Weir, J. Research NBS **45,** 468 (1950) RP2160.
[9] C. E. Weir, J. Research NBS **52,** 247 (1954) RP2496.
[10] L. H. Adams and E. D. Williamson, J. Franklin Inst. **195,** 475 (1923).
[11] F. H. Norton, Refractories, 2nd Ed. (McGraw-Hill Book Co., New York, N. Y., 1942).
[12] P. W. Bridgman, Proc. Am. Acad. Arts Sci, **68,** 27 (1933).
[13] G. R. Rigby, Trans. Brit. Ceram. Soc. **41,** 123 (1941).
[14] A. Eisenstein, J. Appl. Phys. **17,** 434 (1946).
[15] L. Pauling, Nature of the chemical bond (Cornell University Press, Ithaca, N. Y., 1948).
[16] Standard X-ray diffraction powder patterns, NBS Circular 539, vol. I (June 15, 1953).
[17] H. E. Swanson (private communication).
[18] R. W. G. Wyckoff, Crystal structures, vol. 1, ch. III, table III (2) (Interscience Publishers, Inc., New York, N. Y., 1951).
[19] P. W. Bridgman, The physics of high pressure, 2d Ed., p. 183 (G. Bell & Sons, Ltd., London, 1949).

WASHINGTON, December 13, 1955.

Journal of Research of the National Bureau of Standards Vol. 56, No. 4, April 1956 Research Paper 2667

[1] Improved Synthesis of Sodium D-Glucuronate-6-C^{14} and of D-Glucose-6-C^{14}

R. Schaffer and H. S. Isbell

A process is reported for the synthesis of barium 1,2-*O*-isopropylidene-D-glucofururonate-6-C^{14} in 55 percent yield from 1,2-*O*-isopropylidene-D-*xylo*-dialdopentofuranose and sodium cyanide-C^{14}. The salt was converted to sodium D-glucuronate-6-C^{14} in 92 percent radiochemical yield and to D-glucose-6-C^{14} in 84 percent yield. The over-all radiochemical yield of D-glucose-6-C^{14} based on the sodium cyanide-C^{14} used was 45 percent in comparison with prior yields of approximately 15 percent.

1. Introduction

C^{14}-labeled glucuronic acid and D-glucose-6-C^{14} are in demand for biological and medical research but have not been generally available for lack of efficient methods of synthesis. Most of the material heretofore available was made by a procedure originated by Sowden [1].[2] The procedure begins with 1,2-*O*-isopropylidene-D-glucose and includes the intermediate production of a solution containing 1,2-*O*-isopropylidene-D-*xylo*-dialdopentofuranose, reaction of this solution with sodium cyanide-C^{14}, separation of 1,2-*O*-isopropylidene-D-glucofururonic acid, lactonization of the acid, and reduction of the lactone with either sodium borohydride or lithium aluminum hydride [2].

The method was modified by Shafizadeh and Wolfrom [3]. They avoided isolation of 1,2-*O*-isopropylidene-D-glucofururonic acid by lactonizing the acid mixture and separating the epimeric lactones by chromatography on clay. By use of this technique and a bicarbonate buffer in the cyanohydrin reaction they obtained crystalline 1,2-*O*-isopropylidene-D-glucofurano-γ-lactone in 15.5 percent yield and 1,2-*O*-isopropylidene-D-idurono-γ-lactone in 16 percent yield, based on the amount of cyanide used. The modification is a marked improvement over the original Sowden method which gave a 12.5 percent yield of only the glucuronic epimer, but it is scarcely suitable for the commercial production of D-glucose-6-C^{14}. It is therefore of interest to report a procedure developed at the National Bureau of Standards as part of a general program on the production of position-labeled sugars [4]. The procedure has been used for the preparation of D-glucose-6-C^{14} which has been supplied to numerous research groups in this country and abroad.

2. Discussion of the Process

Until recently the starting material for the synthesis, 1,2-*O*-isopropylidene-D-*xylo*-dialdopentofuranose, was known only as a sirup. It was first prepared by Iwadare [5] from 1,2-*O*-isopropylidene-D-glucofuranose by oxidation with lead tetraacetate. Later, oxidation with sodium metaperiodate was employed [6] and the sirupy product was used for the synthesis of 6-nitro-6-deoxyhexoses [7] and D-xylose-1-C^{14} [6] as well as for D-glucose-6-C^{14}. The sirupy product is not satisfactory for the synthesis of labeled sugars because it contains formaldehyde derived from the glycol oxidation. The formaldehyde may be combined with the sugar; in any case, it adheres tenaciously to the product. In the present investigation the last trace of formaldehyde was removed by crystallization of the product from water.

Crystalline 1,2-*O*-isopropylidene-D-*xylo*-dialdopentofuranose has been extensively studied and used at the National Bureau of Standards since 1952. The product that crystallizes from water contains 1 mole of water for 4 moles of the aldehyde. The molecular weight determined from freezing point depressions indicates that the product is a dimer. By dissolution of the hydrate in benzene and subsequent crystallization, an anhydrous product was obtained. This substance appears to be the same as a crystalline product recently reported by Brocca and Dansi [8]. Both the hydrate and the anhydrous product are suitable raw materials for the present process. Use of a crystalline compound rather than a crude sirup for starting the process eliminates loss of labeled cyanide by reaction with impurities and greatly simplifies the synthesis.

In prior work on the labeled-sugar program it was found that the proportions of the epimers formed in the cyanohydrin reaction can be altered by use of suitable buffers [9]. To ascertain conditions for the optimum yield of glucuronic acid, a number of cyanohydrin reactions were conducted with the xylose derivative, in which several buffers and C^{14}-labeled cyanide were used. The conditions employed in these reactions (table 1) were developed in experiments with nonradioactive materials in which the reaction times for complete addition of cyanide and the conditions for hydrolysis of the cyanohydrins were studied. In the work with labeled cyanide the yield of glucuronic acid was determined by an isotope dilution technique. The

[1] Part of a project on the development of methods for the synthesis of radioactive carbohydrates, sponsored by the Atomic Energy Commission. The paper is based on work described in an AEC report.

[2] Figures in brackets indicate the literature references at the end of this paper.

TABLE 1. *Yields of 1,2-O-isopropylidene-D-glucuronate salts from cyanohydrin reactions as determined by isotope dilution analysis*

Part 1. Composition of the cyanohydrin reaction mixtures

Reaction mixture	1,2-*O*-Isopropylidene-D-*xylo*-dialdopentofuranose	Sodium cyanide $-C^{14}$	Sodium hydroxide	Other reagents	Water
	mM	*mM*	*mM*	*mM*	*ml*
I	0.110	0.089	0.30	0.37 $NaHCO_3$	3
II	.077	.060	.20	.54 $NaHSO_3$	3
III	.077	.060	.20	.54 HOAc	3
IV	.175	.160	.60	1.4 HOAc	5

Part 2. Conditions and results

Reaction mixture	Conditions for addition reaction		Conditions for hydrolysis			Radioactivity		Yield of glucuronate
	Temp.	Time	Time at 70° C	Na_2CO_3	Time at 100° C	$NaC^{14}N$	Glucuronate-6-C^{14}	
	°C	*Days*	*Hours*	*mM*	*Hours*	*μc/mM*	*μc/mg*	*Percent*
I	7 to 9	5	None	None	3	700	0.160 [b]	27
II	25 to 30	3	2	0.3	3	700	.152 [b]	38
III	25 to 30	14	2	.3	3	700	.173 [c]	44
IV	25 to 30	25	2 [a]	.7	2	700	.422 [c]	58

[a] 0.15 mM of Na_2SO_3 was added before heating was begun.
[b] Lithium 1,2-*O*-isopropylidene-D-glucuronate-6-C^{14} obtained by use of 100 mg of carrier.
[c] Barium 1,2-*O*-isopropylidene-D-glucuronate-6-C^{14} obtained by use of 125 mg of carrier.

results revealed that in the slightly acid solution of mixture IV the reaction is slow but the yield of glucuronic epimer is high, and that with an increase in alkalinity the yield decreases.

Under conditions ordinarily used for hydrolyzing nitriles in the cyanohydrin synthesis, the reaction mixture from the 5-*aldo*-xylose derivative turns dark brown and there is much decomposition. To avoid this complication it was found advantageous to start the hydrolysis at a relatively low temperature (70° C), and at a relatively low alkalinity. After partial hydrolysis, the alkalinity was increased by the addition of sodium carbonate and the temperature was raised to 100° C. It was also found that reaction mixtures containing sodium sulfite gave lighter colored solutions in the hydrolysis step than others. In the procedure finally developed, sodium sulfite is added prior to heating at 70° C and sodium carbonate prior to heating at 100° C. The course of the hydrolysis was followed by titration of the ammonia liberated, or qualitatively by use of moist *p*H test paper.

To provide a means for separating the epimeric acids formed in the hydrolyzate, the salts of 1,2-*O*-isopropylidene-D-glucuronic acid were studied. The previously known barium salt [10] and a new lithium salt were found to crystallize well and to be suitable for isolating 1,2-*O*-isopropylidene-D-glucuronic acid from the reaction mixture. The barium salt seems the more useful, but both salts gave clear-cut separations since the corresponding salts of iduronic acid do not crystallize.

In the procedure recommended for the production of labeled glucuronic acid, the cold hydrolyzate is passed through a column containing a cation exchange resin, and the effluent is neutralized immediately with barium hydroxide. An insoluble residue is separated by filtration and the aqueous filtrate is concentrated to crystallization of barium 1,2-*O*-isopropylidene-D-glucuronate. Separation of a pure crystalline salt of 1,2-*O*-isopropylidene-D-glucuronic acid makes isolation of crystalline 1,2-*O*-isopropylidene-D-glucuronic acid unnecessary, thus eliminating loss of product that would be caused by partial hydrolysis of the isopropylidene groups.

For the production of D-glucose-6-C^{14} the crystalline salt is converted to the acid by use of an ion-exchange resin. The solution containing the acid is lyophilized and the dry residue is lactonized by heating with toluene according to the method of Sowden [1]. Under these conditions there is little loss due to hydrolysis of the isopropylidene group. The lactonized isopropylidene derivative is reduced without isolation of the pure lactone with either sodium borohydride or with lithium aluminum hydride by the method of Roseman [2]. The isopropylidene-D-glucose-6-C^{14} thus obtained is converted to D-glucose-6-C^{14} by hydrolysis and the sugar is separated by crystallization in the usual manner.

For the production of glucuronates, or D-glucurone, the salt of 1,2-*O*-isopropylidene-D-glucuronic-6-C^{14} acid is heated with a sulfonic acid ion-exchange resin. This converts the salt to the acid and hydrolyzes the isopropylidene group. Sodium, potassium, and other salts of glucuronic acid are then obtained by neutralization of the acid with the corresponding base, followed by crystallization. The lactone (D-glucurone-6-C^{14}) is obtained by lyophilization of the aqueous acid, dissolution of the residue in Methyl Cellosolve (ethylene glycol monomethyl ether), and crystallization.

3. Experimental

3.1. 1,2-*O*-Isopropylidene-D-*xylo*-dialdopentofuranose

A stirred solution of 50 g of sodium metaperiodate and 400 ml of water in a 1-liter flask, surrounded by an ice bath, was treated during 30 min with 50 g of 1,2-*O*-isopropylidene-D-glucofuranose, added in small portions. After stirring an additional 20 min, the excess periodate was decomposed by the addition of ethylene glycol. The solution was concentrated by freeze drying and the residue was extracted with four 100-ml volumes of chloroform. The extracts were combined, clarified by filtration through carbon, and concentrated under reduced pressure to a heavy sirup. By dissolution of the sirup in 100 ml of water and reconcentration under vacuum, the chloroform was removed. The concentrate was dissolved in 50 ml of water, filtered, and stored in the refrigerator for several weeks. The crystals that formed were separated, washed with water, and then recrystallized from water to give 29.9 g of 1,2-*O*-isopropylidene-D-*xylo*-dialdopentofuranose hydrate. Additional hydrate crystallized after lyophilization of the mother liquors and dissolution of the residue in an equal weight of water.

Anal. Calculated for $C_5H_{12}O_5.\frac{1}{4}H_2O$: C, 49.9; H, 6.5.
Found: C, 50.1; H, 6.6.

The hydrate, which crystallizes from water as large prisms, had a molecular weight of 262 in formamide and of 253 in acetic acid as determined by the Beckman freezing-point method; these values correspond with the calculated value 257 for a dimer with one-half molecule of water of hydration. The product melted at 180° to 184° C when heated slowly from room temperature to the melting point. Immersion of a sample in a capillary tube into a bath whose temperature exceeds 145° C resulted in rapid melting with evolution of gas. The melt solidified and remelted below 184° C. The hydrate gave $[\alpha]_D^{20}$ of −25.6° at equilibrium in water.

By dissolving the hydrate in boiling benzene and cooling, needlelike crystals of anhydrous 1,2-*O*-isopropylidene-D-*xylo*-dialdopentofuranose were obtained. The crystals were separated, washed with a mixture of benzene and petroleum ether, and dried.

Anal. Calculated for $C_5H_{12}O_5$: C, 51.1; H, 6.4.
Found: C, 51.1; H, 6.4.

The anhydrous compound melted at 182° to 184° C, and in water solution at equilibrium $[\alpha]_D^{20} = -25.9°$. The substance had a molecular weight of 390 in acetic acid as determined by the Beckman freezing-point method. The calculated value for the dimer is 376. Brocca and Dansi [8] report a similar product with a melting point of 175° to 177° C and $[\alpha]_D^{30}$ of −26.6° at equilibrium.

3.2. Lithium 1,2-*O*-Isopropylidene-D-glucofururonate

To 5 ml of a stirred cold aqueous solution containing 1.08 g of 1,2-*O*-isopropylidene-D-glucurone was added 0.21 g of $LiOH.H_2O$. The solution became yellow and in a few moments crystals of the lithium salt appeared. After stirring for 10 min, 20 ml of ethanol was added dropwise during the next half hour. The slightly yellow crystals were separated, washed with 80 percent ethanol, and dried. They weighed 0.93 g. The product was dissolved in water, the solution was filtered through a bed of decolorizing carbon, and crystallization was induced by the gradual addition of ethanol. The crystals obtained were short colorless needles which did not melt below 240° C. $[\alpha]_D^{20} = -3.8°$ (*c*, 3; H_2O).

Anal. Calculated for $LiC_5H_{13}O_7$: Li, 2.9; C, 45.0; H, 5.5;
Found: Li, 2.9; C, 45.2; H, 5.6.

3.3. Yields of 1,2-*O*-Isopropylidene-D-glucuronate Salts from 1,2-*O*-Isopropylidene-D-*xylo*-dialdopentofuranose and C^{14}-labeled Cyanide

The compositions of the reaction mixtures are given in part 1 of table 1, and a summary of the conditions employed and the data from which the yields were calculated is given in part 2. The reactants of each mixture were combined as solutions and stored in stoppered containers at the indicated temperatures. At the end of the time allowed for completion of the addition reaction, mixtures II and III were warmed to 70° C, and mixture IV, after addition of sodium sulfite, was also heated to 70° C. Mixtures II, III, and IV were then treated with sodium carbonate and all four reaction mixtures heated in a boiling water bath to complete the hydrolysis of the cyanohydrins. Nonradioactive lithium 1,2-*O*-isopropylidene-D-glucuronate was added to I, II, and III as carrier; the corresponding barium salt to IV. After cooling in ice water each solution was passed through a column containing 5 ml of Amberlite 1R-120H resin.[3] The effluents of I, II, and III were neutralized with lithium hydroxide. Barium hydroxide was used for IV and the insoluble matter removed. The neutralized effluents were concentrated under vacuum until the onset of crystallization, warmed to redissolve any material that had separated, and then passed through a filter coated with decolorizing carbon. The filtrates were concentrated under an air stream, seeded with the appropriate isopropylidene-glucuronate salt, and, as the crystallizations proceeded, treated with small amounts of methanol. The products were washed with aqueous methanol and then recrystallized from water and methanol. The specific activities of the isolated salts are given in table 1 together with the calculated yields for each reaction mixture.

3.4. Barium 1,2-*O*-Isopropylidene-D-glucuronate-6-C^{14}

A solution of 5.0 mM of sodium cyanide containing 12.5 mc of C^{14} and 5 mM of sodium hydroxide in 25 ml of water was frozen on the side of a 200-ml flask. Twenty-five ml of an aqueous solution containing 1.11 g. of 1,2-*O*-isopropylidene-D-*xylo*-dialdopentofuranose was introduced and frozen in the flask. Finally 20 ml of 1.0 *N* acetic acid was added and the flask was securely stoppered and swirled until its contents were completely melted. After 25 days at room temperature the flask was opened, 0.252 g of Na_2SO_3 was added, and the slightly yellow solution was heated at 70° C for 2 hr. After the addition of 1.06 g of Na_2CO_3 the solution was refluxed for 2 hr, next cooled in an ice bath, and then passed through a column containing 50 ml of cation exchange resin (Amberlite 1R–120H) at ice temperature. The effluent, including washings, was delivered into a flask surrounded by ice, containing 7.88 g of $Ba(OH)_2.8H_2O$. A stream of gaseous carbon dioxide was next passed into the effluent until the solution was neutral and the insoluble material was separated by filtration.

Concentration of the filtrate under reduced pressure to about 60 ml resulted in the separation of an additional amount of precipitate. Refiltration yielded a solution which contained according to a radioassay 11.76 mc of C^{14}. A few seed crystals of

[3] Amberlite 1R-120-H, Resinous Products Division of Rohm & Haas Co., Philadelphia, Pa.

barium 1,2-*O*-isopropylidene-D-glucuronate [10] were added and the solution was then concentrated under a gentle stream of air. Large colorless crystals of labeled barium salt formed during the evaporation. They were separated from the mother liquor and washed several times with water and 50 percent methanol. Dissolution of the crystalline product in water, removal of a small amount of insoluble residue, and recrystallization yielded 0.690 g of barium 1,2-*O*-isopropylidene-D-glucuronate-6-C^{14} monohydrate containing 5.6 mc of radioactivity. Three 500-mg portions of nonradioactive barium salt used as carrier resulted in the isolation of 0.86 mc, 0.22 mc, and 0.07 mc of additional salt. The radiochemical yield (6.75 mc) amounted to 54 percent based on the $NaC^{14}N$ used. The mother liquor (5.0 mc) was set aside for separation of 1,2-*O*-isopropylidene-D-iduronate-6-C^{14}epimer.

3.5. Preparation of 1,2-*O*-Isopropylidene-D-glucuronolactone-6-C^{14} From Barium 1,2-*O*-Isopropylidene-D-glucuronate-6-C^{14}

Seventy ml of an ice-cold aqueous solution of 1.184 g of barium 1,2-*O*-isopropylidene-D-glucuronate-6-C^{14} monohydrate containing 6.5 mc of C^{14} was passed through a column containing 9 ml of ice-cold Amberlite 1R-120H. The effluent and washings were frozen and lyophilized. A volume of 100 ml of toluene was added to the sirup which remained after the lyophilization. The mixture was heated under a reflux condenser for 4 hr. Removal of the toluene by evaporation under a gentle stream of air left large crystals of 1,2-*O*-isopropylidene-D-glucurone-6-C^{14} mixed with some brown residue.

3.6. Preparation of D-Glucose-6-C^{14} From 1,2-*O* Isopropylidene-D-glucuronolactone-6-C^{14}

The crude 1,2-*O*-isopropylidene-D-glucurone-6-C^{14} described in the preceding paragraph was dissolved in approximately 70 ml of anhydrous diethyl ether and then added at a dropwise rate from a pressure-equalized dropping funnel to a flask containing 13.2 mM of lithium aluminum hydride in 30 ml of diethyl ether. The solution was stirred continuously with a magnetic stirrer. The residual labeled material was rinsed into the reduction flask with ether and the reaction mixture was refluxed for 30 min. Then 25 ml of anhydrous ethanol was added dropwise to the stirred reaction mixture, followed by 6 ml of glacial acetic acid and 130 ml of water. The supernatant ether was volatilized by a current of air. The resulting aqueous solution was passed into a column containing 100 ml of cation exchange resin (Amberlite 1R-120H). The effluent including wash liquor was concentrated at reduced pressure, 10 mM of aqueous sulfuric acid added, and the volume adjusted to 200 ml. The solution was heated for 2 hr in a boiling water bath, and, after cooling to room temperature was passed into a column containing, 40 ml of anion exchange resin.[4] The radioactive solution was washed from the resin, concentrated to about 50 ml filtered through a bed of decolorizing carbon and lyophilized. The residue was dissolved in the minimum quantity of methanol and the solution was filtered. Crystalline D-glucose-6-C^{14} was obtained after addition of 2-propanol to the point of incipient turbidity. Recrystallization yielded 485 mg of D-glucose-6-C^{14} with a specific radioactivity of 9.2 μc/mg. By the use of 2.0 g of carrier, an additional 993 μc of the labeled glucose was obtained. The chemical yield from the barium salt to the sugar was 69 percent; the radiochemical yield was 84 percent. The over-all radiochemical yield based on the sodium cyanide-C^{14} used was 45 percent.

3.7. Preparation of Sodium D-Glucuronate-6-C^{14} Monohydrate From Barium 1,2-*O*-Isopropylidene-D-Glucuronate-6-C^{14}

In a 100-ml flask equipped with a magnetic stirrer, an electric heater, and a reflux condenser, 896 mg of barium 1,2-*O*-isopropylidene-D-glucuronate (590 μc), 10 ml of Amberlite 1R-120H, and 40 ml of water were combined and heated to boiling for 50 min. The mixture was cooled, filtered through a small bed of resin, and washed. The filtrate was neutralized with sodium hydroxide, concentrated under reduced pressure, treated with decolorizing carbon, and then filtered. The concentrated filtrate was diluted with a few drops of ethanol, and seeded with crystals of sodium D-glucuronate monohydrate [11]. The resulting crystals were separated from the mother liquor and washed with aqueous ethanol. Recrystallization from aqueous ethanol yielded 595 mg of the monohydrate with a total radioactivity of 509 μc. By use of nonradioactive carrier an additional 34 μc of sodium D-glucuronate-6-C^{14} was obtained from the mother liquor. The radiochemical yield was 92 percent.

3.8. Preparation of D-Glucurone-6-C^{14} From Barium 1,2-*O*-Isopropylidene-D-Glucuronate-6-C^{14}

A solution of 927 mg of barium 1,2-*O*-isopropylidene-D-glucuronate-6-C^{14} (165 μc) in 50 ml of water, and 10 ml of Amberlite 1R-120H resin, was treated as described for the preparation of sodium D-glucuronate-6-C^{14}. After separation from the resin the solution was concentrated at reduced pressure, passed through a filter coated with decolorizing carbon, and then freeze-dried. The residue was dissolved in Methyl Cellosolve, and the solution was seeded with nonradioactive D-glucurone. Recrystallization gave 438 mg of D-glucurone-6-C^{14} with a total radioactivity of 133.5 μc. By use of carrier an additional 19.3 μc of labeled glucurone was obtained. The radiochemical yield was 93 percent.

4. Radioactivity Measurements

Determinations of C^{14} were made upon samples dissolved in formamide or in aqueous mixtures [12]. The radioactivities of the solutions were measured with a proportional beta counter.[5]

[4] Duolite A-4, Chemical Process Co., Redwood City, Calif.

[5] Nuclear Measurements Corporation, Indianapolis, Ind., Model PC-4.

The authors express their appreciation to R. A. Paulson for determinations of carbon and hydrogen, and to Harriet L. Frush and T. T. Galkowski who conducted some of the early development work.

5. References

[1] J. C. Sowden, J. Am. Chem. Soc. **74,** 4377 (1952).
[2] S. Roseman, J. Am. Chem. Soc. **74,** 4467 (1952).
[3] F. Shafizadeh and M. L. Wolfrom, J. Am. Chem. Soc. **77,** 2568 (1955).
[4] H. S. Isbell, J. V. Karabinos, H. L. Frush, N. B. Holt, A. Schwebel and T. T. Galkowski, J. Research N. B. S. **48,** 163 (1952) RP2301; H. S. Isbell and J. V. Karabinos, *ibid.*, **48,** 438 (1952) RP2334; H. L. Frush and H. S. Isbell, *ibid.*, **50,** 133 (1953) RP2400; *ibid.*, **51,** 167 (1953) RP2446; *ibid.*, **51,** 307 (1953) RP2458; H. S. Isbell, H. L. Frush and N. B. Holt, *ibid.*, **53,** 217 (1954) RP2536; *ibid.*, **53,** 325 (1954) RP2550; H. S. Isbell, H. L. Frush, and R. Schaffer, *ibid.*, **54,** 201 (1955) RP2581.
[5] K. Iwadare, Bull. Chem. Soc. Japan **16,** 40 (1941).
[6] J. C. Sowden, J. Am. Chem. Soc. **73,** 5496 (1951).
[7] J. M. Grosheintz and H. O. L. Fischer, J. Am. Chem. Soc. **70,** 1476 (1948).
[8] V. Brocca and A. Dansi, Ann. Chim. (Rome) **44,** 120 (1954).
[9] H. S. Isbell, U. S. Patent 2,606,918 (1952).
[10] C. L. Mehltretter, B. H. Alexander, R. L. Mellies, and C. E. Rist, J. Am. Chem. Soc. **73,** 2424 (1951).
[11] W. Hach and D. G. Benjamin, J. Am. Chem. Soc. **76,** 917 (1954).
[12] A. Schwebel, H. S. Isbell, and J. D. Moyer, J. Research NBS **53,** 221 (1954) RP2537.

Washington, November 23, 1955.

Journal of Research of the National Bureau of Standards Vol. 56, No. 4, April 1956 Research Paper 2668

Ideal Gas Thermodynamic Functions of the Isotopic Hydrogen Cyanides[1]

Joe C. Bradley, Lester Haar,[2] and Abraham S. Friedman

The ideal gas thermodynamic functions for HCN, DCN, and TCN were calculated from molecular data. The recent spectroscopic data for HCN and DCN by Allen [1][3] and Douglas and Sharma [2] were employed. The zero frequencies of TCN were obtained by a normal coordinate treatment. The partition functions are obtained in closed form. The calculations include high-temperature corrections for vibrational anharmonicity, rotation-vibration coupling, centrifugal stretching, and azimuthal quantum effects, and low-temperature corrections for nonclassical rotation. The statistical calculations were performed on the Standards Electronic Automatic Computer (SEAC). Tables of C_p°/R, $(H^\circ-E_0^\circ)/RT$, $-(F^\circ-E_0^\circ)/RT$, and S°/R have been calculated at small temperature intervals from 50° to 5,000° K.

1. Introduction

The procedure developed in earlier papers [3,4,5] for high-speed machine computation of the thermodynamic functions of molecules in the ideal gas state was used. The partition function is written in a factored form to include corrections for vibrational anharmonicity, rotation-vibration coupling, centrifugal stretching, nonclassical rotation, and azimuthal quantum effects. The expression for the factored internal partition function is

$$Q=\frac{1}{S}\left[\prod_i(1-e^{-u_i})^{d_i}\right]\left[\frac{kT}{hcB_e}\right]\left[1+\rho T\right]\left[\prod_i\left(1+\frac{d_i\delta_i}{e^{u_i}-1}\right)\right]\left[\prod_{i\le j}(1+f_{ij})\right]\left[1+\frac{\theta_1}{T}+\frac{\theta_2}{T^2}\right]$$

where

$$\rho=(2kD)/hcB_e^2,$$

$$\theta_1=\frac{1}{3}(hcB_e)/k, \theta_2=\frac{1}{15}(hcB_e/k)^2$$

and

$$f_{ij}=\frac{d_i(d_j+\delta_{ij})X'_{ij}(hc/kT)}{(e^{u_i}-1)(e^{u_j}-1)}, \quad X'_{ij}=X_{ij}+g_{ij}/3.$$

In these expressions the δ_i represent rotation-vibration coupling constants, the X_{ij} are the anharmonic constants, g_{22} is an anharmonic constant for the doubly degenerate vibration, ω_2, and δ_{ij} is the kronecker delta. Pennington and Kobe's method [6] of including the g_{22} term in the partition function was used. The other symbols and constants have their usual meaning (see e. g., [3]).

[1] This work was supported in part by the U. S. Atomic Energy Commission.
[2] Present address: Johns Hopkins University Applied Physics Laboratory.
[3] Figures in brackets indicate the literature references at the end of this paper.

2. Molecular Data

The vibrational data for HCN and DCN were recently obtained by Allen [1]. The rotational data for HCN and DCN were investigated by Douglas and Sharma [2]. The anharmonicity and rotation-vibration coupling constants were calculated for TCN using the isotope relations [3],

$$X'_{ij}=\left(\frac{\omega'_i\omega'_j}{\omega_i\omega_j}\right)X_{ij} \quad \text{and} \quad \delta'_i=\left(\frac{\omega'_i}{\omega_i}\right)\delta_i$$

where the primed quantities refer to the molecule whose X_{ij} or δ_i is to be calculated, and the unprimed quantities refer to the reference molecule. The X_{ij} and δ_i for TCN were calculated using HCN and DCN as reference molecules; the averages of these calculations were used in the tabulated results except for the constant X_{12} in which case DCN was used as a reference molecule. Approximating

$$f_{\substack{ij\\(i\neq j)}}=\frac{d_i(d_j+\delta_{ij})\dfrac{hc}{kT}X'_{ij}}{(e^{u_i}-1)(e^{u_j}-1)} \quad \text{by} \quad f_{\substack{ij\\(i\neq j)}}=\frac{d_i(d_j+\delta_{ij})\dfrac{hc}{kT}X'_{ij}}{(e^{u_k}-1)^2}$$

where $u_k^2=u_iu_j$ changes the correction factor f_{23} by 20 percent and the free energy by 1 part in 36,000 at 5,000°K. This effect is much less in the case of f_{13} and f_{12} (see [3]). The zero-order frequencies for TCN were obtained by a normal coordinate treatment.

The chemical atomic weights used in the calculations of the translational partition functions were obtained from the values listed by Wichers [7]. The isotopic mass used in the zero-point frequency and equilibrium moment of inertia calculation are listed by Mattauch and Fluegge [8]. The constants used are given in table 1.

TABLE 1. *Molecular constants*

	Units	HCN	DCN	TCN
ν_1	cm^{-1}	2100.24	1927.27	1723.90
ν_2	cm^{-1}	711.90	569.13	503.36
ν_3	cm^{-1}	3315.03	2632.33	2446.67
X_{11}	cm^{-1}	10.45	7.10	6.37
X_{22}	cm^{-1}	2.50	2.09	1.45
X_{33}	cm^{-1}	52.50	20.23	22.72
X_{12}	cm^{-1}	2.90	−2.73	−1.93
X_{13}	cm^{-1}	14.43	32.88	18.00
X_{23}	cm^{-1}	19.19	15.71	11.48
g_{22}	dimensionless	3.63	−2.00	−1.00
δ_1	dimensionless	0.00643	0.00518	0.00495
δ_2	dimensionless	−.0024	−.0035	−.0024
δ_3	dimensionless	.00727	.00854	.0066
I_e	$g\ cm^2 \times 10^{-40}$	18.846	23.093	27.029
θ_1	°K	0.7122	0.5812	0.4967
θ_2	$(°K)^2$	.2965	.1975	.1442
ρ	$(°K)^{-1} \times 10^{-6}$	1.79	1.99	1.88

3. Thermal Functions

The heat capacity, enthalpy, free energy, and entropy of HCN, DCN, and TCN are listed in tables 2, 3, and 4. The thermal functions are tabulated in dimensionless units at small intervals ranging from 50° to 5,000° K. These tables also include the first differences for the tabulated thermodynamic functions.

The uncertainty in the calculated vibrational anharmonicity and rotation-vibration coupling constants is approximately 25 percent except in the case of the anharmonic constant X_{12} for TCN in which case the sign of the constant cannot be satisfactorily predicted. The uncertainty in the vibrational and rotational fundamentals is less than 1 percent assuming negligible uncertainty in the calculated zero point vibrational frequencies. At temperatures below 1,000° K this will result in an uncertainty in the third place to the right of the decimal for the tabulated properties of these substances. The thermal functions are tabulated with more figures to permit intercomparison among the several isotopic modifications.

The contribution of the excited electronic states, significant only at the highest temperatures, have been neglected. The entropy contribution of isotopic spin and the entropy of isotopic mixing have been omitted.

Stamm, Halverson, and Whalen [9] have revised older tables of free energy for HCN which include corrections for vibrational anharmonicity, rotation-vibration coupling, centrifugal stretching, and a low-temperature correction. The results reported here are in excellent agreement with those of Stamm et al.

TABLE 2. *Ideal gas thermodynamic functions for* HCN

°K	$\frac{C_p^\circ}{R}$		$\frac{(H^\circ - E_0^\circ)}{RT}$		$\frac{-(F^\circ - E_0^\circ)}{RT}$		$\frac{S^\circ}{R}$	
50	3.50020	4	3.48581	240	14.22796	63576	17.71377	63816
60	3.50025	19	3.48821	173	14.86372	53784	18.35194	53957
70	3.50045	74	3.48994	135	15.40157	46610	18.89152	46746
80	3.50120	209	3.49129	119	15.86768	41128	19.35898	41248
90	3.50329	456	3.49249	128	16.27897	36803	19.77146	36931
100	3.50786	825	3.49378	162	16.64700	33306	20.14078	33468
110	3.51612	1301	3.49540	223	16.98007	30423	20.47547	30646
120	3.52913	1850	3.49763	309	17.28430	28007	20.78193	28317
130	3.54764	2431	3.50073	418	17.56437	25957	21.06511	26376
140	3.57195	3004	3.50491	543	17.82395	24199	21.32887	24743
150	3.60199	3539	3.51035	680	18.06595	22676	21.57630	23357
160	3.63739	4013	3.51716	823	18.29271	21346	21.80987	22169
170	3.67753	4415	3.52539	966	18.50618	20177	22.03157	21143
180	3.72168	4738	3.53505	1105	18.70795	19142	22.24301	20247
190	3.76906	4983	3.54611	1238	18.89937	18220	22.44548	19458
200	3.81890	5157	3.55849	1362	19.08157	17394	22.64007	18756
210	3.87047	5266	3.57212	1475	19.25552	16651	22.82764	18126
220	3.92313	5318	3.58687	1577	19.42203	15978	23.00891	17556
230	3.97632	5323	3.60265	1667	19.58182	15367	23.18447	17035
240	4.02955	5288	3.61933	1746	19.73549	14810	23.35482	16556
250	4.08243	5223	3.63679	1814	19.88359	14298	23.52039	16113
260	4.13467	5133	3.65494	1872	20.02658	13828	23.68153	15700
270	4.18600	5026	3.67366	1919	20.16487	13394	23.83854	15314
280	4.23627	4906	3.69286	1958	20.29882	12992	23.99169	14951
290	4.28534	4778	3.71245	1989	20.42875	12619	24.14120	14608
300	4.33313	4646	3.73235	2013	20.55494	12271	24.28729	14284
310	4.37959	4511	3.75248	2030	20.67765	11945	24.43014	13976
320	4.42471	4378	3.77279	2042	20.79711	11640	24.56990	13682
330	4.46849	4246	3.79321	2048	20.91352	11354	24.70673	13403
340	4.51096	4118	3.81370	2051	21.02706	11084	24.84076	13135
350	4.55215	3995	3.83421	2050	21.13791	10830	24.97212	12880
360	4.59210	3877	3.85471	2045	21.24621	10589	25.10092	12635
370	4.63088	3765	3.87517	2038	21.35210	10361	25.22727	12399
380	4.66853	3658	3.89555	2029	21.45572	10145	25.35127	12174
390	4.70511	3558	3.91584	2017	21.55717	9939	25.47301	11957
400	4.74069	16483	3.93602	9875	21.65656	46933	25.59259	56808
450	4.90553	14768	4.03477	9457	22.12590	43004	26.16068	52462
500	5.05321	13540	4.12935	9022	22.55594	39783	26.68530	48805
550	5.18861	12637	4.21957	8607	22.95378	37087	27.17335	45694
600	5.31499	11936	4.30565	8227	23.32465	34790	27.63030	43018
650	5.43435	11356	4.38792	7883	23.67256	32808	28.06048	40691
700	5.54792	10843	4.46675	7571	24.00064	31077	28.46740	38649
750	5.65636	10368	4.54247	7288	24.31142	29550	28.85389	36858
800	5.76004	9912	4.61535	7027	24.60692	28192	29.22228	35219
850	5.85917	9468	4.68563	6784	24.88885	26975	29.57448	33760
900	5.95386	9032	4.75347	6557	25.15860	25877	29.91208	32434
950	6.04418	8604	4.81905	6342	25.41738	24880	30.23643	31223
1000	6.13022	8184	4.88247	6138	25.66619	23971	30.54866	30109
1050	6.21207	7776	4.94386	5942	25.90590	23136	30.84976	29079
1100	6.28984	7381	5.00328	5755	26.13726	22368	31.14055	28123
1150	6.36365	7000	5.06084	5575	26.36095	21657	31.42179	27232
1200	6.43366	12921	5.11660	10637	26.57752	41379	31.69412	52016
1300	6.56287	11596	5.22297	9592	26.99131	39075	32.21428	49068
1400	6.67883	10409	5.32289	9392	27.38207	37047	32.70496	46440
1500	6.78293	9357	5.41682	8835	27.75255	35244	33.16937	44080
1600	6.87650	8431	5.50518	8318	28.10499	33627	33.61017	41945
1700	6.96081	7617	5.58836	7839	28.44126	32166	34.02963	40006
1800	7.03699	6906	5.66676	7396	28.7623 3	30838	34.42969	38235
1900	7.10605	6283	5.74073	6986	29.07131	29625	34.81204	36613
2000	7.16888	5737	5.81059	6606	29.36757	28511	35.17816	35118
2100	7.22626	5260	5.87666	6255	29.65268	27483	35.52934	33739
2200	7.27887	4840	5.93921	5931	29.92752	26532	35.86674	32464
2300	7.32727	4472	5.99853	5630	30.19285	25649	36.19138	31280
2400	7.37200	4147	6.05483	5352	30.44935	24826	36.50418	30179
2500	7.41347	3859	6.10836	5094	30.69761	24057	36.80598	29152
2600	7.45207	3605	6.15931	4855	30.93819	23337	37.09750	28192
2700	7.48812	3379	6.20786	4633	31.17156	22660	37.37943	27294
2800	7.52192	3177	6.25420	4426	31.39817	22024	37.65237	26451
2900	7.55370	2998	6.29846	4234	31.61841	21424	37.91688	25659
3000	7.58368	5528	6.34081	7943	31.83266	41179	38.17348	49123
3200	7.63897	5005	6.42025	7318	32.24446	39145	38.66471	46463
3400	7.68902	4577	6.49343	6771	32.63591	37309	39.12935	44080
3600	7.73479	4223	6.56114	6289	33.00901	35644	39.57015	41934
3800	7.77703	3928	6.62404	5864	33.36546	34127	39.98950	39992
4000	7.81631	3680	6.68268	5486	33.70673	32739	40.38942	38225
4200	7.85312	3469	6.73755	5150	34.03412	31463	40.77168	36613
4400	7.88781	3288	6.78905	4849	34.34876	30286	41.13781	35135
4600	7.92069	3132	6.83755	4578	34.65162	29198	41.48917	33776
4800	7.95201	2996	6.88333	4335	34.94360	28187	41.82694	32522
5000	7.98198	.....	6.92669	.....	35.22548	.....	42.15217	.....

TABLE 3. *Ideal gas thermodynamic functions for* DCN

°K	$\frac{C_p^\circ}{R}$		$\frac{(H^\circ-E_0^\circ)}{RT}$		$\frac{-(F^\circ-E_0^\circ)}{RT}$		$\frac{S^\circ}{R}$	
50	3.50025	43	3.48845	199	14.48342	63620	17.97188	63820
60	3.50069	187	3.49044	157	15.11963	53817	18.61008	53974
70	3.50256	528	3.49202	160	15.65781	46639	19.14983	46799
80	3.50785	1107	3.49362	213	16.12420	41160	19.61782	41373
90	3.51893	1883	3.49575	318	16.53581	36846	20.03156	37165
100	3.53776	2771	3.49894	471	16.90428	33339	20.40322	33841
110	3.56548	3673	3.50376	662	17.23797	30512	20.74173	31174
120	3.60221	4506	3.51028	875	17.54310	28130	21.05338	29005
130	3.64727	5217	3.51903	1098	17.82440	26117	21.34344	27216
140	3.69944	5779	3.53002	1319	18.08558	24398	21.61560	25717
150	3.75723	6188	3.54321	1529	18.32956	22915	21.87278	24444
160	3.81911	6453	3.55851	1721	18.55871	21624	22.11722	23345
170	3.88365	6591	3.57572	1893	18.77496	20491	22.35068	22384
180	3.94956	6624	3.59466	2042	18.97987	19489	22.57453	21531
190	4.01581	6572	3.61508	2168	19.17476	18597	22.78985	20765
200	4.08153	6455	3.63676	2272	19.36074	17798	22.99751	20070
210	4.14609	6291	3.65949	2355	19.53872	17078	23.19821	19433
220	4.20901	6094	3.68304	2420	19.70950	16425	23.39255	18845
230	4.26995	5876	3.70724	2467	19.87375	15829	23.58100	18297
240	4.32871	5646	3.73192	2500	20.03205	15285	23.76398	17785
250	4.38518	5413	3.75693	2521	20.18490	14784	23.94184	17305
260	4.43932	5183	3.78214	2530	20.33274	14321	24.11489	16852
270	4.49115	4958	3.80745	2531	20.47596	13892	24.28341	16423
280	4.54074	4743	3.83276	2523	20.61488	13493	24.44765	16017
290	4.58817	4539	3.85800	2510	20.74982	13121	24.60782	15631
300	4.63357	4348	3.88310	2491	20.88104	12773	24.76414	15264
310	4.67706	4171	3.90801	2468	21.00877	12446	24.91679	14915
320	4.71877	4006	3.93270	2443	21.13324	12139	25.06594	14582
330	4.75884	3856	3.95713	2415	21.25463	11849	25.21176	14264
340	4.79740	3718	3.98128	2385	21.37312	11575	25.35441	13960
350	4.83459	3593	4.00513	2354	21.48887	11315	25.49401	13670
360	4.87052	3479	4.02868	2322	21.60203	11069	25.63071	13392
370	4.90532	3377	4.05190	2290	21.71273	10836	25.76464	13126
380	4.93909	3284	4.07481	2258	21.82109	10613	25.89590	12872
390	4.97194	3201	4.09739	2226	21.92723	10401	26.02463	12628
400	5.00395	15029	4.11966	10673	22.03125	49146	26.15091	59820
450	5.15425	13906	4.22639	9981	22.52271	45051	26.74911	55032
500	5.29331	13197	4.32620	9396	22.97323	41678	27.29944	51074
550	5.42728	12669	4.42017	8907	23.39001	38845	27.81018	47752
600	5.55198	12195	4.50924	8493	23.77847	36431	28.28771	44924
650	5.67393	11713	4.59417	8133	24.14278	34346	28.73695	42480
700	5.79107	11204	4.67551	7813	24.48624	32525	29.16176	40339
750	5.90311	10666	4.75364	7520	24.81150	30920	29.56515	38441
800	6.00978	10110	4.82885	7246	25.12071	29493	29.94956	36749
850	6.11089	9546	4.90132	6987	25.41565	28214	30.31697	35201
900	6.20635	8986	4.97119	6739	25.69779	27059	30.66899	33799
950	6.29622	8438	5.03859	6501	25.96838	26010	31.00698	32512
1000	6.38060	7909	5.10360	6271	26.22849	25053	31.33210	31324
1050	6.45969	7405	5.16632	6049	26.47903	24174	31.64535	30223
1100	6.53375	6928	5.22681	5834	26.72077	23363	31.94758	29198
1150	6.60304	6480	5.28515	5627	26.95441	22613	32.23956	28240
1200	6.66784	11734	5.34143	10664	27.18054	43180	32.52197	53845
1300	6.78519	10288	5.44808	9926	27.61234	40742	33.06042	50668
1400	6.88807	9050	5.54734	9246	28.01976	38591	33.56711	47838
1500	6.97858	7997	5.63980	8622	28.40568	36676	34.04549	45299
1600	7.05855	7101	5.72602	8051	28.77245	34958	34.49848	43009
1700	7.12957	6340	5.80654	7529	29.12283	33404	34.92858	40934
1800	7.19288	5692	5.88183	7053	29.45908	31992	35.33792	39045
1900	7.24990	5138	5.95236	6618	29.77601	30701	35.72838	37320
2000	7.30129	4664	6.01855	6221	30.08303	29516	36.10158	35737
2100	7.34793	4256	6.08076	5858	30.37819	28424	36.45896	34282
2200	7.39049	3903	6.13934	5525	30.66244	27413	36.80178	32939
2300	7.42953	3598	6.19460	5221	30.93657	26475	37.13117	31696
2400	7.46551	3332	6.24681	4942	31.20132	25601	37.44814	30544
2500	7.49884	3100	6.29624	4685	31.45734	24786	37.75358	29472
2600	7.52985	2896	6.34309	4449	31.70521	24023	38.04830	28472
2700	7.55882	2717	6.38759	4231	31.94544	23307	38.33303	27539
2800	7.58599	2558	6.42991	4031	32.17851	22634	38.60843	26665
2900	7.61158	2418	6.47022	3845	32.40486	22000	38.87508	25845
3000	7.63576	4473	6.50867	7186	32.62486	42238	39.13354	49425
3200	7.68049	4070	6.58053	6591	33.04725	40094	39.62779	46686
3400	7.72119	3742	6.64645	6076	33.44820	38164	40.09466	44240
3600	7.75862	3473	6.70721	5626	33.82984	36416	40.53706	42042
3800	7.79335	3249	6.76348	5231	34.19401	34826	40.95749	40058
4000	7.82584	3060	6.81579	4883	34.54228	33373	41.35807	38257
4200	7.85645	2900	6.86462	4574	34.87602	32041	41.74064	36615
4400	7.88545	2762	6.91037	4300	35.19643	30813	42.10680	35113
4600	7.91308	2643	6.95337	4054	35.50456	29679	42.45794	33734
4800	7.93951	2538	6.99391	3833	35.80136	28629	42.79528	32462
5000	7.96490	.....	7.03225	.....	36.08765	.....	43.11990	.....

TABLE 4. *Ideal gas thermodynamic functions for* TCN

°K	$\frac{C_p^\circ}{R}$		$\frac{(H^\circ-E_0^\circ)}{RT}$		$\frac{(-F^\circ-E_0^\circ)}{RT}$		$\frac{S^\circ}{R}$	
50	3.50031	89	3.49015	174	14.69139	63649	18.18154	63824
60	3.50120	345	3.49189	153	15.32789	53839	18.81979	53992
70	3.50466	878	3.49343	188	15.86628	46659	19.35971	46848
80	3.51344	1686	3.49531	286	16.33288	41184	19.82819	41470
90	3.53031	2676	3.49818	446	16.74472	36878	20.24290	37325
100	3.55708	3720	3.50264	656	17.11351	33412	20.61615	34068
110	3.59428	4700	3.50920	898	17.44763	30570	20.95684	31469
120	3.64129	5538	3.51819	1155	17.75334	28204	21.27153	28359
130	3.69667	6195	3.52974	1410	18.03539	26208	21.56513	27618
140	3.75862	6662	3.54384	1651	18.29747	24505	21.84132	26156
150	3.82525	6954	3.56036	1871	18.54252	23036	22.10288	24908
160	3.89479	7083	3.57908	2055	18.77289	21759	22.35197	23824
170	3.96572	7107	3.59973	2230	18.99048	20637	22.59022	22868
180	4.03680	7024	3.62204	2368	19.19686	19646	22.81890	22014
190	4.10704	6870	3.64572	2479	19.39332	18762	23.03905	21241
200	4.17574	6665	3.67051	2565	19.58035	17970	23.25147	20535
210	4.24240	6429	3.69617	2629	19.76065	17255	23.45683	19885
220	4.30670	6174	3.72247	2675	19.93320	16605	23.65568	19281
230	4.36844	5913	3.74922	2704	20.09926	16013	23.84849	18717
240	4.42758	5653	3.77626	2719	20.25940	15470	24.03567	18189
250	4.48411	5399	3.80346	2722	20.41411	14970	24.21757	17693
260	4.53811	5158	3.83068	2716	20.56381	14508	24.39450	17224
270	4.58969	4929	3.85785	2702	20.70889	14079	24.56674	16781
280	4.63899	4717	3.88487	2682	20.84968	13679	24.73456	16361
290	4.68617	4520	3.91169	2657	20.98648	13306	24.89817	15963
300	4.73138	4340	3.93827	2628	21.11954	12956	25.05781	15585
310	4.77478	4176	3.96456	2597	21.24910	12628	25.21366	15225
320	4.81655	4027	3.99053	2564	21.37538	12318	25.36592	14883
330	4.85682	3892	4.01618	2530	21.49857	12027	25.51475	14557
340	4.89574	3771	4.04148	2494	21.61884	11751	25.66033	14246
350	4.93346	3662	4.06643	2459	21.73636	11490	25.80279	13949
360	4.97008	3564	4.09102	2424	21.85126	11242	25.94229	13666
370	5.00572	3476	4.11526	2389	21.96368	11006	26.07895	13395
380	5.04049	3397	4.13916	2354	22.07375	10782	26.21291	13137
390	5.07447	3327	4.16270	2321	22.18157	10568	26.34428	12889
400	5.10774	15795	4.18592	11131	22.28725	49953	26.47317	61084
450	5.26569	14778	4.29723	10430	22.78678	45821	27.08402	56251
500	5.41348	14037	4.40154	9842	23.24500	42417	27.64654	52259
550	5.55385	13388	4.49996	9344	23.66917	39558	28.16914	48903
600	5.68774	12749	4.59341	8912	24.05476	37121	28.65817	46034
650	5.81523	12091	4.68253	8526	24.43597	35015	29.11851	43542
700	5.93615	11414	4.76780	8173	24.78613	33175	29.55393	41348
750	6.05030	10728	4.84953	7843	25.11788	31550	29.96742	39393
800	6.15758	10046	4.92797	7531	25.43339	30103	30.36136	37635
850	6.25805	9380	5.00329	7234	25.73442	28804	30.73771	36038
900	6.35185	8740	5.07563	6949	26.02246	27630	31.09810	34579
950	6.43926	8132	5.14513	6676	26.29876	26562	31.44389	33238
1000	6.52059	7560	5.21189	6414	26.56438	25585	31.77628	31999
1050	6.59620	7026	5.27601	6162	26.82023	24687	32.09627	30849
1100	6.66647	6531	5.33766	5921	27.06711	23858	32.40477	29779
1150	6.73178	6074	5.39687	5690	27.30569	23089	32.70256	28780
1200	6.79253	10920	5.45377	10728	27.53659	44082	32.99037	54810
1300	6.90173	9500	5.56105	9923	27.97742	41579	33.53847	51503
1400	6.99673	8309	5.66028	9192	28.39322	39369	34.05350	48562
1500	7.07982	7312	5.75221	8530	28.78691	37399	34.53913	45930
1600	7.15295	6476	5.83752	7932	29.16091	35630	34.99843	43562
1700	7.21772	5774	5.91684	7390	29.51721	34031	35.43406	41421
1800	7.27546	5181	5.99075	6900	29.85753	32577	35.84828	39477
1900	7.32728	4679	6.05975	6456	30.18330	31248	36.24306	37705
2000	7.37407	4251	6.12431	6054	30.49579	30028	36.62011	36082
2100	7.41659	3886	6.18485	5688	30.79607	28904	36.98093	34593
2200	7.45545	3572	6.24174	5355	31.08512	27865	37.32686	33220
2300	7.49118	3301	6.29530	5052	31.36377	26900	37.65907	31952
2400	7.52419	3066	6.34582	4775	31.63277	26002	37.97860	30778
2500	7.55485	2861	6.39358	4522	31.89280	25164	38.28638	29687
2600	7.58347	2682	6.43880	4289	32.14445	24381	38.58325	28671
2700	7.61030	2525	6.48169	4076	32.38826	23646	38.86996	27722
2800	7.63555	2386	6.52246	3879	32.62473	22956	39.14719	26836
2900	7.65941	2263	6.56125	3698	32.85430	22306	39.41556	26005
3000	7.68205	4209	6.59824	6907	33.07736	42807	39.67561	49715
3200	7.72414	3858	6.66731	6331	33.50544	40613	40.17276	46944
3400	7.76273	3572	6.73063	5834	33.91157	38938	40.64221	44472
3600	7.79845	3338	6.78897	5401	34.29796	36852	41.08694	42254
3800	7.83183	3142	6.84299	5023	34.66648	35229	41.50948	40252
4000	7.86326	2978	6.89323	4690	35.01878	33746	41.91201	38437
4200	7.89304	2837	6.94013	4396	35.35625	32388	42.29639	36784
4400	7.92142	2717	6.98410	4134	35.68013	31137	42.66423	35272
4600	7.94859	2612	7.02545	3901	35.99151	29983	43.01696	33884
4800	7.97471	2520	7.06446	3691	36.29134	28914	43.35580	32605
5000	7.99991	.....	7.10138	.....	36.58048	.....	43.68186	.....

378088—56——3

4. References

[1] H. C. Allen (private communication).
[2] A. E. Douglas and D. Sharma, J. Chem. Phys. **21,** 448 (1953).
[3] A. S. Friedman and L. Haar, J. Chem. Phys. **22,** 2051 (1954).
[4] L. Harr and A. S. Friedman, J. Chem. Phys. **23,** 869 (1955).
[5] L. Haar, J. C. Bradley, and A. S. Friedman, J. Research NBS **55,** 285 (1955) RP2631.
[6] R. E. Pennington and K. A. Kobe, J. Chem. Phys. **22,** 1442 (1954).
[7] E. Wichers, J. Am. Chem. Soc. **74,** 2447 (1952).
[8] J. Mattauch and S. Fluegge, Nuclear physics tables and an introduction to nuclear physics (Interscience Publishers, Inc., New York, N. Y., 1946).
[9] Stamm, Halverson, and Whalen, J. Chem. Phys. **17,** 104 (1949).

WASHINGTON, December 12, 1955.

Journal of Research of the National Bureau of Standards Vol. 56, No. 4, April 1956 Research Paper 2669

Surge Voltage Breakdown of Air in a Nonuniform Field

J. H. Park and H. N. Cones

The discharge and breakdown phenomena in air when a surge voltage is applied to sphere-plane electrodes were investigated. A steeply rising surge of 145 kilovolts peak value was applied to the plane placed 86 centimeters above the laboratory floor. A 1.6-centimeter diameter sphere, mounted an adjustable distance below the plane, was connected to ground through the surge impedance of a coaxial cable. Experimental data consisted of oscillograms of the current to the sphere and pictures of the discharge between the electrodes. A method for chopping the applied voltage surge at an accurately controllable time was used to study the discharge at gap spacings for which a full-wave applied surge would cause breakdown.

Complete breakdown did not occur for gap spacings greater than 28 centimeters, sphere positive, or 20 centimeters, sphere negative. But at gap spacings up to 56 centimeters, sphere positive, and 46 centimeters, sphere negative, discharge streamers (corona) did develop from the sphere and they were accompanied by short pulses of current to the sphere. At gap spacings near those giving breakdown, these initial streamers span the gap without yielding breakdown. Measured speeds of formation of these initial streamers were found to be 500 centimeters per microsecond for the sphere negative and 800 centimeters per microsecond for the sphere positive.

For shorter gap spacings the discharge leading to breadown is illustrated by the data obtained with the applied voltage chopped. Bright conducting channels develop between the sphere and plane. At the same time the current to the sphere starts to rise again fairly slowly at first and then at an increasing rate up to breakdown. The mechanism leading to breakdown is not the same for the sphere negative as for the sphere positive, and it is different for very short gaps which correspond to high overvoltage. An attempt is made to explain how the initial streamers form and how the channels leading to breakdown develop.

1. Introduction

Electrical breakdown in air has been extensively studied by a large number of investigators and the many papers and books already published on this subject have contributed greatly toward an understanding of the mechanism of breakdown. The parameters most likely to affect breakdown mechanism are (1) gas pressure, (2) size, shape, and separation of electrodes, and (3) waveform of the applied voltage. No single simple theory can be expected to explain breakdown of a gas under all possible experimental conditions. The original Townsend theory with some modifications [1,2] [1] is well established as giving the breakdown mechanism of gases at pressures much below atmospheric, and in some recent theoretical analyses [3,4] the Townsend theory is extended to include breakdown at amospheric pressures. However, the streamer theory of Loeb and Meek [5] or some modification of it appears most likely to account for the short formative time lags experienced in uniform field breakdown at atmospheric pressure. Breakdown studies at high frequencies appear to require an entirely different theory to adequately explain the results, and a theory that seems adequate has been proposed [6,7,8].

The theories referred to above are based mainly on uniform field breakdown, largely because this has seemed the simpler case. For the same reason, most of the experimental data already published have been for gaps giving a uniform or nearly uniform field. At the higher voltages almost all of these data have been obtained with sphere gaps because such gaps are used as primary reference standards in the field of high voltage measurements. For the design of high voltage electrical equipment and in the development of methods for measuring steeply rising voltage surges, a knowledge of just how breakdown occurs when a voltage is suddenly applied to electrodes producing a nonuniform field is of primary importance. Results obtained by Norinder and others [9,10,11,12,13] indicate that the mechanism of breakdown for nonuniform field gaps is quite different from that for uniform field gaps. The work described in this paper was undertaken in order to gain a better understanding of the mechanism of breakdown for nonuniform fields.

2. Scope of the Experimental Work

The present work is limited to discharge phenomena and breakdown in air, under the usual laboratory conditions of pressure and humidity, when voltage is suddenly applied and the electrode geometry is such that a nonuniform electric field is produced in the gap. The laboratory floor which has a grounded metal grid imbedded in its surface was used as a semi-infinite ground plane. The upper or high-voltage electrode consisted of a large circular plane, 84 cm (33 in.) in diameter, made of an aluminum alloy, placed 86.4 cm (34 in.) above and parallel to the ground plane. The ground electrode was a 1.6-cm (⅝-in.) diameter sphere mounted at the end of a conductor centered inside a 0.635-cm (¼-in.)

[1] Figures in brackets indicate the literature references at the end of this paper

diameter metal tube and insulated from it. The sphere was located at an adjustable distance L beneath the center of the high-voltage plane electrode as indicated schematically in figure 1. A metal-covered trench in the floor permitted the sphere mounting tube to extend into the trench through a hole in the cover. The tube was grounded at the metal trench cover, and in the trench below its cover, the tube and its center conductor were connected to a coaxial cable. This cable ran in the trench to a cathode ray oscillograph (CRO) where it was terminated by its characteristic impedance of 50 ohms. Thus the sphere was "in effect" connected directly to ground through a 50-ohm resistance and any current from the sphere to the high-voltage plane electrode could be measured by the IR drop it produced at the oscillograph. In addition to permitting an accurate measurement of prebreakdown current between the sphere and the plane when voltage is suddenly applied to the plane, this electrode arrangement [2] also makes it possible to compute the initial electric field at various distances from the sphere toward the plane (see the appendix for a summary of such computations). The voltage gradient is of course maximum at the surface of the sphere, allowing significant polarity effects to be studied.

The main purpose of the present investigation was to obtain data indicating the mechanism of breakdown. A study of discharge phenomena could be approached in two ways: (1) by holding the peak voltage of the applied surge constant and changing the gap spacing or (2) by holding the gap spacing constant and changing the peak voltage. Since it is experimentally quite troublesome to maintain the same rise time for various values of peak voltage, method (1) above was used. Voltage surges of fairly short duration and of the following wave shapes were applied to the gap: (1) a surge that rose to a peak value of 145 kv in about 0.07 μsec (as rapidly as possible with the setup used) and maintained this peak value fairly constant, gradually decreasing to half value in about 100 μsec (designated as 0.07×100, 145-kv surge); (2) a surge similar to (1) except that it rose to peak value in about 1 μsec (designated as 1×100, 145-kv surge); (3) surges similar to either (1) or (2) except that the voltage was chopped off at various times after reaching peak value (designated as $0.07\times t_c$, 145-kv or $1\times t_c$, 145-kv surge).

The sphere-plane electrode system was enclosed in a light-tight fiberboard box 3½ by 3 by 10 ft (106×91×305 cm). A 35-mm camera with an f/1.9 coated lens was placed inside this enclosure at a distance of 30 in. (76 cm) from the gap for taking photographic records of the discharge between electrodes. This box also provided shielding for the test gap against any extraneous radiation. The effect of an increased ion and electron density at the gap before applying voltage was determined by placing a radioactive source near the sphere electrode.

[2] The idea of putting high voltage on the plane electrode and grounding the smaller electrode through a resistance so that current could be measured was also used by Saxe and Meek [13] in their recent work on this subject. The present paper was completed but not published at the time the Saxe and Meek paper was published.

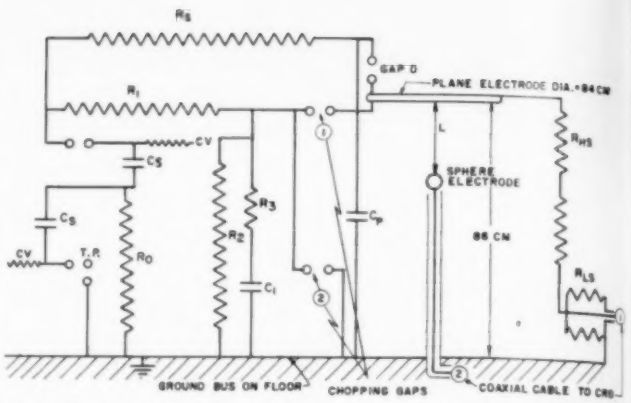

FIGURE 1. *Schematic diagram of sphere-plane electrodes showing the voltage supply and measuring circuits*

At the two points marked "CV," one positive and the other negative, 100-kv charging voltages were introduced. C_s=½ μf, 100-kv capacitor. R_0=3,000 ohms. R_1=2,500 ohms. R_s=165 ohms. C_p=0.003 μf capacitor. R_3=500 ohms. R_2=40,000 ohms. C_1=0.002 μf capacitor. R_{HS} and R_{LS} form voltage divider.

3. Experimental Setup and Procedure

The arrangement of the sphere-plane electrodes is shown schematically in figure 1. The divider for measuring the voltage applied to the plane is also shown. The high voltage part of this divider consists of a 1,000-ohm noninductive wire wound resistor, R_{HS}, placed vertically to the floor at about 2 ft from the edge of the plane electrode. The divider low side, R_{LS}, is a specially constructed 5-ohm noninductive resistor, arranged to produce minimum inductive effects from ground currents when it is connected to the coaxial cable to the CRO. A high-voltage cold-cathode oscillograph with beam intensification [14] was used to record the voltage waveform and to measure peak values. By connecting the CRO cable at (2) in figure 1 the same oscillograph was used to obtain a record of prebreakdown current. This arrangement of electrodes and measuring circuits was used throughout our experiments.

The circuit used for producing the surge voltage and for applying it to the plane-sphere gap is shown in figure 1 at the left. Capacitors, C_s, are 2 units from a 20-unit 2,000-kv surge voltage generator. They are each charged to 100 kv by the full-wave kenotron rectifier of the surge voltage generator, one positive and the other negative with respect to ground. By applying a tripping pulse to the middle ball of the three-ball gap, the two capacitors, C_s, are connected in series to the discharge circuit. To obtain a full-wave voltage surge at the test gap, chopping gap (1) is set wide and (2) is shorted. Thus the two capacitors, C_s in series, start discharging through R_1 in parallel with R_s and C_p in series. If gap D is shorted, the slowly rising voltage surge (1×100, 145-kv surge) is applied to the plane-sphere gap. To obtain the fast-rising surge (0.07×100, 145-kv surge), gap D is set at 5-cm spacing. This keeps the voltage off the plane-sphere gap during its slowly rising portion. The oscillograph records reproduced in figures 2 and 3 show the waveform of the steeply and slowly rising voltage surges, respectively. Details of the wave front are shown by the records obtained using a fast sweep.

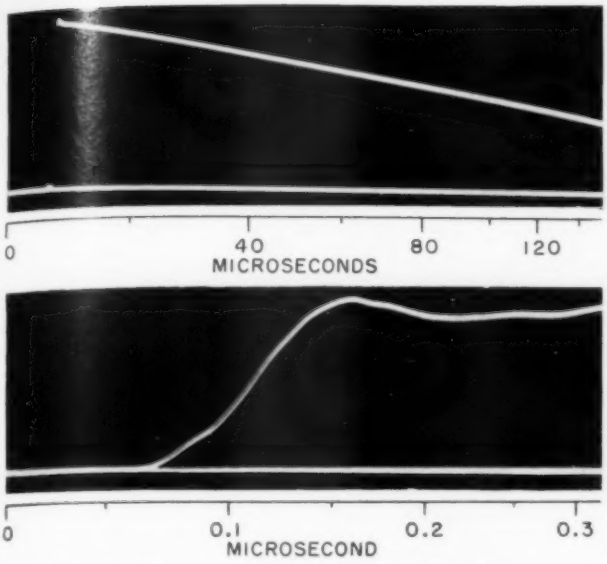

FIGURE 2. *Oscillograms of 0.07×100, 145-kv voltage surge.*
A, Slow sweep showing wave tail; B, fast sweep showing wave front.

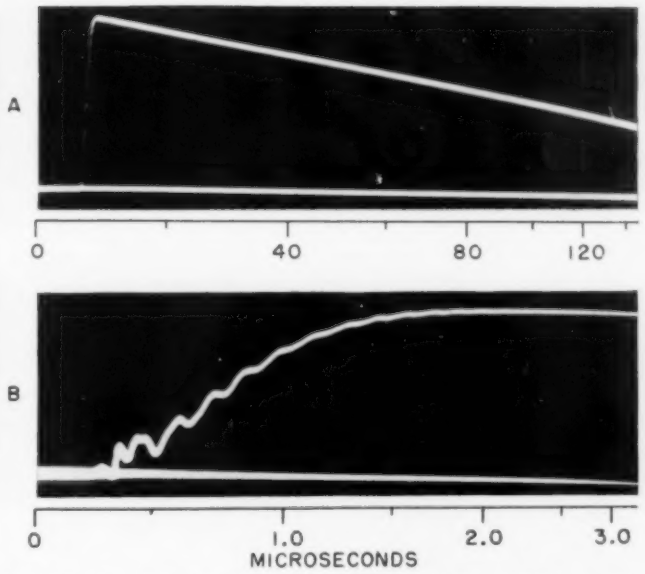

FIGURE 3. *Oscillograms of 1×100, 145-kv voltage surge.*
A, Slow sweep showing wave tail. B, Fast sweep showing wave front.

The chopping gaps (1) and (2) together with R_1, R_2, R_3, and C_1 are used to chop the voltage applied to the plane electrode at a definite time after it is applied. This chopping circuit is similar to one described by G. H. Johnson [15]. As noted from the values of circuit constants given in figure 1, the time constant $R_s C_p$ is about 0.5 μsec and the time constant $(R_1+R_2)C_1$ is about 5 μsec. Thus gap D fires very soon after the supply circuit is triggered and this puts voltage on the plane electrode. At the same time the voltage across chopping gap (2) begins to rise, and by adjusting gap (2) it can be set to fire from 1 to 6 μsec after voltage is applied to the plane electrode. Before chopping gap (2) fires, the two balls of chopping gap (1) have voltages of the same polarity applied to them; thus gap (1) will not fire. But when gap (2) fires, the full voltage applied to the plane will appear across gap (1) and it will fire, thus chopping the supply voltage.

The procedure consisted, in general, of choosing a particular wave shape and polarity and then obtaining (1) CRO records of the sphere current and (2) photographs of the discharge between sphere and plane, for various values of gap spacing L. At values of L for which the full voltage wave would cause complete breakdown between the sphere and plane, a series of pictures and CRO records of current were also taken with the applied voltages chopped at various times before complete breakdown.

Records of light output from the prebreakdown discharge were also obtained in some cases by using a photomultiplier tube and a high-speed oscilloscope with amplifier. The variations in light output followed the same pattern as the records of current to the sphere, but because this scheme is much more subject to extraneous pickup and calibration errors, the current records are considered to be more significant.

4. Experimental Results

4.1. Full-Wave 145-kv Surge

Sets of data were obtained under four different conditions of applied voltage: (1) steeply rising surge (.07×100), sphere positive, (2) slowly rising surge (1×100), sphere positive, (3) steeply rising surge, sphere negative, and (4) slowly rising surge, sphere negative. For each condition of applied voltage, the test data included CRO records of the current to the sphere and corresponding photographs of the discharge, at various values of gap spacing L.

Typical results are shown in figures 4, 5, 6, and 7. The first small wiggles on the current records are caused by capacitance current to the sphere when voltage is suddenly applied. They are useful as reference points to show the exact time at which voltage is applied. Following the capacitance current wiggles there is a sudden rise in current followed by an approximately exponential decrease to zero. This will be called the "first discharge pip" because it occurs only on shots causing a visible discharge from the sphere. It does not constitute a complete breakdown of the gap. The first discharge pip is definitely not associated with capacitance pickup because on some shots it occurs when the rate of change of applied voltage is nearly zero as shown, for example, in figure 5A.

For gap spacings less than 28 cm (sphere positive) or 15 cm (sphere negative), complete breakdown between sphere and plane takes place on at least some of the shots. Complete breakdown is indicated on the current record (see figures 4F, 5E, 6F, and 7C) by a second and roughly exponential increase in current to large values. This current rise follows the first discharge pip and will be referred to as the

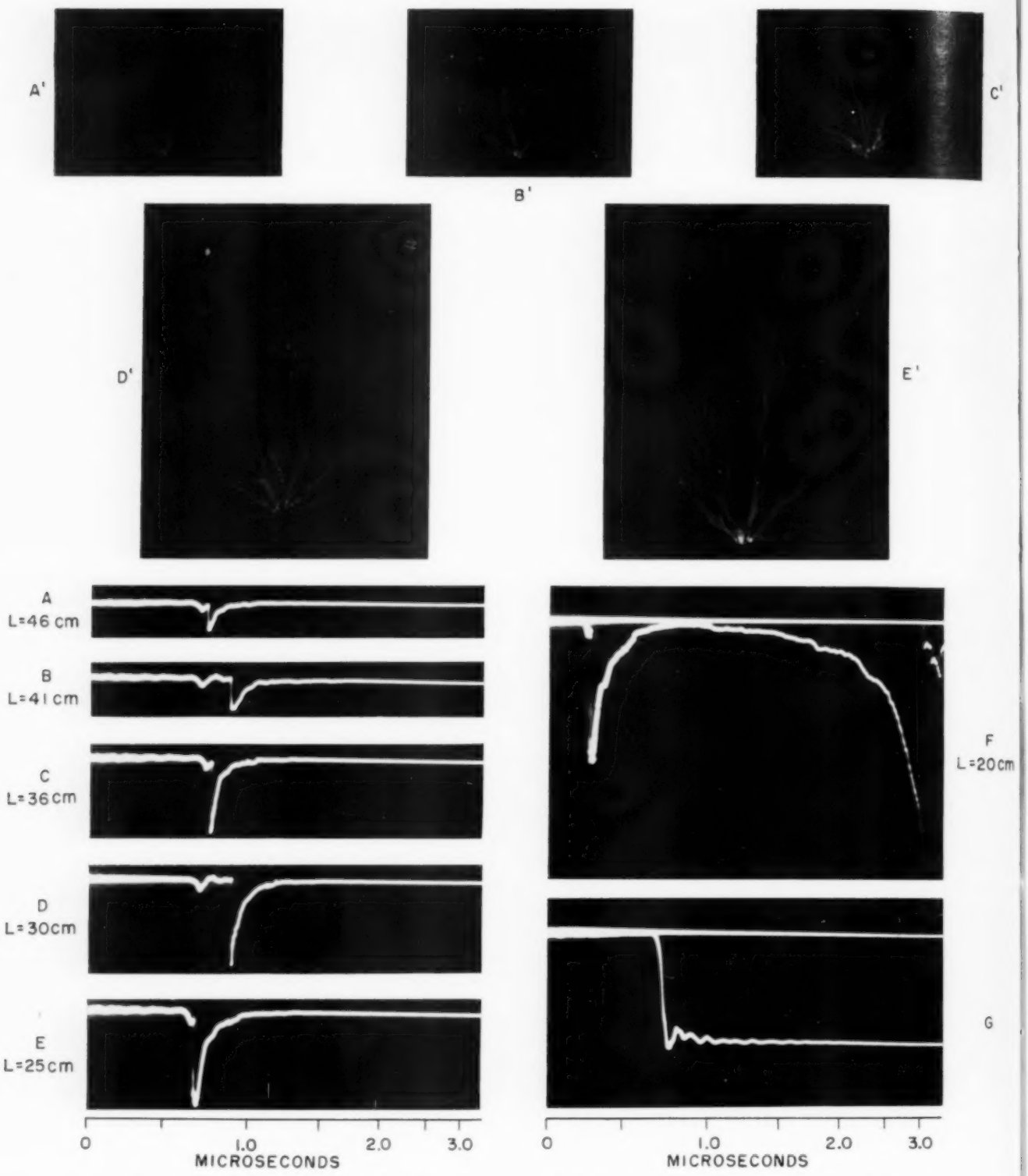

FIGURE 4. *Oscillograms of prebreakdown current and discharge pictures taken on the same shots.*

Sphere positive, 0.07×100, 145-kv surge. Gap spacings L as noted. F is current oscillogram for complete breakdown of gap. G is oscillogram of applied voltage.

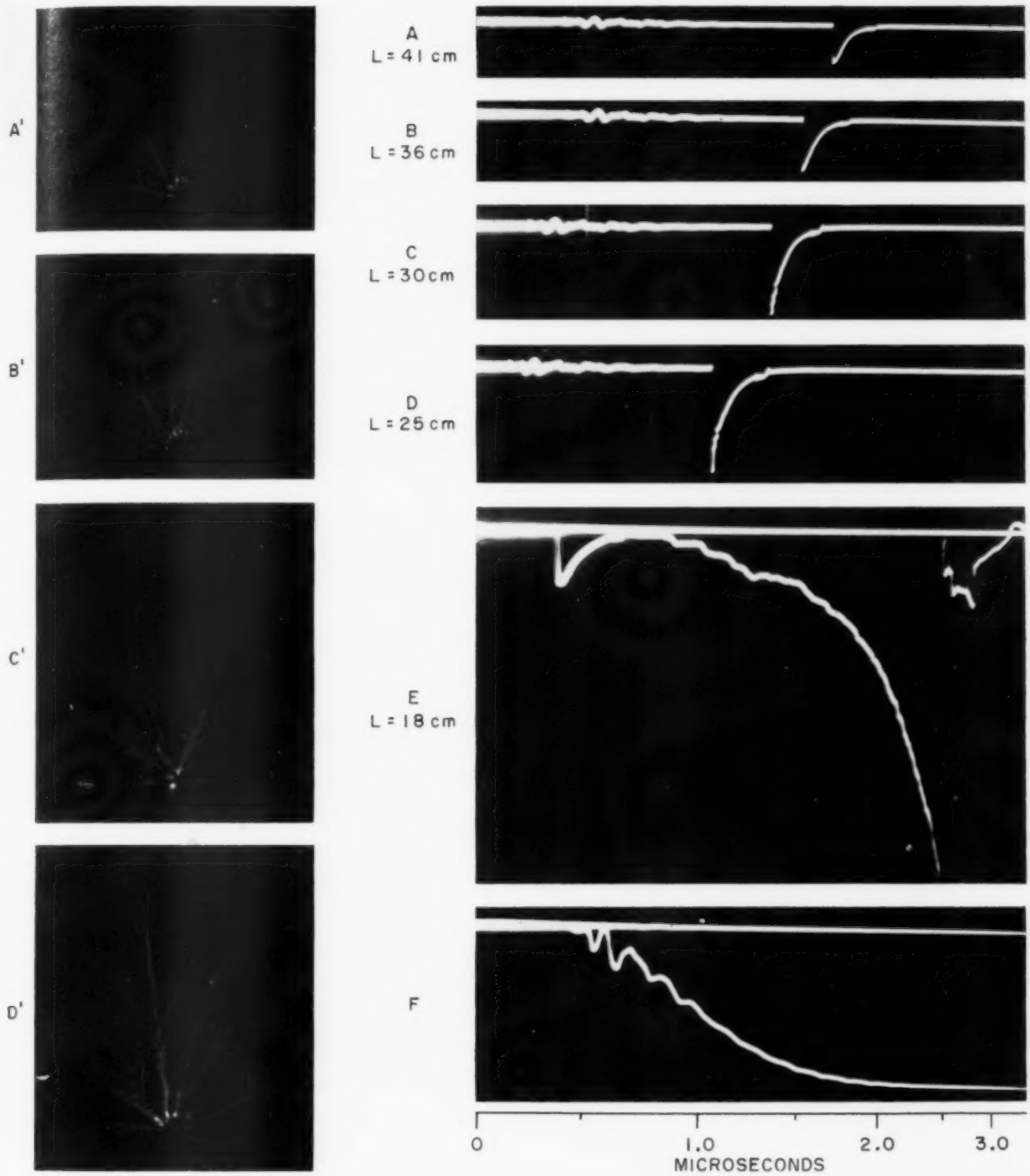

FIGURE 5. *Oscillograms of prebreakdown current and discharge pictures taken on the same shots.*

Sphere positive, 1×100, 145-kv surge. Gap spacings L as noted. E is current oscillogram for complete breakdown of gap. F is oscillogram of applied voltage.

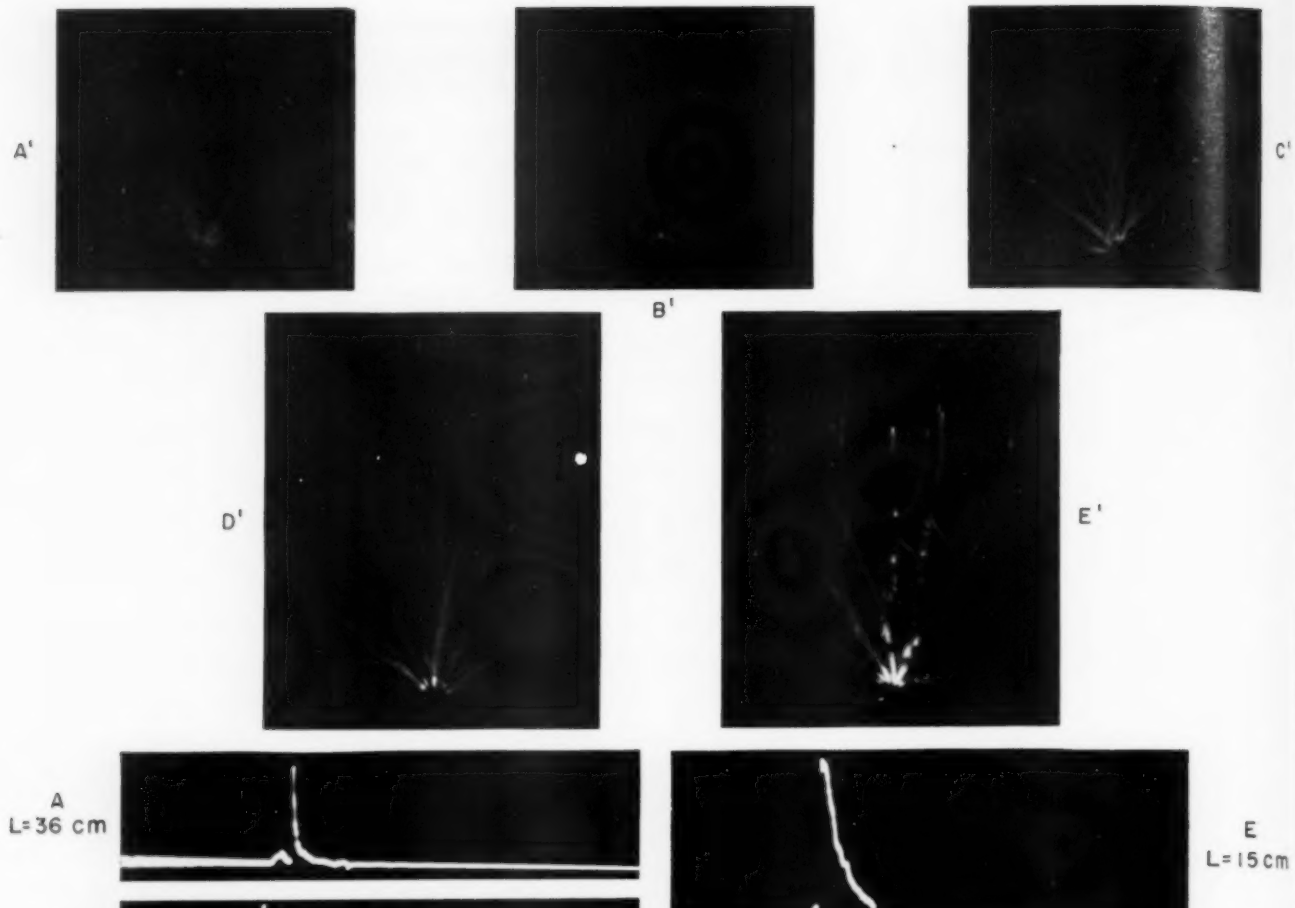

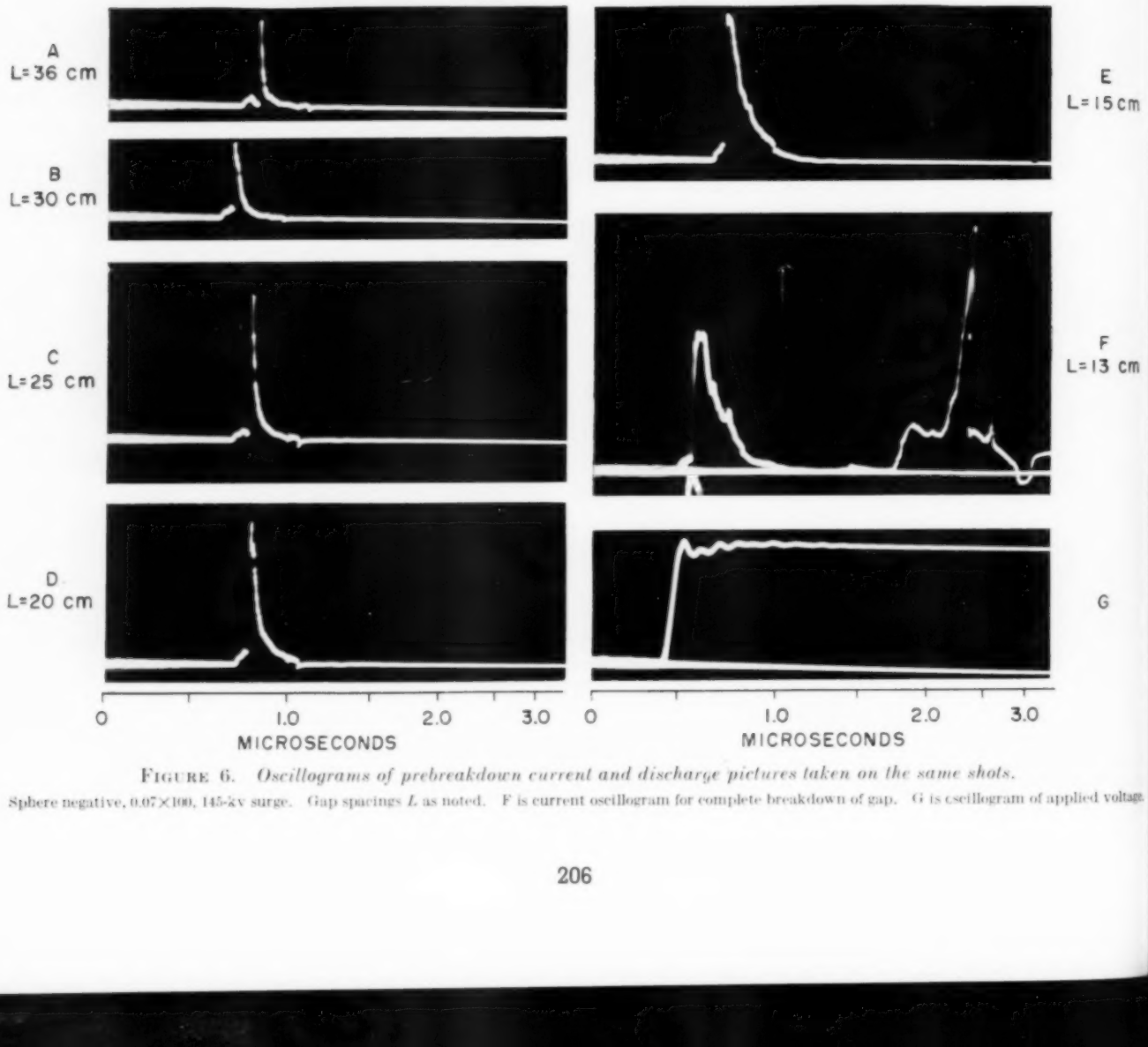

FIGURE 6. *Oscillograms of prebreakdown current and discharge pictures taken on the same shots.*

Sphere negative, 0.07×100, 145-kv surge. Gap spacings L as noted. F is current oscillogram for complete breakdown of gap. G is oscillogram of applied voltage.

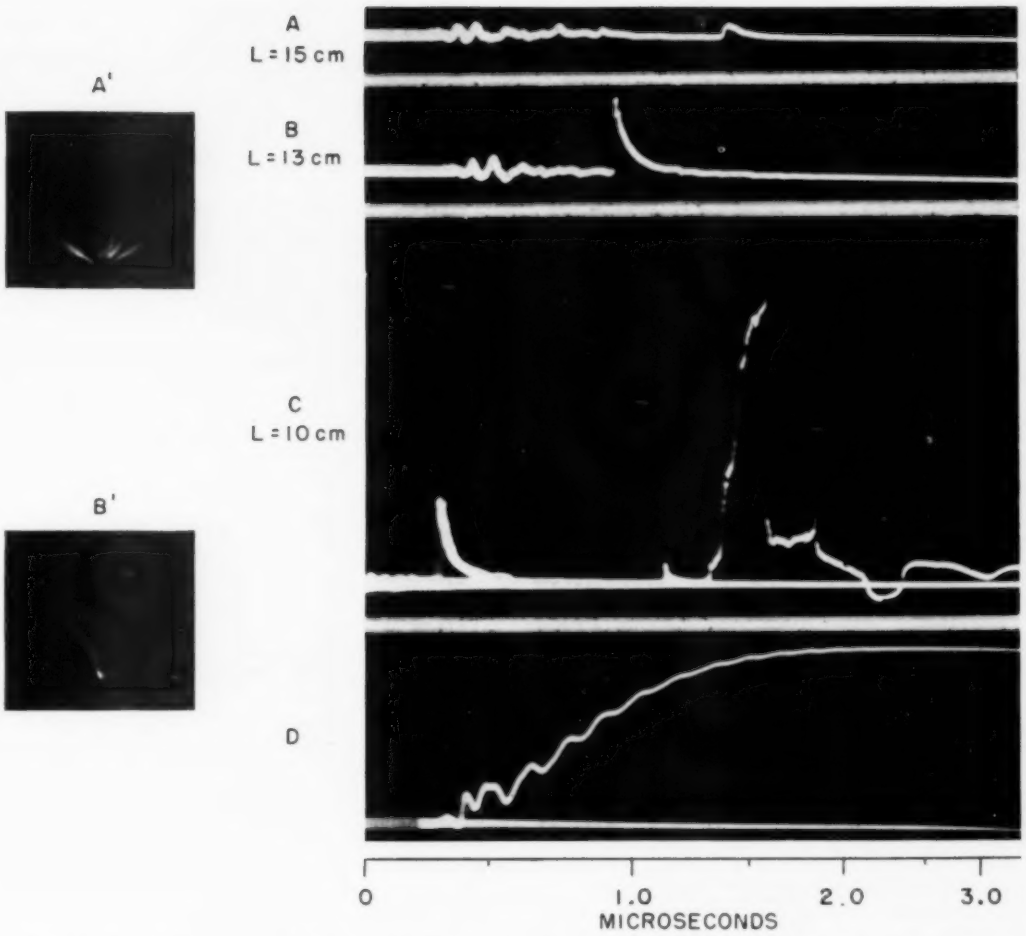

FIGURE 7. *Oscillograms of prebreakdown current and discharge pictures taken on the same shots.*

Sphere negative, 1×100, 145-kv surge. Gap spacings L as noted. C is current oscillogram for complete breakdown of gap. D is oscillogram of applied voltage.

"second discharge rise." When the second discharge rise reaches a value of about 40 amp, a safety gap between the sphere and its grounded mounting tube flashes over, thus cutting off the voltage applied to the CRO cable. The corresponding discharge photographs are not included because they show only a large dense streak on the film. Every time the second discharge rise starts, complete breakdown follows unless the voltage wave is chopped. Thus the discharge photographs shown in figures 4, 5, 6, and 7 are all associated with the first discharge pip only. It should be noted that although the "streamers" shown in these pictures completely bridge[3] the gap for spacings of 25 cm (sphere positive) and 15 cm (sphere negative) they do not constitute complete breakdown, because after the first discharge pip, the current becomes too low to be measured although the voltage remains high for a much longer time.

[3] Complete bridging of the gap was demonstrated by superposing a negative showing the discharge streamers over a negative taken under the same conditions of gap spacing and camera positioning with lights on. Streamers that bridge the gap have a bright spot at their upper tip end as illustrated in figures 4E' and 6E'.

A large amount of data similar to those illustrated in figures 4 to 7 was accumulated to determine the repeatability of results. The following quantities were tabulated: (1) time delay from start of voltage surge to first discharge pip, (2) peak current value of first discharge pip, (3) percentage of flashovers or breakdowns for a given gap spacing, and (4) time delay from first discharge pip to breakdown. All of these quantities were found to vary from shot to shot and/or to some extent from day to day, some more than others. The various factors that might affect repeatability of results will be considered.

Once the circuit constants were properly adjusted, both the steeply and slowly rising voltage surges repeated very well in waveform from shot to shot and day to day. By careful control of charging voltage, peak values were repeated on successive shots (the measured variations being within 2 percent). Air density and humidity could not be controlled but records were kept of pressure, temperature, and humidity. No attempt was made to determine or apply a correction for air density, but

for all data used, the relative air density was within 2 percent of that for standard laboratory conditions of 760 mm of Hg pressure and 25° C temperature. The relative humidity varied from 20 to 75 percent during the period data were being accumulated. The nonrepeatability of experimental results could not be correlated with or accounted for by the small variations in peak magnitude of the applied voltage from shot to shot or by the small changes in relative air density from day to day. There was an indication that changes in relative humidity affected some of the measured quantities.

The surface condition of the spherical electrode and the kind of metal of which the sphere was made may have affected repeatability of results. Most of the data were obtained using a 1.6-cm diameter silver sphere, but data were also obtained using zinc, copper, brass, aluminum, and magnesium spheres of the same diameter. Originally all spheres were given a smooth polish and wiped with a dry chamois, but after even one flashover the surface became quite discolored and after a large number of flashovers the smooth surface was somewhat roughened. Experimental results did not appear to be affected by the condition of the surface of the sphere, but some of the measured quantities appeared to vary slightly with the kind of metal used for the sphere.

Another factor that would be expected to affect repeatability of results is the particular distribution of ions and electrons in the air between the electrodes at the instant voltage is applied. This factor should be of special importance when measuring the time delay from application of voltage to first discharge pip. The conditions prevailing during the experimental observations were intended to approximate average laboratory conditions with each shot being unaffected by previous shots. However, as the gap was located inside a light-tight enclosure so that good pictures of the discharge could be taken, precautions were necessary to insure that the ion distribution was representative of that in free air.

This enclosure had sliding doors at each end. It was found that on the first application of voltage after closing these doors, a discharge pip almost always appeared before peak voltage was reached. It was observed that on succeeding applications of voltage with the doors left closed, either no discharge pip occurred or it was delayed. This can be explained if, during the first application of voltage, a large percentage of the ions inside the enclosure are swept out of the air; because, with the doors closed, there is little chance for new ions to leak into the enclosure before the next application of voltage 30 sec later. When the doors were opened between shots or when a weak gamma-ray source of ionization (Co^{60} giving 0.05 millireontgen (mr) per hour at a distance of 1 m) was placed inside the enclosure a discharge pip was always obtained. In order to check the effect of sweeping ions out of the air inside the enclosure, for one series of tests a d-c source of 7,000 v was applied to the upper plane except for the duration of the high-voltage pulse. This sweep voltage effectively prevented a discharge pip with

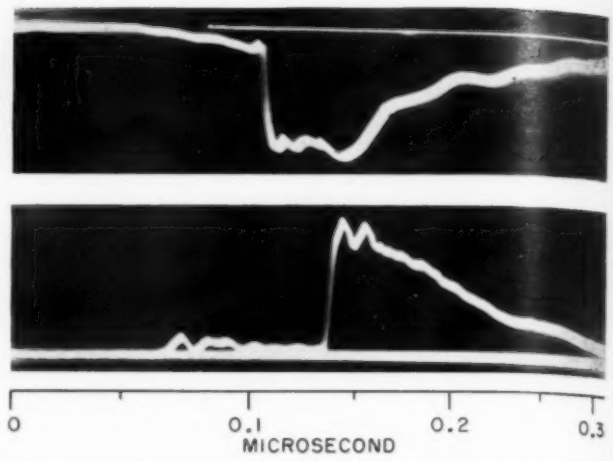

FIGURE 8. *Oscillograms of first discharge current pip on fast sweep.*

A, sphere positive $L = 23$ cm. B, sphere negative $L = 15$ cm.

the doors closed and the weak ionizing source inside the enclosure. With the doors open the sweep voltage did not prevent the discharge pip, apparently because ions could diffuse into the space between the electrodes faster than they were removed. Most of the experimental results were obtained with the weak Co^{60} source inside the enclosure, which it was thought would keep ion density inside about equal to that prevailing in the laboratory provided the 7,000 v was not applied. During some of the experiments stronger ionizing sources were used to study the effect of increasing the ion density in the gap.

A summary of the various quantities that could be tabulated after analyzing the data from over 1,000 shots will now be given. As a start, characteristics associated with the first discharge pip will be described. This discharge appears at gap spacings up to 56 cm (sphere positive) and 46 cm (sphere negative), but at the large spacings there is no discharge pip on some of the shots and the time delay values as measured from the initial application of voltage are quite erratic (up to 20 μsec). At gap spacing less than 46 cm (sphere positive) and 30 cm (sphere negative) a discharge occurs for nearly every shot, and although the time delay is erratic on an occasional shot it is almost always quite small—less than 0.1 μsec for the steeply rising surge and less than 1 μsec for the slowly rising surge.

The wave shape of the first discharge pip is quite repeatable for the sphere positive and somewhat less repeatable for the sphere negative. Typical CRO records of this waveform taken on a fast sweep are shown in figure 8. In general, an average wave shape can be described which holds for both polarities of the sphere and for both steeply and slowly rising surges. It rises to peak value in about 0.008 μsec and decays approximately exponentially to half value in about 0.08 μsec. This pip-wave shape stays essentially the same for all values of gap spacing but its peak value increases as gap spacing is decreased.

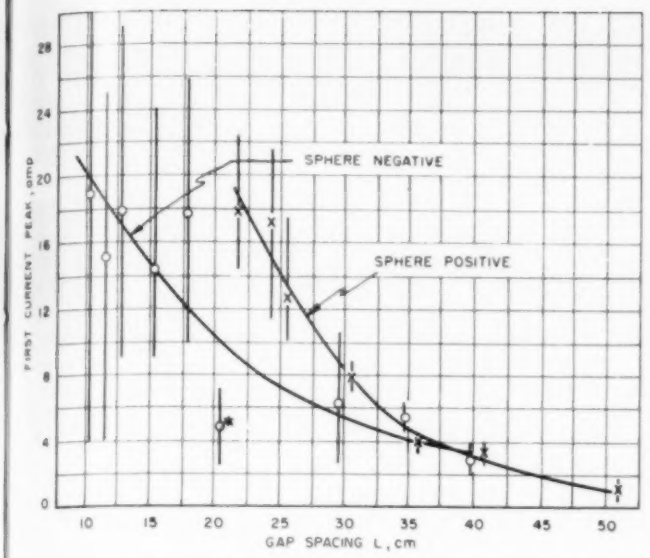

FIGURE 9. *Curves of peak value of first current pip plotted against gap spacing.*

0.07×100, 145-kv surge. Plotted points are each the average of 10 to 100 shots and the vertical lines indicate the spread from minimum to maximum values. *This point is low because on all 10 shots the relative humidity was 75 percent or higher.

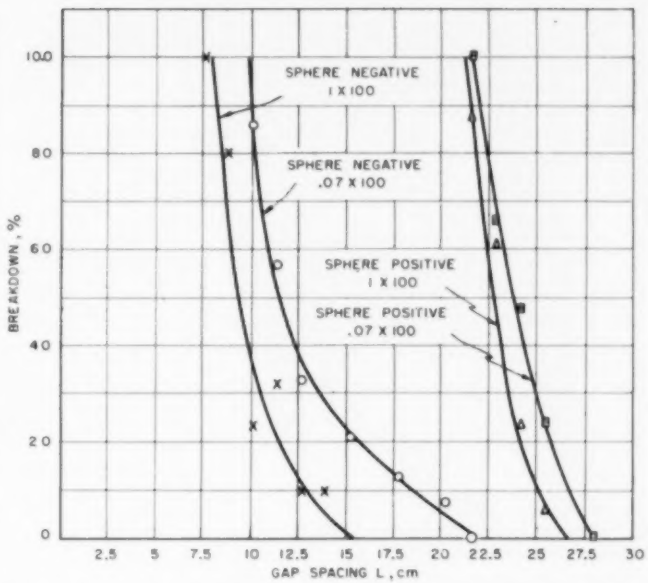

FIGURE 10. *Curves of number of breakdowns expressed as a percentage of the total number of shots at each gap spacing plotted against gap spacing.*

The curves in figure 9 are drawn through points of average value of peak current at various gap spacings for the steeply rising surge. Each plotted point is the average of 10 to 100 shots and the spread from the average is indicated by the vertical line through each point. For the sphere positive the points fall quite nicely on a smooth curve, but the spread in values for each point is fairly large—no effect was detected due to changes in relative humidity or the kind of metal used for the sphere. For the sphere negative the spread in values for each point is extremely large, making it difficult to draw definite conclusions; but with the relative humidity above 70 percent, better repeatability and lower values of average current were obtained. Also it was found that zinc or brass spheres gave somewhat higher currents than silver, copper, or magnesium spheres.

Results using the slowly rising surge are not plotted in figure 9. The actual values varied from 1 to 8 amp and could not be correlated with gap spacing. The lower values obtained with slowly rising surges can be accounted for by the fact that the first discharge pip usually starts on the rising front of the surge, frequently at less than half peak value. An analysis of a large number of records obtained with slowly rising surges indicated that the peak current was approximately proportional to the actual value of voltage at the instant the discharge started. Even for the steeply rising surges it is possible that on some shots the discharge started on the rising front of the voltage, thus partially accounting for the spread in values obtained on successive shots. Examination of a large number of pictures of the discharge, such as those shown in figures 4, 5, 6, and 7, indicates a different pattern of tree-like streamers on each shot but in general the length of these streamers increases in proportion to the peak discharge current. These prebreakdown streamers completely bridge the gap for spacings at which breakdown is likely.

For gap spacings less than 28 cm (sphere positive) or 20 cm (sphere negative), complete breakdown occurs for at least some shots and there is a time delay from the first discharge pip to breakdown as indicated in figures 4F, 5E, 6F, and 7C. A large number of shots at gap spacings giving breakdown were taken using silver, zinc, and copper spheres. The kind of metal used for the sphere and its surface condition may have had an effect ,but because of the statistical nature of the results this effect could not be definitely established and the data on silver, zinc, and copper spheres were all averaged together.

The curves in figure 10 show the number of breakdowns as a percentage of the total number of shots at each gap spacing plotted against gap spacing. Each plotted point represents the results of at least 50 shots. For the sphere positive the increase in gap spacing in going from 100 to 0 percent flashover is 30 percent for the steeply rising surge and 25 percent for the slowly rising surge. For the sphere negative this increase is 120 percent for the steeply rising surge and 90 percent for the slowly rising surge. Also, for sphere positive the gap spacing giving 100 percent flashover is very nearly the same for both the steeply and slowly rising surges, but for sphere negative the gap spacing is 9.6 cm for the steeply rising surge and 8.1 cm for the slowly rising surge. Thus breakdown occurs over a wider range of gap setting for the sphere negative than for the sphere positive and a steeply rising surge increases this range for both polarities.

A plot of time delay from start of first discharge pip to breakdown, against gap spacing is given in

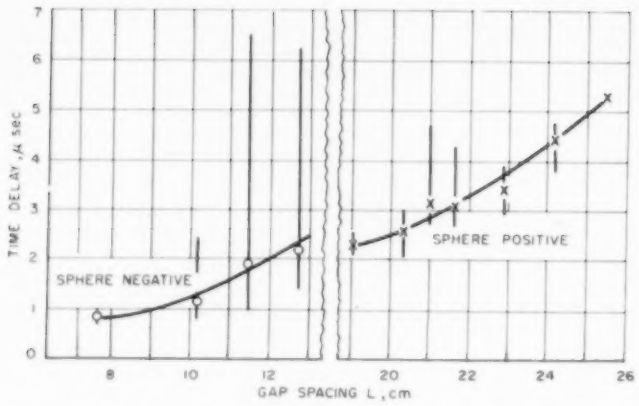

FIGURE 11. *Curves of time delay from start of first current pip to breakdown plotted against gap spacing.*

0.07×100, 145-kv surge. Plotted points are each the average of 10 to 30 shots and the vertical lines indicate the spread from minimum to maximum values.

figure 11 for a steeply rising surge. Each of the plotted points through which the curves are drawn is the average of 10 to 30 shots and the vertical line through each point shows the spread from minimum to maximum time delay at that spacing. The time delay increases on the average with gap spacing but the variation from shot to shot at each gap spacing is quite large, especially with the sphere negative. Time delays for the slowly rising surge are not plotted, but the average values follow about the same curves as plotted in figure 11 and the variations from shot to shot at each gap spacing are about the same.

The statistical nature of the experimental results might be caused by variations in the distribution of free electrons and ions in the gap from shot to shot. As already mentioned, a weak ionizing source was used while obtaining the above data in order to give an average ion density inside the gap enclosure that would correspond to average laboratory conditions outside of such an enclosure. However, the ion distribution still varied from instant to instant and it would be very difficult, if not impossible, to control the instantaneous distribution.

The distribution can be greatly modified by using a strong artificial source of ionization. This was done in two ways: (1) by placing a strong gamma-ray source (Co^{60} giving 50 mr/hr at 1 m) about 46 cm below the sphere with its beam aimed at the sphere, or (2) by placing a weaker source (Co^{60} giving 0.5 mr/hr at 1 m) inside the sphere and near its upper surface.

Data similar to those described above were taken with either one or the other of these gamma-ray sources in place. The following results were noted: (1) the first discharge pip appeared on every shot, even at gap spacings up to 56 cm (sphere positive), and its time delay even at the long gap spacings was always less than 0.2 μsec; (2) the value of peak current of the first discharge pip was much more repeatable from shot to shot, the gain in repeatability being very pronounced for a steeply rising surge and sphere negative; (3) the average value of peak current was less—down to about one-third its value without the strong source for sphere negative at gap spacing 10 cm; (4) the gamma-ray source had little or no effect on the time lag of breakdown versus gap-spacing curves; (5) the only noticeable effect on the percent breakdown versus gap-spacing curves was that for the slowly rising surge and sphere negative no breakdown occurred at gap spacings greater than 11.4 cm.

From these results it is concluded that variations from shot to shot, (1) in the time delay to start of first discharge pip and (2) in the peak value of current of first discharge pip, arise from the random distributions of charges in the gap at the instant voltage is applied. Once the first discharge pip has occurred, however, the subsequent mechanism of breakdown is not affected to any great extent by this initial charge distribution.

4.2. Chopped-Wave 145-kv Surge

Further investigation of the discharge that occurs during the first discharge pip was carried out by chopping the voltage very quickly after the first discharge pip starts. A large number of oscillograms of the current showing the first discharge pip, and corresponding pictures of the discharge, were taken with chopping time from 0.005 to 0.02 μsec after start of first discharge pip. Typical examples of these records are shown in figure 12 for sphere positive and figure 13 for sphere negative. Some branches of the streamers propagate across the gap very quickly (in about 0.01 μsec), and their appearance is very nearly the same as those obtained without chopping the voltage wave but at greater gap spacings. An approximate value for the velocity of propagation of these streamers was obtained by determining the actual length of the streamers from a discharge picture, and taking the time of formation from the corresponding current oscillogram as the time from start of discharge pip to time voltage was chopped. This was done for 10 sets of records for each polarity (similar to those shown in figs. 12 and 13). The mean streamer propagation velocity was found to be 500 cm/μsec for sphere negative and 800 cm/μsec for sphere positive, the average deviations being 90 for sphere negative and 100 for sphere positive.

The experimental results obtained using a full-wave surge voltage indicate that the discharge is initiated by a sudden burst of current, which is quickly reduced to a low value and remains near zero unless complete breakdown is to occur. When and only when breakdown is to occur, the discharge current begins to increase again (the "second discharge rise"), rather slowly at first and then at an ever increasing rate up to breakdown. If breakdown is complete, a picture of the discharge is of little value because the film is greatly overexposed by the intense light from the high current arc. If, however, the voltage wave is chopped off at some time before complete breakdown would have occurred, a photograph of the discharge should be indicative of much of the ionization phenomena taking place up to the time of chopping

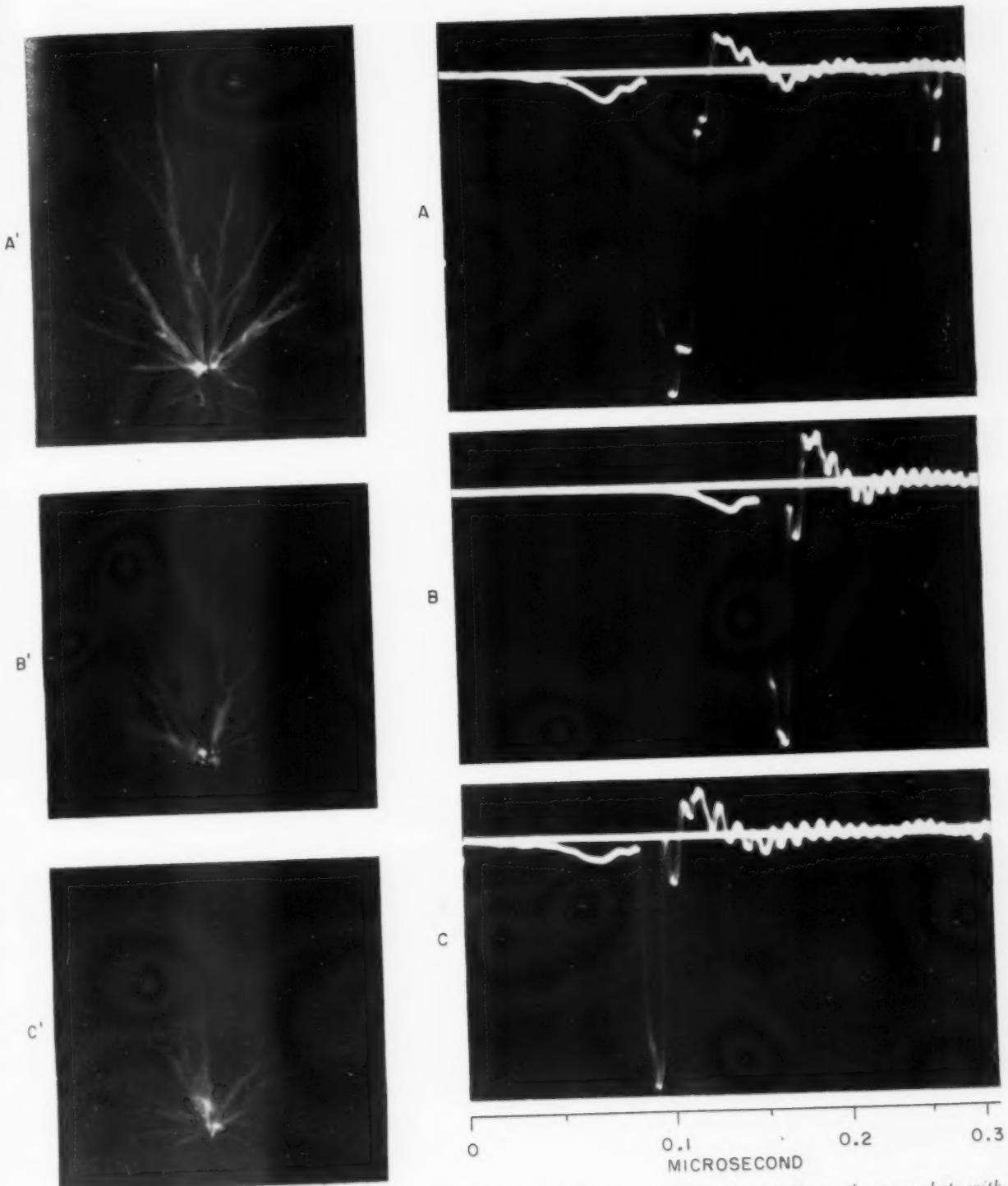

FIGURE 12. *Oscillograms of first current pip (A, B, and C) and discharge pictures (A', B', and C') on the same shots with voltage wave chopped quickly after start of first current pip.*

0.07×*t*. 145-kv surge, sphere positive. Gap spacing = 18 cm for A and B and 20 cm for C.

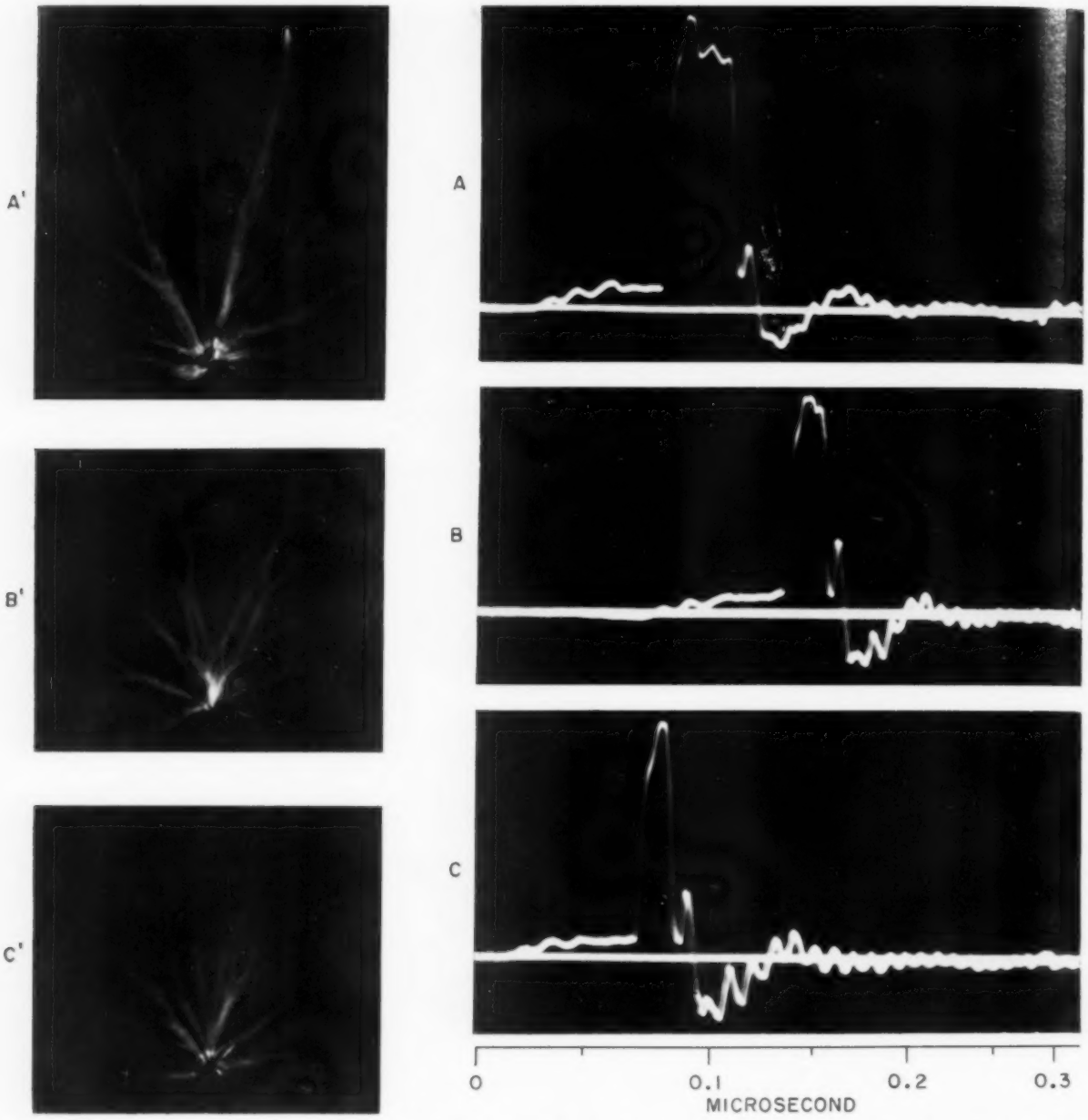

FIGURE 13. *Oscillograms of first current pip (A, B, and C) and discharge pictures (A', B', and C') on the same shots with voltage wave chopped quickly after start of first current pip.*

0.07 $\times t_c$, 145-surge, sphere negative. Cap spacing L=15 cm.

Such records were obtained by using the chopping circuit described in section 3. Oscillograms of discharge current and pictures of the discharge on the corresponding shot were taken at various chopping times. For these tests, the gap spacing L was held constant at a value that would nearly always give complete breakdown for a full-wave applied surge. Results were obtained for both polarities of the sphere and for both steeply and slowly rising surges. Because sphere polarity had a marked effect, a description of results for each polarity will be given separately.

The oscillograms of discharge currents (figs. 14A to 14F) and the corresponding pictures of the discharge (figs. 14A′ to 14F′) were obtained using $0.07 \times t_c$, 145-kv surges with the sphere positive and a gap spacing of 20 cm. Each picture is, of course, of a separate shot, so that the streamer pattern should not be expected to repeat in exact detail from picture to picture. Rather, this series of pictures has been

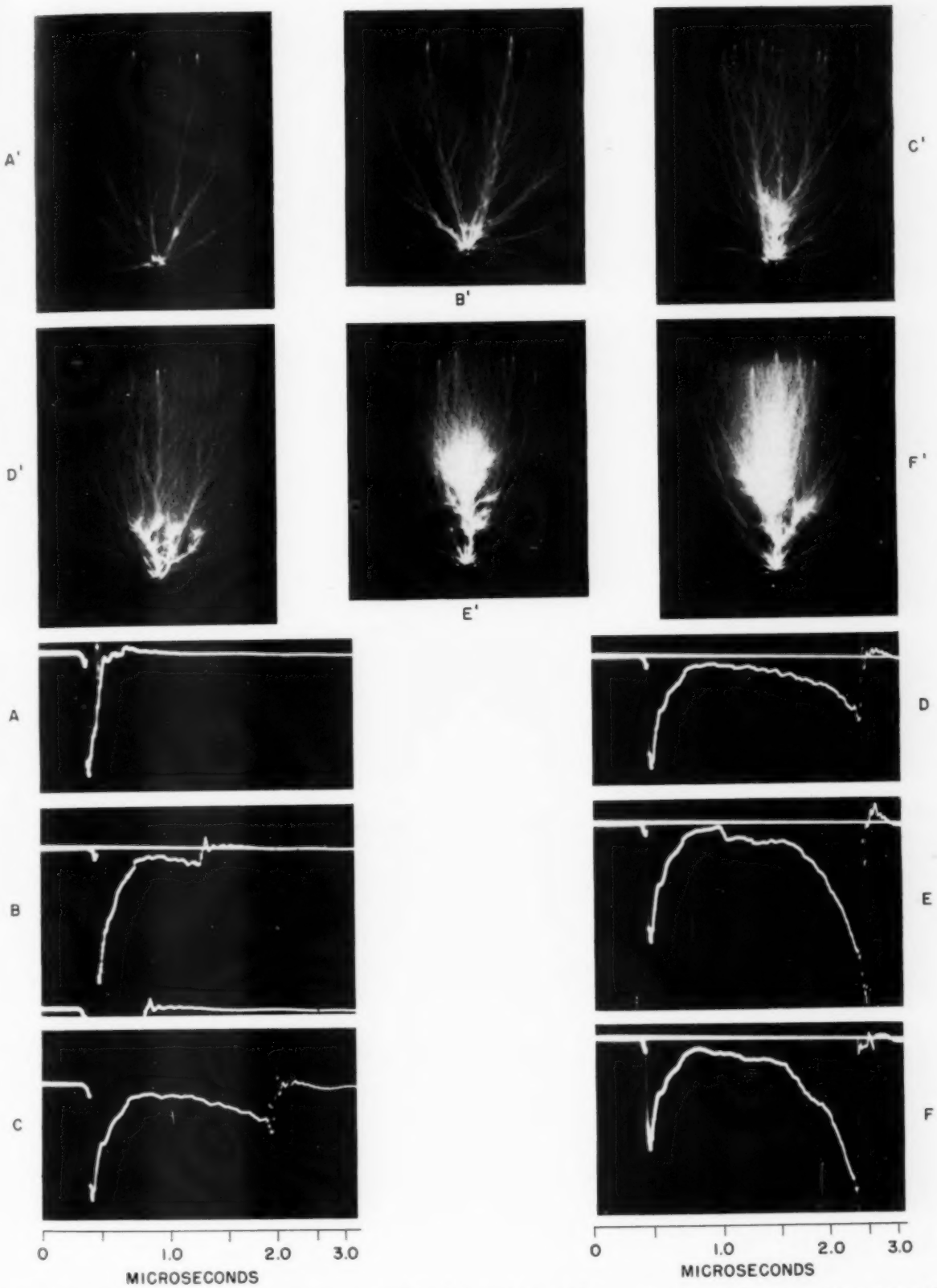

FIGURE 14. *Oscillograms of prebreakdown current and discharge pictures taken on the same shots with applied voltage* **chopped at** *various times after the first current pip.*

$0.07 \times t_c$, 145-kv surge (see figure 4G), sphere positive. Gap spacing 20 cm—breakdown would be complete if voltage were not chopped.

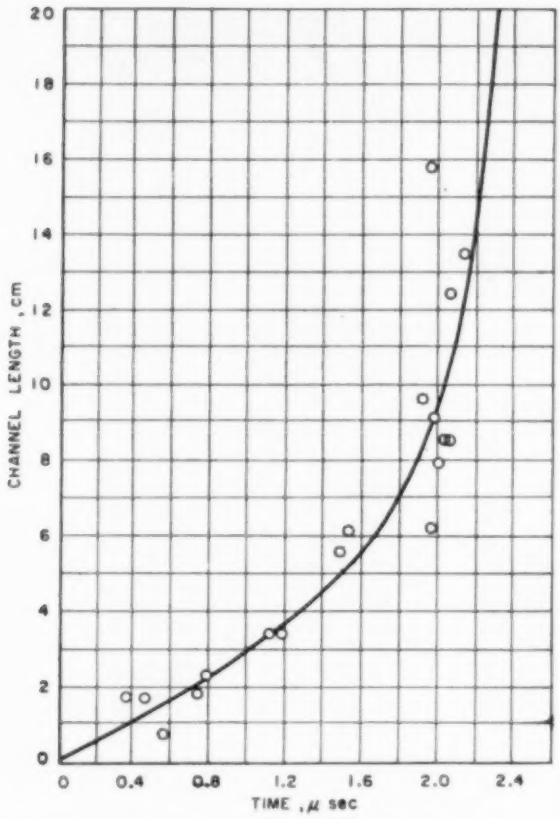

FIGURE 15. *Plot of channel length against time from first current pip to chopping.*

0.07×t_c, 145-kv surge. Sphere positive. L=20 cm.

chosen to show the discharge as nearly as possible as it would appear at successive intervals after the first current pip. The initial streamer patterns that form during the first discharge pip and before the second discharge rise starts (see figs. 14A and 14A′) are very similar in appearance to those previously obtained when the voltage was not chopped and breakdown did not occur (see figs. 4E and 4E′). The appearance of the discharge begins to change after the second discharge rise starts. This change consists of one or more bright discharge channels starting at or near the sphere. As the discharge current increases, these brilliant channels appear to extend in a rather tortuous path toward the plane electrode. Each bright tufted channel appears to be fed by a multitude of very fine hair-like filaments. These hair-like filaments are continuously developed from the leading fingers or branches of the growing channel and many appear to extend all the way to the plane electrode very early in the channel growth.

Approximate values for the rate of channel growth were obtained by measuring (1) the channel length on a discharge picture and (2) the time from first discharge pip to the chopping of the voltage wave on the corresponding current oscillogram. This was done for 18 sets of records similar to those shown in figure 14. A plot was then made of channel length against time to chopping of the voltage wave, and a smooth curve drawn through the plotted points as shown in figure 15. The slope of this curve gives approximate values for the instantaneous rate of channel growth. The channel starts to grow at a fairly slow and uniform rate of 3 cm/μsec. After it has reached a length of 3 cm it grows at an increasing rate. At midgap (10 cm) its rate of growth is about 20 cm/μsec. Beyond midgap it appears to grow much faster, and quickly reaches the plane electrode, causing complete breakdown.

Current oscillograms and discharge pictures shown in figure 16 were obtained in the same manner as those in figure 14, except that the slowly rising surge voltage ($1\times t_c$, 145-kv) was used. Breakdown occurs in essentially the same way, but the initial streamers that develop during the first current pip vary greatly in pattern and magnitude from shot to shot. As seen from figures 16A, 16B, and 16D, when the first discharge pip appears after the applied voltage has risen to a fairly large value, its magnitude is quite large and the initial streamers are fully developed and similar to those in figure 14. As seen from figures 16C, 16E, and 16F, when the first discharge pip appears before the applied voltage has reached a high value its magnitude is much less and the initial streamers do not extend very far from the sphere. However, the growth of the channel which leads to breakdown does not appear to be greatly affected by the magnitude or pattern of the initial streamers.

With the sphere negative, current oscillograms and discharge pictures for the voltage chopped at various times are shown in figures 17 and 18. The time delay from first discharge pip to breakdown varies more from shot to shot than with the sphere positive, and this increased the experimental difficulty in obtaining a set of illustrative records with the voltage chopped at various stages in the breakdown process. However, fairly satisfactory sets of records were obtained by taking a large number of shots. The initial discharge streamers bridge the gap on all shots for a steeply rising voltage (fig. 17), and on some shots for the slower rising voltage (fig. 18). Breakdown begins with the second discharge rise, and the increase in this current is not as gradual as for sphere positive. At about the same time as the second discharge rise starts, the discharge pictures show positive channels (plasma) beginning from the plane. These were noted by Norinder [10, fig. 16, p. 510] and referred to as "plate stems." These plane or anode channels grow toward the sphere in much the same way that a channel starting from the sphere grows toward the plane with sphere positive. As the channel approaches the sphere, breakdown occurs very rapidly, when the channel either contacts the sphere or connects with a channel developing from the sphere.

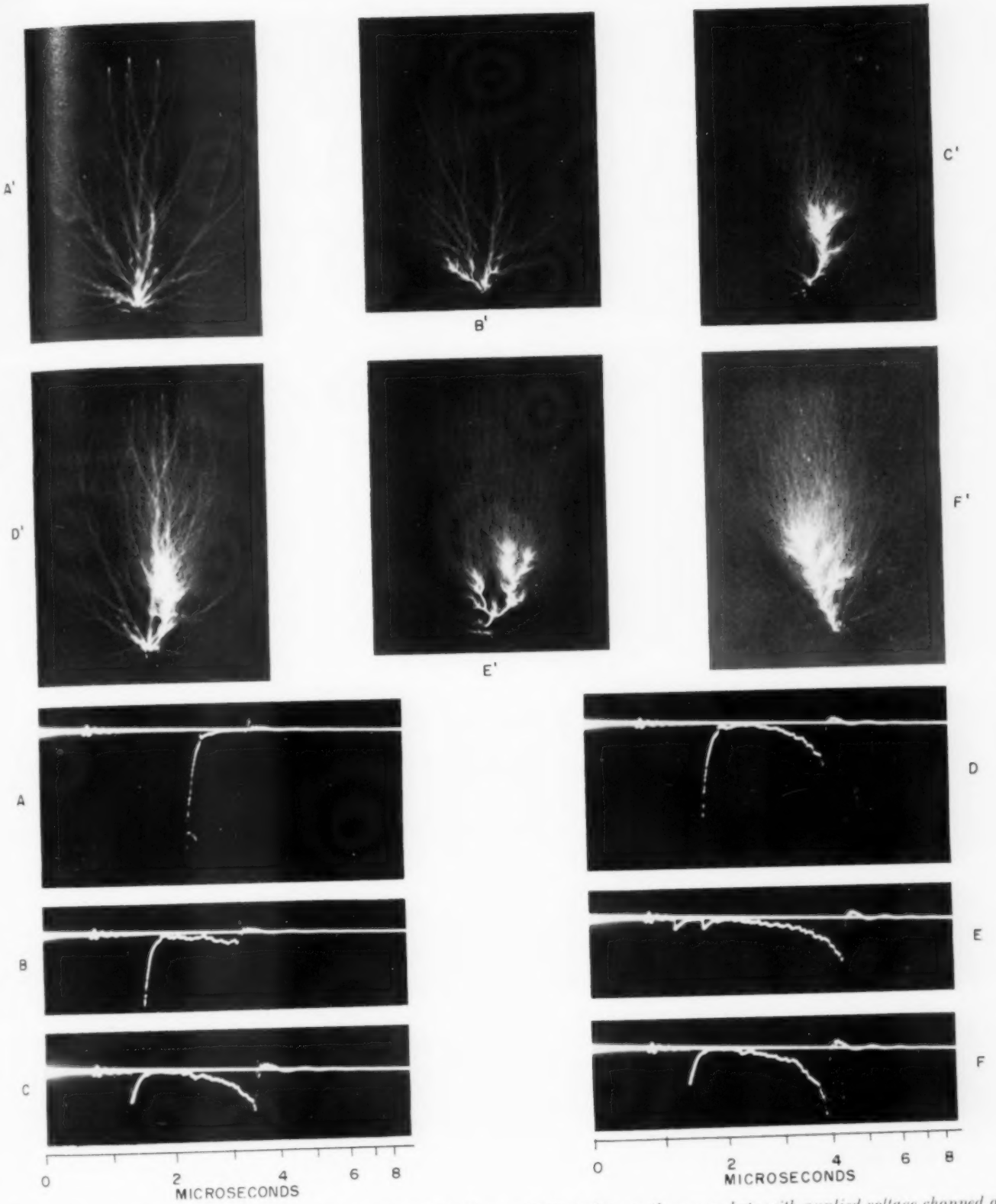

FIGURE 16. *Oscillograms of prebreakdown current and discharge pictures taken on the same shots with applied voltage chopped at various times after first current pip.*

1.85/μ, 145 kv surge (see figure 52), sphere positive. Gap spacing 20 cm—breakdown would be complete if voltage were not chopped.

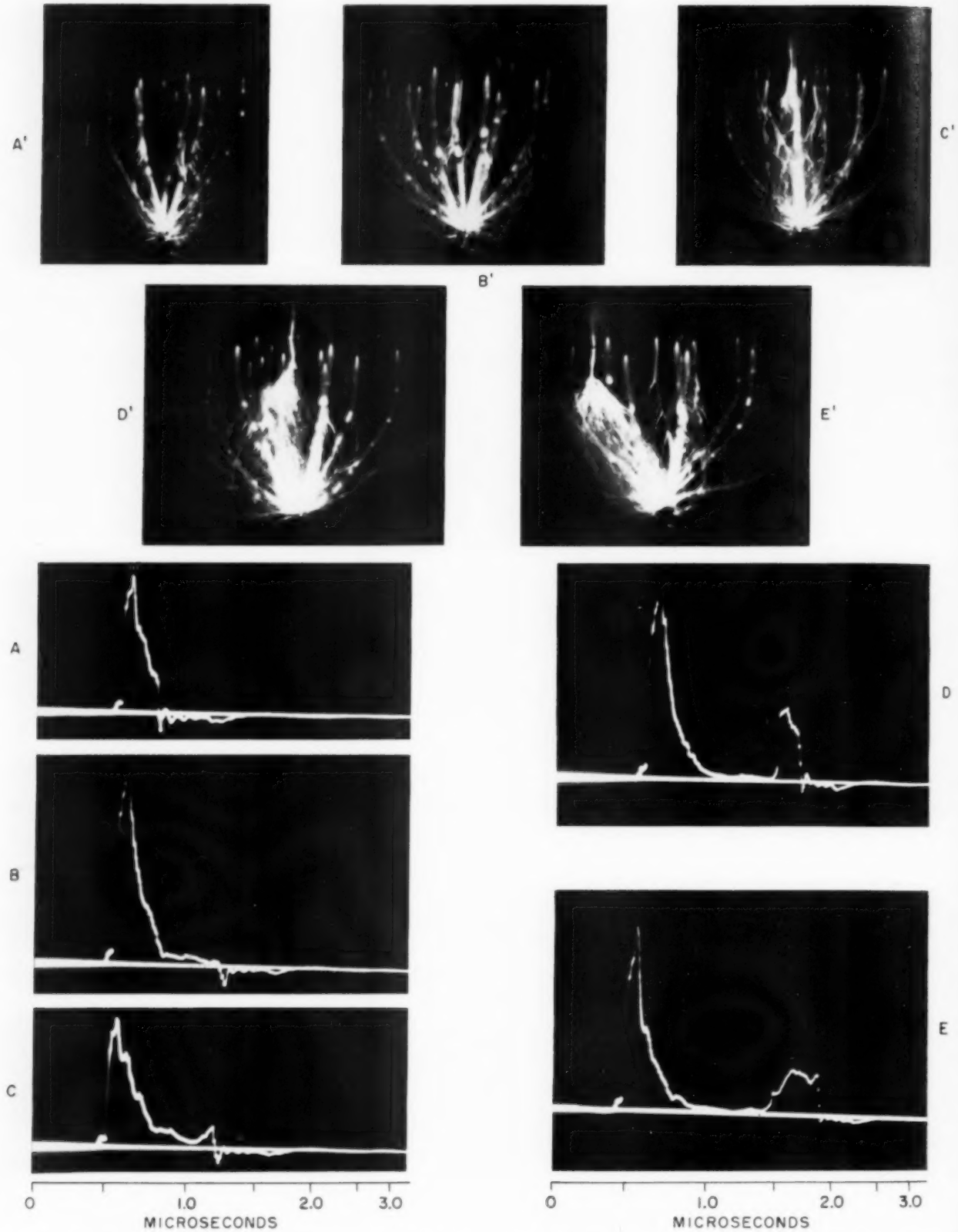

FIGURE 17. *Oscillograms of prebreakdown current and discharge pictures taken on the same shots with applied voltage chopped at various times after first current pip.*

$0.07 \times t_c$, 145-kv surge (see figure 6G), sphere negative. Gap spacing 11.5 cm—breakdown would be complete if voltage were not chopped.

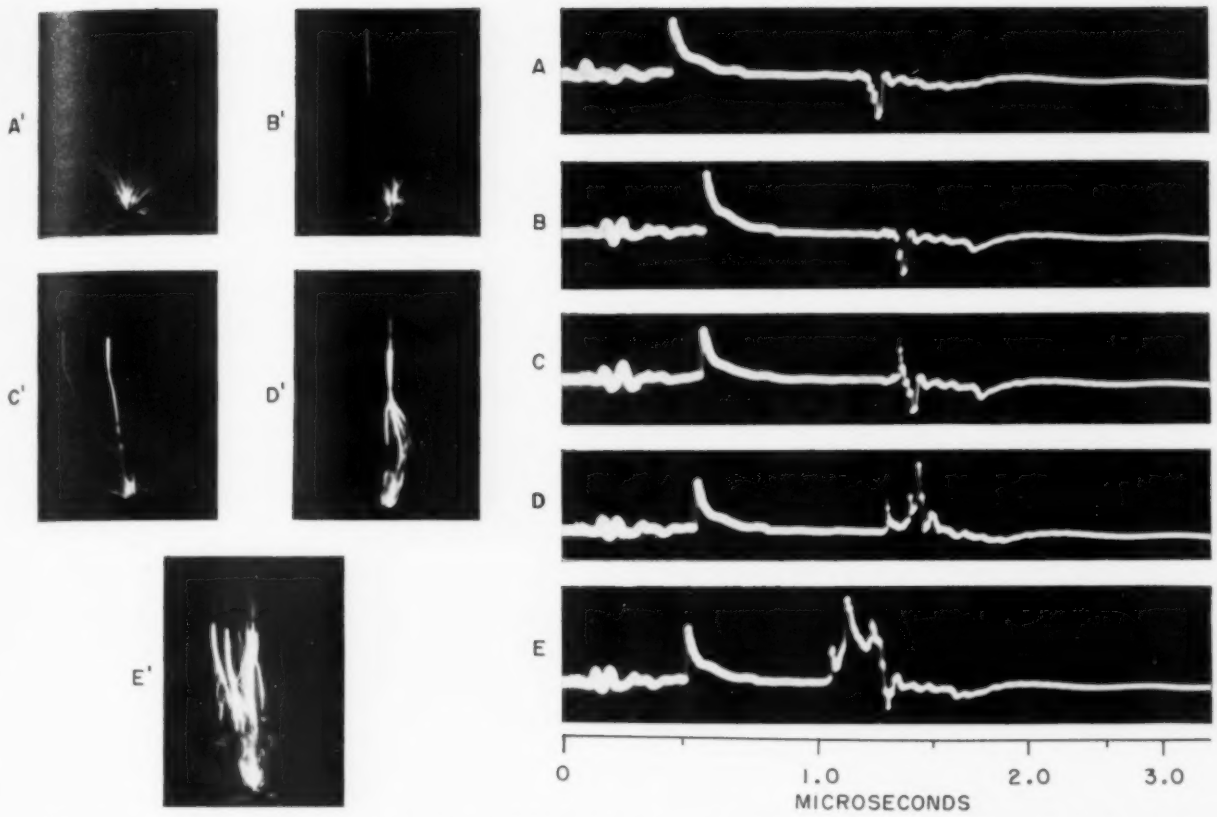

FIGURE 18. *Oscillograms of prebreakdown current and discharge pictures taken on the same shots with applied voltage chopped at various times after first current pip.*

$1\times t_0$, 145-kv surge (see figure 7D), sphere negative. Gap spacing 7.5 cm—breakdown would be complete if voltage wave were not chopped.

5. Analysis of Experimental Results

The reader may feel the need of referring to particular discharge pictures and current oscillograms while going over this last section. Table 1 summarizes these records and gives the corresponding figure numbers.

TABLE 1. *Summary reference tabulation of discharge picture an current oscillogram figures*

Sphere polarity	Wave front	Wave tail	Figure No.
	μsec		
Positive	0.07	100 μsec	4
Do	.07	Chopped very quickly	12
Do	.07	Chopped after 0.5 μsec	14
Do	1.0	100 μsec	5
Do	1.0	Chopped after 1 μsec	16
Negative	.07	100 μsec	6
Do	.07	Chopped very quickly	13
Do	.07	Chopped after 0.5 μsec	17
Do	1.0	100 μsec	7
Do	1.0	Chopped after 1 μsec	18

5.1. First Discharge Pip

In order to explain the initial discharge streamers and the current pip associated with them, it is necessary to make some additions and modifications to theories already postulated. Because of their high velocity of formation and the fact that they follow the lines of force of the applied field, these streamers cannot be compared to the pilot streamer or stepped leader stroke observed in lightning. Because they can travel across the gap without leading to breakdown they cannot be completely explained by Loeb and Meek's streamer theory [5], although this theory will be used here as the basis for their explanation. A brief summary of the proposed explanation will be given first, followed by details of various phases of the mechanism involved and correlation with the experimental data.

The term "streamers" is used because of their appearance on the discharge pictures. Actually these photographic traces (which will still be called streamers) are produced by balls or regions of high space-charge density with high ionization and excitation activity at their leading surface, being projected from the sphere toward the plane along lines of force of the applied field. If moving pictures at a speed of 10^{10} frames per second could be taken, each frame would presumably show a small localized bright area somewhere between the sphere and the plane, while regions outside the ball would give very little light. The ball does not consist of a group of

electrons or ions moving outward from the sphere,[4] but should be thought of as a traveling wave of high charge density which is propagated by a process in which new charges are continually produced at the leading surface of the ball by the high gradient there. In the path behind the ball there is left a high concentration of both positive and negative ions, with an excess of positive ions in case the sphere is positive and an excess of negative ions in case the sphere is negative. The net space charge left by the moving ball is enough to markedly reduce the original high gradient near the sphere, and thus inhibit for a short time further ionization activity in the path behind the ball. The streamers do not form conducting paths from the sphere to the plane because after the ball has crossed the gap the residual gradients are so low that no more ions are produced.

To explain the formation and propagation of the ball of high charge density, a process is suggested similar to that used by Loeb and Meek [5] in their streamer theory for uniform fields, which starts with the familiar electron avalanche. The chance of a free electron being correctly positioned with respect to the sphere to start an avalanche at the instant at which voltage is applied is quite small. But it has been demonstrated that the streamers do start at or very nearly at this instant for a gap out in the open under laboratory conditions, giving an average background density of ions in the air between the electrodes. Hence a free electron for avalanche initiation is probably produced from a negative ion by the high voltage gradient (90 kv/cm or more) near the sphere when voltage is applied. With the sphere positive a ball of positive space charge is formed by an avalanche, and with the sphere negative a ball of negative space charge. The two cases will be considered separately.

With the sphere positive, a negative ion situated in the high-field region near the sphere supplies a free electron, which starts ionizing neutral molecules and quickly forms an avalanche. As soon as this ionization process starts, it furnishes a plentiful supply of photons which liberate electrons in the nearby high field, where they, too, can readily start new avalanches. By means of this speedy relay of photons over the entire high-field region adjacent to the sphere, its upper half becomes rapidly "peppered" with avalanches.

The electrons are drawn out of the avalanches into the sphere, leaving balls of high positive space-charge density near the surface of the sphere. These balls will, of course, vary in size and charge density, but at least some of them will be capable of initiating positive streamers.[5] The space-charge balls enhance the field near them so that photo electrons liberated in the region just ahead of a ball form new avalanches which are attracted to the ball, leaving a volume of high net positive space charge just in front of the sphere. The flow of electrons through the ball and back toward the sphere tends to reduce the net positive space-charge density in the path left behind the ball. Thus the ball of high positive space-charge density, which also acts as a center of high ionization and excitation activity, remains small but moves rapidly away from the sphere, creating the positive streamer trace on the film.

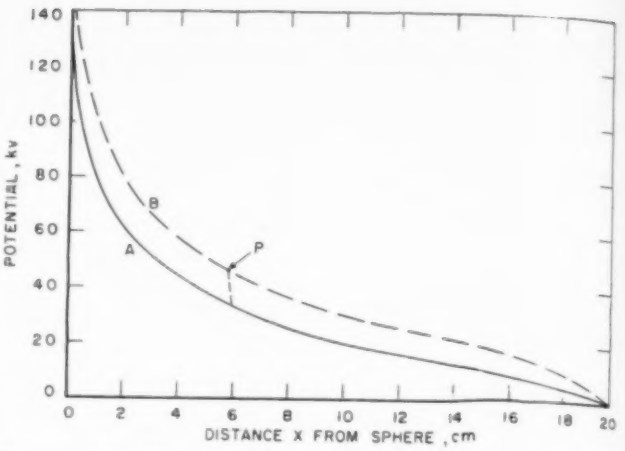

FIGURE 19. *Potential distribution along a streamer from the sphere to the plane.*

Curve A—as computed neglecting space charge. Curve B—as estimated after space charge ball has reached plane.

During this process the positive ions do not move appreciably, but remain essentially where they are produced, and the electrons move only short distances toward the sphere. The high speed of formation of the streamers is accounted for by the motion of the ball of high net positive space-charge density, which produces a momentary high voltage gradient at each point along the streamer path as it passes that point.

In the path left by the ball there is a high density of both positive ions and electrons, with a slight excess of positive ions. This net positive space charge changes the potential distribution between the sphere and plane, as indicated in figure 19. Curve A is the potential computed from the applied voltage with space charge neglected. Curve B is an estimate of the potential after the ball has reached the plane. When the ball is at a given point P, the potential follows curve B from the sphere to point P and curve A from point P to the plane. The discontinuity at point P is due to the high positive charge density in the ball, and it produces the high momentary gradient necessary to project the ball. The gradient as estimated from curve B is not high enough to produce ionization or excitation except in the region very near the sphere. The bright stems near the sphere (see figs. 4E′ and 14A′) indicate ionization in this region, which probably persists

[4] The experiments show that initial streamers travel the entire gap length in times of about 10^{-8} seconds (measured velocities of propagation being from 500 to 1,000 cm/μsec). As the drift velocity of electrons in a region of high gradient (100 kv/cm) is only about 20 cm/μsec, and that of ions less than 0.2 cm/μsec, the process of streamer formation cannot be explained by ions or electrons moving along its entire length.

[5] The first current nip is caused not by one or a few initial streamers but by a large number. An estimate of the total number of streamers that bridge the gap on a given shot can be obtained by counting the bright spots at the plane end of the gap on the discharge picture and multiplying by three, the factor three entering because of the depth of focus of the lens. (The lens has a focal length of 58 mm, and the maximum aperture of f/1.9 was used with the camera at a distance of 76 cm from the gap, the depth of focus thus being 2.5 cm.) The number of streamers and their patterns vary greatly from shot to shot but in general for a given applied voltage the shorter the gap the more streamers. For the sphere positive, a gap spacing of 20 cm, and the steeply rising surge, the average number of streamers per shot was about 50.

until the additional space charge it produces decreases the gradient further. Thus the path left by the rapidly moving ball will not become a highly conducting plasma until some other mechanism for increasing ion density becomes active.

With the sphere negative, the electron avalanches formed in the region near the sphere initiate positive streamers which quickly propagate the short distance to the sphere. As the streamers approach the sphere, the high positive space-charge densities at their tips make the already extremely high gradients near the sphere even higher, and, largely because of these exceedingly high gradients, electrons are immediately released from the sphere.

The mechanism of electron release could be by any one or a combination of the following: (1) positive ion bombardment of the sphere, (2) high-energy photons impinging on the sphere, (3) field emission. In any event, more than sufficient electrons will be released to equalize the positive space-charge density, and a small volume or ball of high negative space charge will form near the sphere in line with each streamer. This is likely because of the high gradient near the sphere due to the applied voltage. Each small ball of high negative space-charge density can propagate away from the sphere by a mechanism nearly the same as for propagation of a positive ball, that is, not only by electron motion but largely because of the continuing generation of new electrons ahead of this volume. Here again, the ionizing and excitation activity is largely confined to this small ball of high space-charge density, which propagates rapidly toward the plane. Thus with the sphere negative, negative streamers develop from the sphere in much the same manner as positive streamers with the sphere positive. The experimental results indicate this to be true, as may be seen by comparing figures 4A′ to 4E′ with figures 6A′ to 6D′ (gap spacings too long to yield breakdown), and figures 12A′ to 12C″ with figures 13A′ to 13C″ (gap spacings giving breakdown but voltage chopped quickly after first discharge pip starts). The negative streamers leave numerous positive ions but a negative net space charge, which initially consists of electrons. The electrons, however, are quickly attached to oxygen molecules to form negative ions. Thus a potential distribution similar to that shown by curve B in figure 19 can persist for a short time and inhibit further ionization.

With the sphere negative, however, the initiation of a streamer requires a shorter gap spacing for a given applied voltage, and the velocity of propagation is less. To account for these experimental results, consider the development of an electron avalanche in the two cases: (1) sphere positive and (2) sphere negative. For the sphere positive, the electrons move in the direction of increasing gradient, because they travel toward the sphere or toward the ball of high positive space-charge density. For the sphere negative, the electrons move in the direction of decreasing gradient, because they travel away from the sphere or away from the ball of high negative space-charge density. Thus, the electron avalanches develop faster for the sphere positive, giving a higher velocity of streamer propagation. Also, the initiating avalanches can form positive streamers for lower applied gradients near the sphere with the sphere positive and thus produce streamer initiation for longer gap spacings.

The question now arises as to how much space charge would be required to suppress ionization, and whether the first discharge pip furnishes this amount. By applying Laplace's equation to the case of concentric spheres it can be shown that for a charge density in the space between the spheres, proportional to the reciprocal of the distance from the center, the gradient will be constant at all points between the spheres. By assuming such a charge distribution, and taking (1) the diameter of the inner sphere to be 1.6 cm, (2) the diameter of the outer sphere to be 40 cm, and (3) the potential difference between the speres as 145 kv, the total space charge required to give a uniform gradient was computed and found to be 3.4×10^{-6} coulombs. The average first discharge pip for a 145-kv surge (sphere positive) and gap spacing of 20 cm was found experimentally to have a peak current of 19 amp and a time to half value of 0.07 μsec. Integrating this current pulse to obtain the total charge supplied by it, gives 1.9×10^{-6} coulombs. This is about one-half the value computed for concentric spheres to give space charge yielding a uniform gradient. The factor one-half is about right to convert from the case of concentric spheres to sphere-plane electrodes.

The above computation is only intended to indicate that the space charge is of the correct order of magnitude to materially reduce the longitudinal voltage gradient in the region near the sphere. The assumptions used, which led to a constant gradient between sphere and plane, are not easily justified. It could be argued that the space charge per unit length of streamer (path left by the ball) would be constant. For concentric spheres this would give an average charge density proportional to the reciprocal of the square of the distance from the center. Computations based on such a charge distribution yield a gradient near the sphere actually higher than that obtained neglecting space charge. No definite statement as to exact charge distribution in the streamers can be made at this time. However, it should be readily possible for this space charge to alter the potential distribution as proposed in figure 19.

Another complication to be considered in such computations is that the space charge, just after formation of the streamers, would probably be mainly concentrated inside them. This would lead to a transverse gradient, i. e., perpendicular to the direction of the streamers. A rough computation of this transverse gradient can be made. The total number of streamers has already been estimated to be 50 (see footnote 5), and the streamer width as determined from measurements on figure 14A′ is 3 mm. By using these values and assuming the streamers to be cylinders with lengths equal to gap spacing, $L=20$ cm, the estimated total volume of all streamers is found to be 70.7 cm^3, giving for 1.9×10^{-6} coulomb total charge, an average charge density inside the

streamers of 0.027×10^{-6} coulomb/cm^3. The maximum voltage gradient at the surface of a streamer due to this charge was approximately computed and found to be about 18 kv/cm, which is not sufficient to produce ionization. Thus, even when both longitudinal and transverse gradients are considered, the space charge introduced by the first discharge pip appears adequate to suppress further ionization.

5.2. Second Discharge Rise and Breakdown

For gap lengths sufficiently short or (in case voltage magnitude had been changed) for voltages sufficiently high, the first discharge pip is followed rather quickly by a second increase in current which, in general, rises at an increasing rate until breakdown occurs. As indicated in the experimental results, the mechanism of breakdown is different for the two sphere polarities.

a. Sphere Positive

With the sphere positive, a highly conducting channel starts to form at the surface of the sphere and grows toward the plane in a tree-like pattern with one or more main arms, each with many fingers which are fed by a multitude of fine filaments. This plasma channel acts as a conducting arm reaching out from the sphere, and as it extends itself toward the plane there is an ever-increasing gradient between the ends of the fingers and the plane. Thus, once started, it leads to complete breakdown unless the voltage is chopped.

The differences between streamers, which accompany the first discharge pip, and channels, which lead to breakdown, must be considered. They will be referred to merely as streamers and channels. Experimental evidence indicates the following differences: (1) Streamers propagate at a very high and probably nearly constant velocity of from 500 to 1,000 cm/μsec, while channels start to grow at a fairly low rate (3 cm/μsec) and their rate of growth increases as they span more of the gap, being about 20 cm/μsec at midgap; (2) streamers do not constitute a highly conducting plasma, but channels do; (3) streamers seem to follow along the original geometric lines of force of the electric field, but channels grow in a random zigzag course; (4) channels create a much more intense photographic record than streamers, suggestive of a much higher temperature and ion density in their core.

As already indicated, the streamers form quickly and leave behind a space-charge distribution which changes the original nonuniform field between sphere and plane to a more nearly uniform field. Thus immediately after the streamers have formed, the gradient at all points in the gap is below that required for ionization by collision, and if breakdown is to develop some other source of ionization must arise.

Although the streamers form almost instantly, the channels take enough time to develop so that the energy fed into their leading tip produces gas temperatures sufficiently high to yield a copious supply of ions. As the channel is formed it serves as a good conductor from its origin at the sphere to its leading end. Thus there will be a high gradient at the tip end of the channel, and filaments similar in their mechanism of formation to the initial discharge pip streamers will form at the tip end and feed more energy into the channel, causing it to propagate. The direction of channel formation at any instant depends upon the adjacent electric field strength and direction at that instant. The field configuration at any instant is fixed largely by the particular space charge distribution at that instant. Because the space charge distribution depends upon all previous ionization activity in the gap, it has random local irregularities and varies from instant to instant. This accounts for the random zigzag course of the channels.

After a channel has started it develops (as discussed above) until it bridges the gap, causing breakdown. Just how and why a channel starts is not self-evident. Because of the inhibiting space charge left by the streamers, it would appear that no further discharge could take place until this space charge had been at least partially cleared from the region near the sphere. This is, of course, true for longer gap spacings at which no breakdown occurs. As gap spacing is decreased a value is reached where breakdown occurs on some shots. In these cases the small bright stem of an initial streamer serves as the beginning of a bright channel. If the initial streamer pattern is such as to produce a sufficiently high gradient in a region near a bright stem, a channel will start to develop. Other streamer patterns may not produce a sufficiently high gradient. Thus the development of a channel is at least partly a matter of chance, the chances being greater for shorter gap spacings (assuming the same applied voltage surge). The fact that the channel does not continue to follow the same path as the streamer is readily accounted for by remembering that the gradient along the streamer (longitudinal gradient) tends to be uniform and fairly low because of space charge. Near the sphere the transverse gradient just outside a streamer should be much greater than the longitudinal gradient. Thus there should be more likelihood of a channel branching away from a streamer stem, as borne out by the experimental results. For the sphere positive (and provided not too great an overvoltage is applied), breakdown takes place along a zigzag channel that has completely spanned the gap (see figs. 20A and 21A).

b. Sphere Negative

With the sphere negative, breakdown is not initiated by a zigzag channel starting from the sphere. This would indicate that conditions in the region near the sphere are not propitious for channel development. One of these conditions is that the transverse gradient adjacent to the streamers be very high. This would hold for positive streamers because positive ions would diffuse into this region quite slowly. It would not hold for negative streamers, because electrons could quickly diffuse into lateral regions, forming negative ions and thereby reducing the gradient. The fact that zigzag

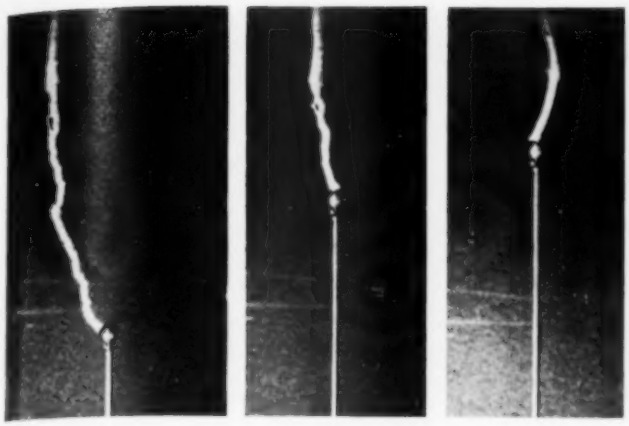

FIGURE 20. *Spark discharge pictures (filter on camera).*
0.07×100, 145-kv surge, sphere positive. A, $L=20$ cm; B, $L=10$ cm; C, $L=5$ cm.

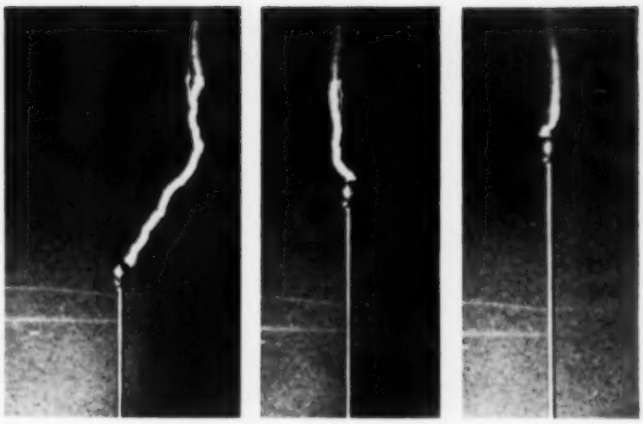

FIGURE 21. *Spark discharge pictures (filter on camera).*
1×100, 145-kv surge, sphere positive. A, $L=15$ cm; B, $L=7.5$ cm; C, $L=3.8$ cm.

channels do not form from the sphere when it is negative helps to account for the observed result that, for the same voltage, a longer gap will break down when the sphere is positive than when it is negative.

It will be remembered that the appearance of negative streamers is quite similar to that of positive streamers for gap spacings longer than those at which breakdown may occur. The change in appearance with further decrease in gap spacing, at the same applied surge voltage, is presumably due to the higher gradients existing at the lower spacings. The most noteworthy change in appearance is the more intense photographic record, indicative of an increase in ionization activity. The increased brightness begins at the sphere and follows the streamers, going farther out into the gap the longer the voltage is left on (see figs. 17A′, 17B′, and 17C′). This phenomenon requires a longer time to develop than the streamers, because when the voltage is chopped very quickly (see fig. 13) it does not occur. Thus it appears that the streamer itself develops into a straight channel as more energy is fed into it. Complete breakdown appears to occur in this way for a sufficiently short gap or sufficient overvoltage.

Another change in appearance is the addition of auxiliary streamers starting out nearly perpendicularly from the initial streamers and then curving down toward the sphere. These are probably positive streamers, initiated because of the high transverse gradient in the region between the initial streamers at a considerable distance from the sphere.

A third change in appearance is that the initial streamers acquire dots or small regions of greater ionization activity along their length. The spacing of these dots is random and some streamers show none. After the initial streamers have traversed the gap there is not sufficient voltage to maintain longitudinal ionizing gradients along the entire streamer. This is just barely true for the shorter gap spacings used with sphere negative, and if the gradient is not exactly uniform along the streamers these dots could be regions of high gradient. These changes in appearance of negative streamers at gap settings leading to breakdown indicate that, for very short gap spacings or considerable overvoltage, breakdown would occur by a streamer developing into a channel as more energy is fed into it.

However, at gap spacings just short enough to give breakdown, there is another mechanism involved in breakdown. Plasma channels start from the plane and develop outward toward the sphere in random paths (see figs. 17D′ and 17E′) similar to the channels which start from the sphere with sphere positive. These plane channels are probably initiated by high gradients at the plane created by the negative space charge of the initial streamers. They would start as positive streamers and quickly develop into channels, which follow a path perpendicular to the plane part way across the gap and develop further in a zigzag path by the same mechanism that produces zigzag channels from the positive sphere. Breakdown is then completed by these zigzag channels proceeding all the way to the sphere or meeting a channel developing from the sphere along the path of an initial negative streamer.

This explanation of breakdown with the sphere negative would predict that the mechanism of breakdown changes as gap spacing is reduced (or overvoltage increased). With very small overvoltage, breakdown would result from a zigzag channel developing from the plane. With high overvoltage, the breakdown channel would develop along the same path used by an initial streamer. This is shown to be true by the photographs of complete spark breakdowns for sphere negative (see figs. 22 and 23) taken with a dense filter at several different gap spacings. Similar photographs taken with the sphere positive (see figs. 20 and 21) indicate that here also, if gap spacing is sufficiently reduced, breakdown occurs by an initial streamer developing into a channel. These results suggest that the mechanism of breakdown in a uniform field gap is first a rapidly forming initial streamer, which because of the high gradients available quickly changes into a channel. This would account for

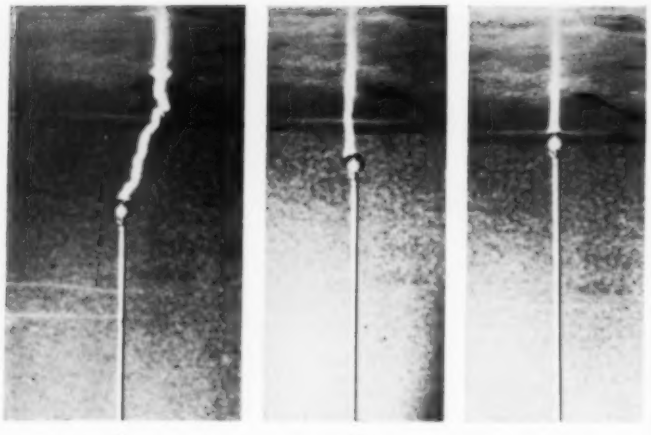

FIGURE 22. *Spark discharge pictures (filter on camera).*

0.07×100, 145-kv surge, sphere negative. A, L=10 cm; B, L=6.5 cm; C, L=3.8 cm.

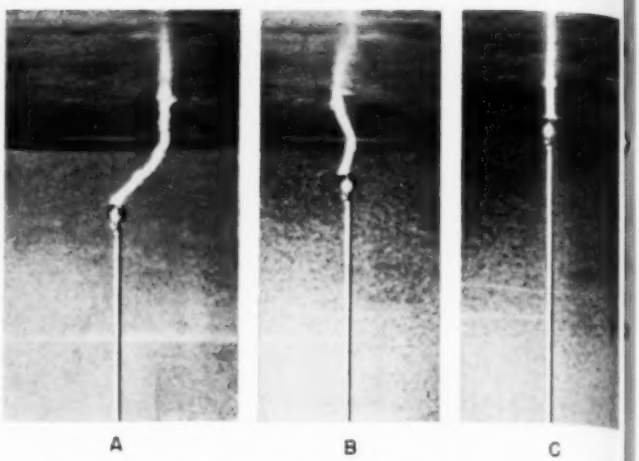

FIGURE 23. *Spark discharge pictures (filter on camera).*

1×100, 145-kv surge, sphere negative. A, L=9 cm; B, L=6.5 cm; C, L=3.8 cm.

the straight spark paths found for uniform field gaps [16].

5.3. Effect of Rate of Voltage Rise

The foregoing explanation of discharge mechanism in a nonuniform field gap has been based largely on data obtained when voltage is suddenly applied to the gap—that is, with a voltage rise time of 0.07 μsec. Data obtained using a rise time of 1 μsec were, in general, the same; but the magnitude of the first discharge pips and the size of the corresponding discharge patterns varied considerably from shot to shot. Because the first discharge pip and the ionization associated with it have such a short duration, they can happen on the rising front of a slowly rising voltage wave. The value of voltage that determines their magnitude is variable from shot to shot and is usually less than the peak value. After the initial discharge is formed, further discharge phenomena are inhibited by the space charge it leaves behind. Thus, unless gap spacing is such that complete breakdown occurs, no further discharges take place after the first discharge pip even though the applied surge voltage continues to rise. The magnitude of the first discharge phenomena depends on the exact value of voltage at the instant of discharge initiation. Consequently, any scattering in "time to first discharge pip" results in a considerable variation in current magnitude and in corresponding photographic records.

Experimental results showed that the later the first discharge pip occurred on the rising front of the voltage wave (that is, the higher the voltage at instant of occurrence), the larger the magnitude of first discharge pip and streamer length. The transition from initial discharge to breakdown is probably very nearly the same for a 1-μsec front voltage as for the faster voltage front, as may be seen for the sphere positive by comparing the records shown in figure 16 with those in figure 14. With the sphere negative the initial discharges do not appear to extend as far into the gap (see fig. 7), and there might be a question as to whether plate stems and channels can form. However, photographic records (fig. 18) using chopped voltages show that they do form, and breakdown occurs in much the same manner as for the steeply rising voltage. This can be accounted for when one realizes that the streamers may extend farther than the photographic records show. At the ends of these streamers a large supply of electrons is produced during the first discharge pip, and there is an interval of nearly 1 μsec before initiation of the plate stems (as seen in fig. 18). During this interval, these electrons can drift toward the plane and, as a negative space charge, cause the high gradients necessary there to initiate positive streamers and channels.

The experimental curves shown in figure 10 indicate another difference in breakdown characteristic depending upon the rate of voltage rise. These curves show that for a steeply rising surge, breakdown is more apt to occur at the greater gap spacings than with a slowly rising surge. As already mentioned, the particular pattern of the initial discharge streamers, which varies from shot to shot, determines whether or not breakdown will occur. In general, probably, the greater the magnitude (i. e., total coulombs) of the first discharge pip, the greater the chance for breakdown to follow. The first discharge pip is of higher magnitude on the average for a steeply rising surge, and thus breakdown is more likely to develop at greater gap spacings.

6. Summary

1. When a surge voltage of sufficient magnitude and duration is applied to a sphere-plane gap (nonuniform field) the prebreakdown discharge phenomena are divided into two phases: (a) the initial streamers which produce the first discharge pip and (b) the somewhat later development of a good conducting channel which causes a second rise in discharge current. This second current rise increases exponentially to breakdown unless the applied voltage is chopped.

2. The statistical nature of the experimental results is demonstrated by summaries of the following measured quantities: (a) time delay from start of voltage surge to first discharge pip, (b) peak current value of first discharge pip, (c) percentage of complete breakdowns for a given gap spacing, and (d) time delay from first discharge pip to breakdown. Before voltage is applied the instantaneous ion pattern near the sphere is changing continuously, thus accounting for the variations in quantities (a) and (b) on successive applications of the surge. The random nature of quantities (c) and (d) is accounted for by variations in the first discharge streamer magnitude and pattern on repeated surge applications.

3. The initial streamers propagate from the sphere toward the plane along lines of force of the applied electric field at very high velocities, 500 cm/μsec for the sphere negative and 800 cm/μsec for the sphere positive. During the initial discharge the surge of current that flows to the sphere rises to a peak value of 1 to 30 amp (depending on gap spacing and sphere polarity) in about 0.008 μsec and then decreases approximately exponentially to zero, reaching half value in about 0.08 μsec. For gap spacings at which breakdown is likely to occur, the initial streamers bridge the entire gap from sphere to plane without causing immediate breakdown. The formation of the initial streamers produces a space-charge distribution in the gap, which apparently inhibits further ionization unless conditions are such that breakdown can occur.

4. If complete gap breakdown is to take place, a second rise in current signifies the development of a conducting channel between the electrodes. With the sphere positive this channel starts to form near the surface of the sphere and follows a zigzag path to the plane. With the sphere negative the conducting channel starts out perpendicular to the plane, but after a short distance changes its course and makes a zigzag path to the sphere. Breakdown is completed when this highly conducting channel completely spans the gap.

5. For gap spacings much shorter than those first causing breakdown, i. e., for considerable overvoltage, the gap breakdown occurs by the development of one of the initial streamers into a conducting channel. The breakdown path is then not zigzag but more nearly straight and seemingly follows a "line of force" of the geometric field. It is suggested that this is the normal type of breakdown for uniform field gaps.

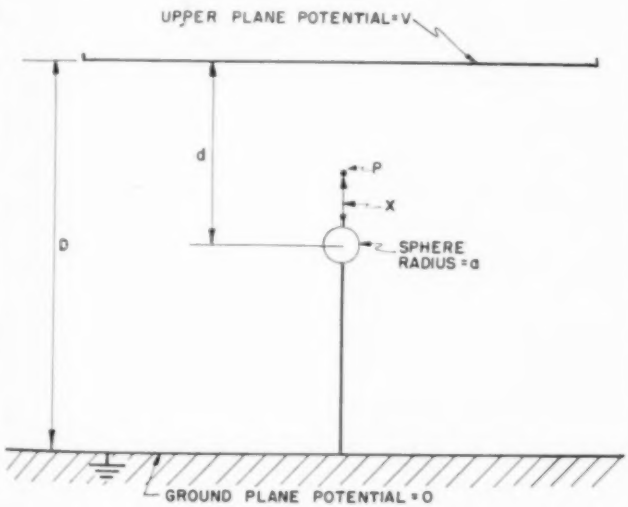

FIGURE 24. *Schematic diagram of sphere-plane electrodes as used to obtain experimental results.*

In Peek's formula, eq (1), $\delta=d-a$ and $y=d-a-x$.

7. Appendix. Computation of Voltage Gradient Between a Sphere and a Plane

For an infinite plane and sphere isolated in space and maintained at a constant potential difference, the gradient along the perpendicular from the plane to the center of the sphere can be computed by a formula given by Peek [17]. In this formula:

V = Potential difference between sphere and plane.
a = radius of the sphere.
δ = the distance from the plane to the surface of the sphere along the perpendicular from the plane to the center of the sphere.
y = the distance from the plane to the point at which gradient is to be determined along the perpendicular from the plane to the center of the sphere.
$p=1+\delta/a$
$f=\frac{1}{4}[(2p-1)+\sqrt{(2p-1)^2+8}]$
E_y = gradient along the perpendicular from the plane to the center of the sphere at a distance y from the plane. E_y is then given in volts per centimeter if dimensions are in centimeters and V is in volts by the equation

$$E_y=V\frac{2\delta[\delta^2(f+1)+y^2(f-1)]}{[\delta^2(f+1)-y^2(f-1)]^2}. \qquad (1)$$

Results obtained using eq (1) would be correct if the plane were at ground potential, located on the floor, and the sphere at the high potential located above the plane, provided the effect of the lead connecting the sphere to the high potential could be neglected. In the present experiments these conditions were not fulfilled and Peek's formula was not considered to be a sufficiently close approximation.

Figure 24 shows the arrangement of (1) ground plane at potential zero, (2) high voltage plane at potential V, and (3) sphere at potential zero as used in the present experiments. By neglecting the effect of the tube supporting the sphere, a system of charges Q_1, Q_1', Q_1'', Q_2', and Q_2'' can be chosen to make the potential very nearly zero at every point on the surface of the sphere. The magnitude and position of Q_1 is chosen so that it, together with the surface charges on the two planes, makes the potential zero everywhere on the surface of the sphere. Charges Q_1' and Q_1'' are image charges for Q_1 which

keep the potentials of the two planes at their proper values. Charges Q_2' and Q_2'' are image charges inside the sphere of Q_1' and Q_1'' to keep the sphere at zero potential. Further image charges were neglected. Using this system of charges and making some approximations based on a being much smaller than d or D, the following formula for E_x, the gradient at the distance x from the surface of the sphere along the perpendicular from the high voltage plane to the center of the sphere, was derived:

$$E_x = V\left\{\frac{1}{D}+\frac{D-d}{D}a\left[\frac{1}{\left(a-\frac{a^2}{D-d}+x\right)^2}+\frac{1}{(2d-a-x)^2}\right.\right.$$

$$-\frac{1}{[2(D-d)+a+x]^2}+\frac{a}{2d\left(a-\frac{a^2}{2d}+x\right)^2}$$

$$\left.\left.+\frac{a}{2(D-d)\left[a+\frac{a^2}{2(D-d)}+x\right]^2}\right]\right\}. \qquad (2)$$

In this equation the effect of the mounting tube for the sphere was neglected, which is probably justified if its diameter is small. To determine approximately how well this holds, a more complicated computation was carried out for the specific case of $d=10a$, $D=40a$, and radius of the mounting tube$=a/4$. Charges along the axis of the mounting tube were considered with their images in addition to the charges used in the derivation of eq (2). They were chosen to make the potential at the surface of the mounting tube nearly zero at all points. The results of this computation for the one specific case mentioned are compared with those obtained by eq (1) and (2) in the following table:

	Mounting tube considered	Equation	
		(2)	(1)
Gradient at surface of the sphere in volts per centimeter	$0.8715\times V$	$0.884\times V$	$1.061\times V$

The value obtained using eq (2) in which the mounting tube was neglected is nearly the same as that obtained when mounting tube was considered. Both values are somewhat lower than that obtained using eq (1), Peek's formula. Equation (2) was considered to be a sufficiently close approximation and for the actual dimensions used in the experimental work and for 145 kv applied to the plane the values of gradient at various distances from the sphere are shown in figure 25 for gap spacings of 10, 20, 30, 40, and 50 cm.

WASHINGTON, December 28, 1955.

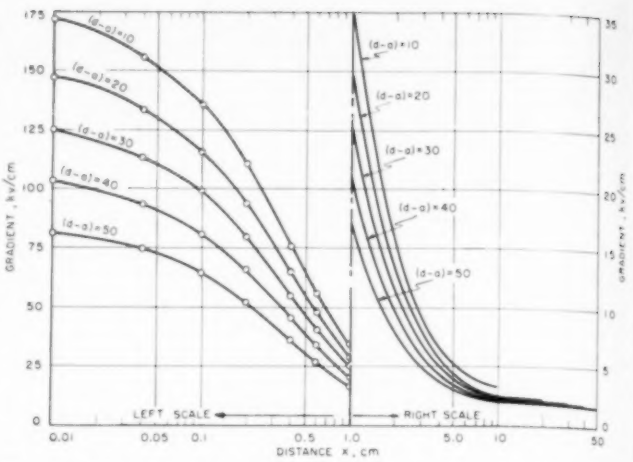

FIGURE 25. *Curves of voltage gradient as computed from eq (2) plotted against distance, x, from the surface of the sphere (see figure 24).*

$V=145$ kv, $D=86.4$ cm, $a=0.794$ cm.

8. References

[1] Leonard B. Loeb, Basic processes of gaseous electronics, chs. VIII and IX (Univ. of California Press, 1955). Additional references at the end of each chapter in this book.

[2] F. A. Maxfield and R. R. Benedict, Theory of gaseous conduction and electronics, page 270 (McGraw-Hill Book Co., Inc., New York, N. Y., 1941).

[3] F. Llewellyn Jones and A. B. Parker, Electrical breakdown of gases—I. Spark mechanism in air, Proc. Roy. Soc. London [A] **213,** 185 (1952).

[4] J. Dutton, S. C. Hayden, and F. Llewellyn Jones, Formative time lags in the electrical breakdown of gases, Brit. J. Appl. Phys. **4,** 170 (1953).

[5] Leonard B. Loeb and John M. Meek, The mechanism of the electric spark (Stanford University Press, 1941).

[6] M. A. Biondi, Microwave gas discharge, Elec. Eng. **69,** 806 (1950).

[7] W. P. Allis and S. C. Brown, High frequency electrical breakdown of gases, Phys. Rev. **87,** 419 (1952).

[8] Sanborn C. Brown, High-frequency gas-discharge breakdown, Proc. IRE **39,** 1493 (1951).

[9] Harald Norinder and Oskars Salka, Mechanism of positive spark discharges with long gaps in air at atmospheric pressure, Arkiv Fysik **3,** No. 19, 347 (1951).

[10] Harald Norinder and Oskars Salka, Mechanism of long-gap negative spark discharges in air at atmospheric pressure, Arkiv Fysik **5,** No. 24, 493 (1952).

[11] Harald Norinder and Oskars Salka, Screens in long discharge gaps, Arkiv Fysik **6,** No. 17, 151 (1953).

[12] J. H. Hagenguth, A. F. Rohlfs, and W. J. Degnan, Sixty-cycle and impulse sparkover of large gap spacings, Trans. AIEE **71,** 455 (1952).

[13] R. F. Saxe and J. M. Meek, The initiation mechanism of long sparks in point-plane gaps, Inst. Elec. Engr. London **102C,** 221 (1955).

[14] John H. Park, A fifty-fold momentary beam intensification for a high-voltage cold-cathode oscillograph, J. Research NBS **47,** 87 (1951) RP2231.

[15] G. H. Johnson, An impulse generator circuit for chopped-wave tests on transformers, Trans. AIEE **72,** 839 (1953).

[16] F. M. Bruce, High-voltage spark discharge, Endeavour **XIII,** No. 50, 61 (Apr. 1954).

[17] F. W. Peek, Dielectric phenomena in high-voltage engineering, p. 30 (McGraw-Hill Book Co., New York N. Y., 1915).

Journal of Research of the National Bureau of Standards Vol. 56, No. 4, April 1956 Research Paper 2670

Index of Refraction and Particle Size as Factors in the Infrared Spectrophotometry of Polyvinyl Chloride

Mary Reiney Harvey, James E. Stewart, and Bernard G. Achhammer

The scope of solid-phase infrared spectroscopy is broadened by the elimination of particle size restrictions heretofore placed on the sample. This applies only, however, to samples whose indices of refraction change only slightly with change in wavelength and can be matched to the indices of refraction of the suspending medium.

The potassium bromide pellet technique has been applied to the infrared spectral measurement of relatively large, solid particles (up to 44 microns diameter) of polyvinyl chloride, thus providing a technique for obtaining the infrared spectrum of polyvinyl chloride without subjecting the polymer to degrading forces. A near-match in the indices of refraction of potassium bromide and polyvinyl chloride is apparently responsible for the well-resolved, scatter-free spectrum obtained. Other imbedding salts having different indices of refraction were used to demonstrate the necessity of matching the indices of refraction of medium and sample when the sample particles are relatively large. The measurement of potassium bromide pellets containing polyvinyl chloride of various particle sizes showed that even very large particles (up to 110 microns) will yield characteristic spectra when the indices of refraction of sample and medium are matched. Infrared spectra of nylon and paper fibers imbedded in potassium bromide were obtained; these spectra demonstrate the the feasibility of this method for use with other materials. Equipment developed to make suitable pellets is described.

1. Introduction

Solid-phase infrared spectral measurements have been the subject of wide interest in recent years. The potassium bromide pellet method developed independently by Sister Miriam Michael Stimson [1] [1] and U Schiedt [2] has received, in particular, widespread attention.[2] This paper describes a further development of this technique to render it applicable to samples of high polymers of relatively large particle size.

Most solid phase methods [3, 4, 5, 6, 7] require that the material being studied be soluble or of a very fine particle size (smaller than the wavelength of incident radiant energy), or the methods employ heat or grinding. Also, a solid piece might be molded, which would require heat and pressure when high polymers are under consideration. Polyvinyl chloride cannot be subjected to heat or grinding without degrading the polymer. In addition, it is not soluble in infrared transmitting solvents and the particle size cannot be reduced without concomitant breakdown of the polymer. As a result, the potassium bromide pellet method has been modified to allow the inclusion of relatively large solid particles of polyvinyl chloride. This adaptation is feasible due to the matching of the indices of refraction of the two materials.

2. Materials

The polyvinyl chloride sample used predominantly in this investigation and referred to as polymer 101 is a commercial polymer.[3] This polymer is a hard, horny, tough, and abrasion-resistant thermoplastic material. It has outstanding resistance to chemicals and oils.

It is a relatively insoluble substance, being soluble in only a few solvents. Solvents include cyclohexanone, tetrahydrofuran, dimethyl formamide, and mixtures of tetrahydrofuran, methyl ethyl ketone, and toluene. Thin films were cast from a solution of the polymer in cyclohexanone, but their infrared spectra indicated that appreciable solvent was retained. In addition, both cyclohexanone and tetrahydrofuran tend to form peroxides in the presence of air [8], making their use as a solvent even more undesirable. Dimethyl formamide has a boiling point in the range of that of cyclohexanone and, therefore, would probably also be retained by a film cast from a solution composed primarily of dimethyl formamide.

The particle size of the bulk powder was examined. A small portion passed the U. S. Standard No. 325 sieve, which has a nominal opening of 44 μ. Increasingly larger amounts were collected by wet-sieving through coarser sieves of the series; the greatest fraction consisted of particles passing sieve No. 120 and retained on No. 170, that is, having a nominal diameter between 88 and 125 μ. There was very little powder retained on sieve No. 120. The Roller analyzer [9] was employed in an attempt to fractionate the powder that passed the No. 325 sieve. When the analyzer was set to collect particles of 0 to 10 μ size, no powder was obtained. Microscopic examination revealed the presence of a very small proportion of particles approximately 10 μ in diameter and very few particles smaller than that. Therefore, it was impossible to collect a sample of fine particle size fulfilling the heretofore established requirement for solid phase spectroscopy, namely, that the particles be smaller than the wavelength of incident radiant energy in order to minimize scatter.

[1] Figures in brackets indicate the literature references at the end of this paper.
[2] A session of the 1954 Pittsburgh Conference on Analytical Chemistry and Applied Spectroscopy was devoted to discussion of the potassium bromide pellet technique. The work described in this report was partially presented in a brief discussion at that time.
[3] Geon 101, kindly supplied by the B. F. Goodrich Chemical Co.

The smallest particle size fraction of the bulk powder most easily obtainable for study was that passing the No. 325 sieve. This fraction will henceforth be designated as 325-mesh powder (less than 44-μ particles). Photomicrographs [4] of this fraction, figure 1, show that on the average the particles approximate spheres and their surfaces appear to have cusps and valleys.

Several unsuccessful attempts were made to produce a satisfactory powder of finer particle size. The mineral oil mull technique was employed and the resulting infrared spectrum, which was published in 1952 [10], exhibited evidences of degradation, showing absorption bands at 3 and 6 μ and a broad, intense band from 8.4 to 12 μ. This degradation was the result of the prolonged mulling required to produce the requisite particle size, due to the hardness of the polymer. As mulling proved to be an unsatisfactory method of reducing particle size, grinding the sample in a cooled, vibratory ball mill [11] was attempted. The powder obtained, however, was discolored and its infrared spectrum contained extraneous absorption bands. Figure 2 is a photomicrograph of the powder that was subjected to 3 hours' ball milling. The appearance of the particles is changed considerably by this treatment.

Another polyvinyl chloride sample, polymer 121,[5] was measured in the infrared to determine the influence of particle size on the spectrum. Polymer 121,

[4] Photomicrographs were obtained by Sanford B. Newman of the Bureau.
[5] Geon 121, kindly supplied by the B. F. Goodrich Chemical Co.

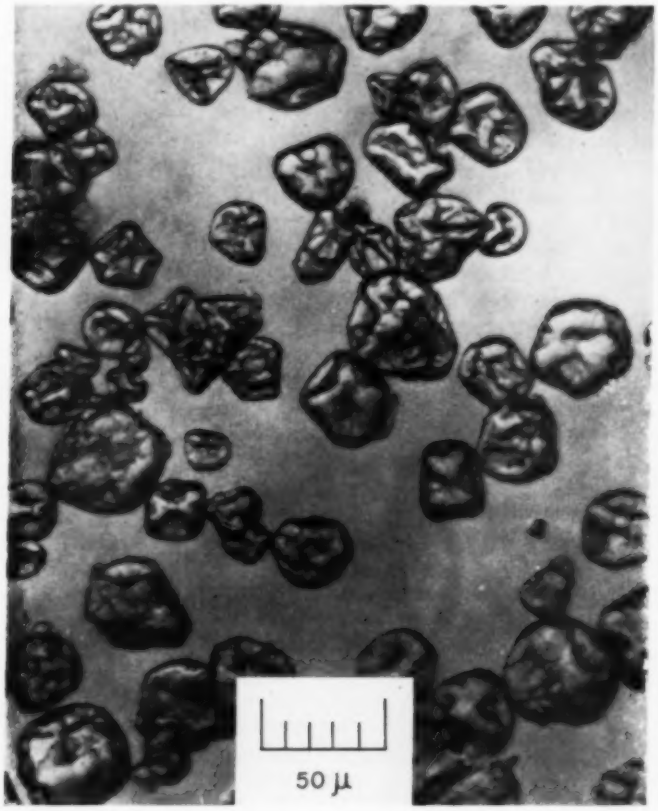

FIGURE 1. *Photomicrograph of 325-mesh polyvinyl chloride.*

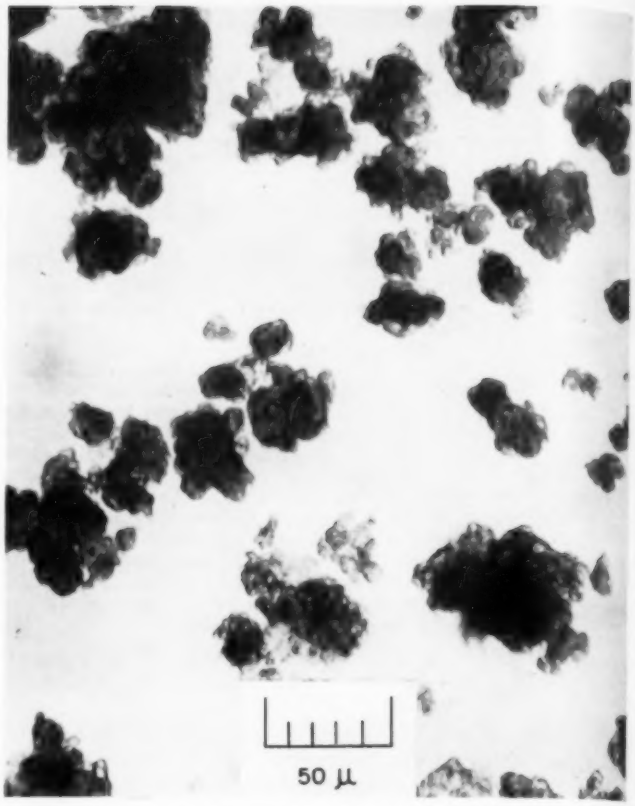

FIGURE 2. *Photomicrograph of ball-milled polyvinyl chloride.*

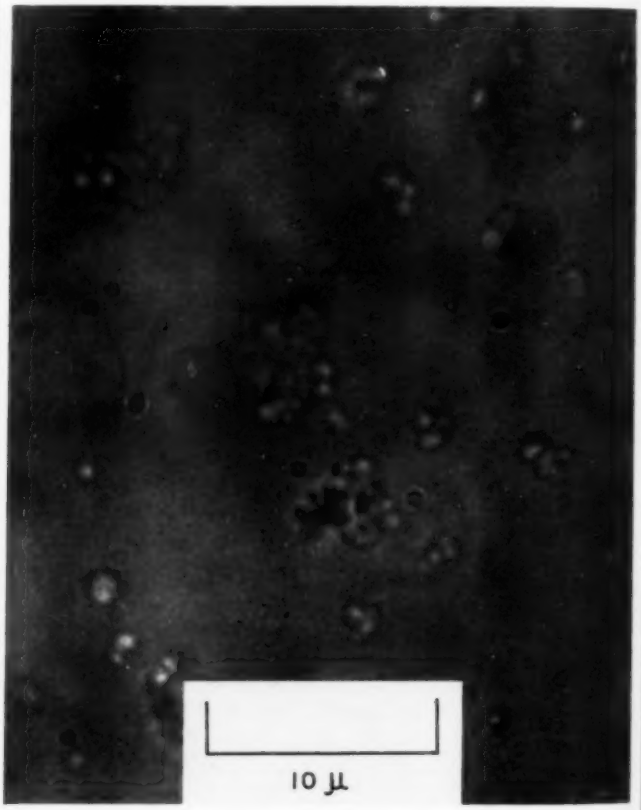

FIGURE 3. *Photomicrograph of 1- to 3-μ polyvinyl chloride.*

a paste resin, is a fine white powder of approximately 1- to 3-μ particle size. Figure 3 is a photomicrograph of this powder.

3. Suspension of Solids in Liquids

Because of the deleterious effects of grinding the polymer, a method to obtain an infrared spectrum of polyvinyl chloride in the undegraded state was sought.

The 325-mesh polymer was mixed (not mulled) in mineral oil. The infrared spectrum of the resulting paste was quite good except in the range from 2 to 6 μ where the radiation was badly scattered.

It was found that if, instead of mineral oil, a liquid was used for the mixing whose index of refraction more nearly matched that of the polymer, the scattering of the radiation could be eliminated.

The index of refraction of polymer 101 was measured in white light by grain immersion methods, using oils standardized in sodium light, and was found to be 1.548 at 27° C. The oils used in the measurement are prepared by mixing various proportions of mineral oil whose index is 1.46 n_D^{20} and α-monobromonaphthalene whose index is 1.66 n_D^{20}. When the powder is observed in the liquid mixture of matching index of refraction, it is almost invisible. When the index of refraction of the liquid mixture differs appreciably from that of the powder, the powder is clearly discernible. An example of this latter situation is shown in figure 1 where the powder is seen against a background of mineral oil.

When the 1.54 and 1.56 n_D^{20} liquid mixtures were used with the 325-mesh polymer to obtain pastes suitable for infrared measurement, the resulting spectra showed the complete elimination of the scattering of the wavelengths from 2 to 15 μ. A spectrum obtained on a mix of powder and the 1.56 n_D^{20} liquid was also published in 1952 [10].

Apparently, only a near-match of indices is necessary to eliminate scatter, but an appreciable difference will not be tolerated. The 1.61 n_D^{20} immersion liquid was too poor a match for the powder and again scattering occurred. When perfluorokerosene (1.32 n_D^{20}), which has no absorption bands from 2 to approximately 7.3 μ with the exception of a weak band at 4.2 μ, was used as the immersion liquid, scatter was extreme and there was not even an indication that there were bands in polyvinyl chloride around 3.4 and 7 μ.

α-Monobromonaphthalene, however, has considerably more absorption bands in the infrared than does mineral oil. When the 325-mesh powder is suspended in the 1.56 n_D^{20} liquid and placed in a rock salt cell of minimum thickness, the infrared spectrum contains α-monobromonaphthalene bands of appreciable intensity. Consequently, compensation must be made for the liquid in order to obtain the spectrum of the polymer. It is possible to achieve good compensation except in the regions where the liquid absorbs intensely, such as the 3.5- and the 12.5- to 13.5-μ regions. Here, inversion of the absorption bands of the liquid or other odd tracings may result [12].

Hexachlorobutadiene, with an index of refraction of 1.5542 n_D^{20}, proved to be an excellent suspending liquid for the 2- to 6-μ region, where it exhibits no absorption. Beyond 6 μ, however, several intense absorption bands are present which mar its usefulness. Hence, no single liquid suitable as a medium for the whole region from 2 to 15 μ was found.

4. Suspension of Solids in Solids

The requirements of a satisfactory suspending medium for relatively large particles are: (1) The substance should be of nearly matching index of refraction, and (2) the substance should exhibit negligible absorption bands in the infrared region. A substance that fulfills the second requirement is potassium bromide. Potassium bromide has an index of refraction of 1.56 n_D^{20} and thus fulfills the first requirement as far as polyvinyl chloride is concerned. Potassium bromide, therefore, should be well suited for use with polyvinyl chloride and this was found to be the case.

The potassium bromide pellet technique [1,2] was employed with several modifications of the method being made. It was desired to incorporate the 325-mesh polymer particles in the potassium bromide without subjecting them to grinding. An intimate admixture of the two powders is required as each particle of polymer powder must be surrounded by potassium bromide so that upon application of pressure the potassium bromide will flow into the "pockets" of the polymer particles. In this way, a pellet with a homogeneous index of refraction is produced. Sufficient admixture was obtained when the polymer and potassium bromide powders were thoroughly stirred together with a spatula.

To obtain a spectrum with absorption bands of appreciable intensity, it was found in the case of polyvinyl chloride that a considerable quantity of sample was required. Pellets were prepared successfully in the $\frac{7}{8}$-in. diameter dies using 2 percent polymer; i. e., 0.028 g of polyvinyl chloride and 1.4 g of potassium bromide. The resulting pellets were 0.05 in. thick.

4.1. Method and Equipment

To prepare a satisfactory pellet with this quantity of material, all conditions must be carefully controlled. Fisher's C. P. grade potassium bromide is ground in an agate mortar and sieved through a 150-mesh sieve.[5] Portions of 1.4 g are weighed into small aluminum cups and dried at 105° C for 100 hr in an air oven. Polymer portions of 0.028 g are weighed into smaller aluminum cups and desiccated. First, an approximately 50:50 potassium bromide-polymer mixture is obtained by transferring some of a potassium bromide portion to a cup containing polymer and thoroughly mixing the two powders with a spatula. Then this 50:50 mixture is diluted by the bulk of the potassium bromide to yield a 2:100 polymer-potassium bromide mix-

[5] Since this writing, the Harshaw Chemical Co. has marketed 325-mesh potassium bromide of optical quality which is currently being used for the preparation of pellets in this laboratory.

ture. This mixing process is carried out in a dry box at less than 3-percent relative humidity [7] as is the transfer of the powder mixture to the mold unit, parts a and b of figure 4. Before adding the top plunger, the mold unit is tapped to settle the powder evenly over the surface of the lower plunger. A small rubber band is placed around the top plunger to suspend it above the powder and also above the vacuum outlet of the chase, b. The mold unit is removed from the dry box, placed on a hardened steel disk, c, on the press platen, surrounded by a rubber wall, d, which also has a vacuum outlet, and topped by another hardened steel disk, e. A seal is formed between the disks and the rubber wall by the application of a 200-lb load and a vacuum; the assembly at this stage is shown in figure 5, A. When a vacuum of approximately 40 μ Hg is obtained, the load is applied slowly until a maximum pressure of approximately 95,000 psi is attained. The mold assembly under load is depicted in figure 5, B. The final pressure is held for 7 min and then slowly released. After release of the vacuum, the assembly can be separated and the pellet ejected from the mold unit by pressing the plungers and pellet out of the chase. A rod of smaller diameter than that of the plungers is used as an ejector and a cork-filled tube of diameter larger than that of the plungers as the receiving receptacle. This method of releasing the pellet without subjecting it to sudden changes in load prevents the formation of cracks in the pellet or of cleavage planes at its perimeter. Ejection of the pellet from the mold unit is depicted in figure 6. The pellet is immediately placed on removal in a desiccator, over silica gel, until the infrared spectrum is measured. Good pellets can be made without evacuating the powder but the results are not as reproducible. Pellets of potassium bromide alone (1.4 g) were made for use as reference pellets.

Extensive experimentation with an earlier mold and an available vacuum chamber [13] aided in the design of the present simple setup. The requirements are:

1. Two *hard* cylinders with all surfaces mirror polished and having plane-parallel ends;

2. A *hard* confining wall fitting these two rods snugly, provided with a vacuum outlet and with inner contacting wall mirror polished;

3. Two *hard* plane-parallel surfaces to protect the press platens;

4. A means of enclosing the parts of 1 and 2, utilizing the parts of 3 as the top and bottom, so that the whole unit is evacuable.

Hardened Stentor tool steel was used for the necessary parts satisfying the requirements of points 1, 2, and 3. To fulfill the fourth requirement, a wall was molded of natural rubber.[8] It afforded a simple means of providing for the considerable amount of vertical travel that is necessary when forming thick

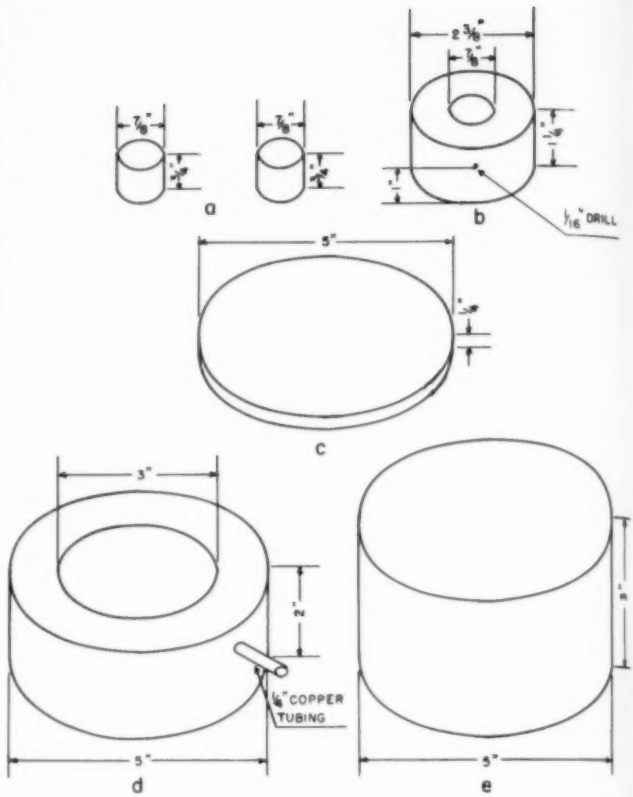

FIGURE 4. *Components of the vacuum mold used for making KBr pellets.*

a, Two steel plungers; b, enclosing steel chase; c, bottom steel disk; d, rubber wall; e, top steel disk.

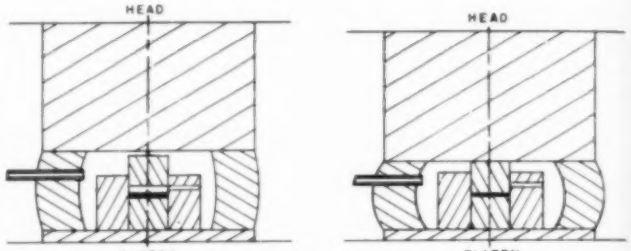

FIGURE 5. *Mold assembly.*

A, During evacuation; B, under load.

pellets. The wall thickness was 1 in. A hole was drilled through the wall and fitted with a brass tube as a vacuum outlet. The tube was sealed in the hole with a rubber adhesive. An improved design incorporates the vacuum outlet in the top steel disk and leaves the rubber wall as a solid piece.

A hydraulic testing machine capable of a maximum load of 60,000 lb is used to press the pellets. A stationary head is employed to insure application of the load perpendicular to the press platen because perfect alinement of all parts is essential at the high pressures used during pellet formation.

[7] At present, the relative humidity is approximately 1 percent as a result of improvements made in the dry box.

[8] The rubber was compounded with 10 parts of carbon black per 100 parts of rubber and cured for 1 hour. The product gave a Shore hardness value of 40. The wall was made in the Rubber Section of the Bureau.

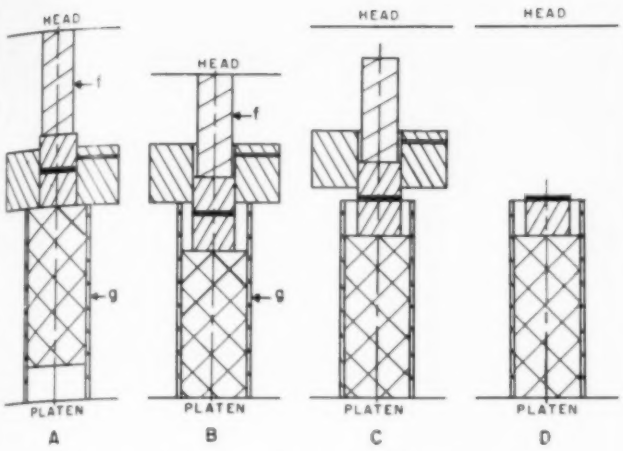

FIGURE 6. *Removal of a pellet from the mold.*

A, Setup for ejection, f, ejector rod, g, cork-filled ejector tube; B, pellet pressed free of chase; C, load released; D, pellet free.

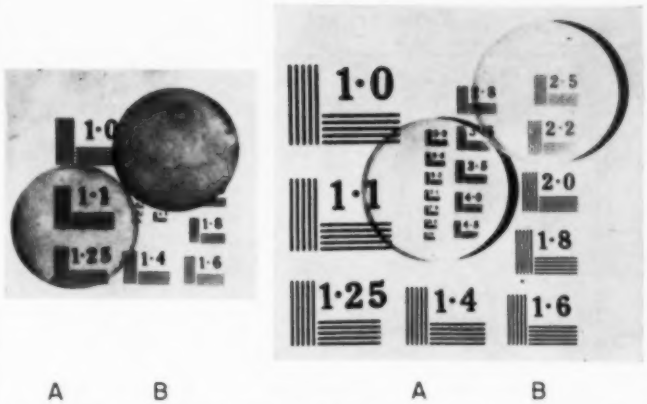

FIGURE 7. *Pellets simulating distance viewing* (left) *and contact viewing* (right).

A, KBr reference pellet; B, pellet of polyvinyl chloride in KBr.

A Perkin-Elmer model 21 double-beam infrared spectrophotometer with sodium chloride prism was used for measurements in the 2- to 15-μ region; in addition, some preliminary measurements were made with a cesium bromide prism in the Perkin-Elmer 21 in the spectral range from 15 to about 38 μ.

The pellets are larger than the infrared beam at the normal position of sample placement and therefore are merely placed in heavy paper holders fastened in place by two paper clips and the unit slipped into the cell mounts on the monochromator.

5. Results and Discussion

Potassium bromide pellets prepared with this equipment are transparent with the occasional exception of a cloudy edge, probably caused by a variation in level of the powder layer in the mold unit. When the 325-mesh polymer particles are incorporated in the potassium bromide, the pellets are still transparent enough to read print through them when they are laid upon the printed matter. If the printed matter is placed about 3 ft away, it can no longer be seen when viewed through the pellet (fig. 7). These pellets were made prior to the inclusion of the cork ejector in the pressing routine, hence a few cracks or strains may be noticed. Such slight imperfections can be tolerated becaue the pellets may be oriented in the holder in such a manner that the imperfections are not in the path of the infrared beam. This is possible because the pellets are $\frac{3}{8}$ in. in diameter and the beam is just less than $\frac{1}{4}$ by $\frac{3}{4}$ in. at the normal position of sample placement

5.1. Spectrum of Relatively Large Particles of Polyvinyl Chloride in Potassium Bromide and in Liquids

The infrared spectrum of the sample pellet just described, compensated by the reference pellet, is shown as the solid curve in figure 8. There is no evidence of scattered radiation and the complete 2- to 15-μ region is measurable. In fact, potassium bromide is usable in the infrared as far as approximately 38 μ. Figure 9 shows the spectrum of the same sample pellet and also of the potassium bromide reference pellet in the 15- to 38-μ region.

The other curves shown in figure 8 were obtained on mixtures of the 325-mesh polymer particles and various liquids; compensation for the liquid was made in each case. The use of these liquids was discussed previously. The noncompensable portions of the curves were deleted and the 1.56 n_D^{20} and 1.61 n_D^{20} liquid curves are not included beyond 6 μ in order to avoid confusion.

5.2. Spectrum of Potassium Bromide

The infrared spectrum of an 0.05-in. thick pellet of potassium bromide is shown as a dotted line in figure 10. There is evidence of a slight amount of impurity in the potassium bromide as indicated by the 3.42- and 7.22-μ bands. The absorption bands at 2.9 and 6.1 μ can probably be attributed to water. These bands could not be reduced by drying the potassium bromide for a longer time in an air oven. If the potassium bromide were not dried at all (a sample freshly removed from the reagent bottle, ground, and immediately pressed), the bands were not appreciably increased but the radiation was scattered from 2 to 6 μ and the pellet was translucent rather than transparent. The sample to be incorporated in the potassium bromide should also be dry or general scatter will result.

It is believed that the 2.9- and 6.1-μ bands cannot be attributed to potassium hydroxide because a pellet pressed from fine potassium bromide that was freeze-dried from deuterium oxide showed bands at 3.99 and 8.33 μ, which could be completely eliminated by subjecting the powder to vacuum drying at 125° C. However, evacuation alone would not accomplish this, and as the use of high temperature when the sample is involved is to be avoided, this method did not constitute an improved drying method.

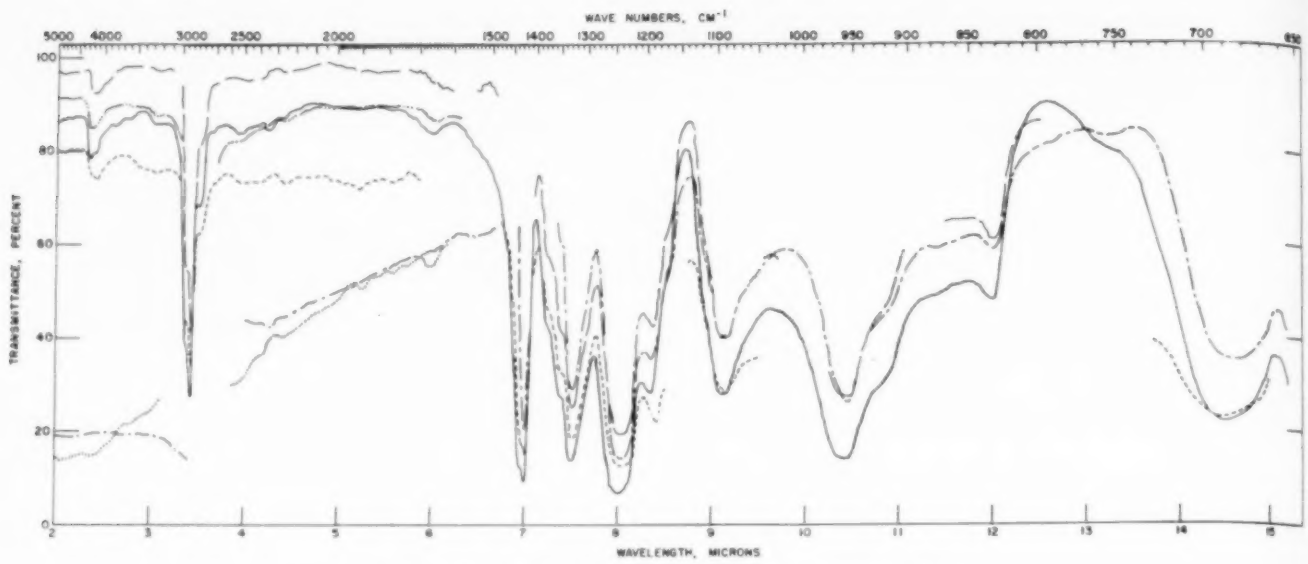

FIGURE 8. *Infrared spectra of polyvinyl chloride powder.*

Polymer particle size: <44 μ. In each case the polymer was mixed with the suspending medium and compensation for that medium was made.

Suspending medium: ————, KBr(1.56 n_D^{20}); — — — —, mineral oil(1.46 n_D^{20}); —— ——, bromobenzene(1.56 n_D^{20}); - - - - -, hexachlorobutadiene (1.55 n_D^{20}); —— · · ——, mineral oil and α-monobromonaphthalene(1.56 n_D^{20}); · · · · · · · · ·, mineral oil and α-monobromonaphthalene(1.61 n_D^{20}).

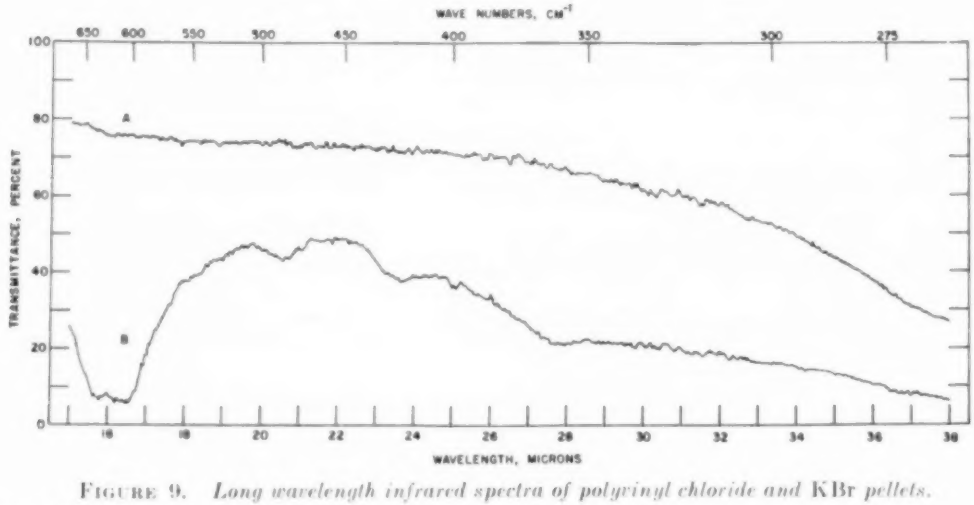

FIGURE 9. *Long wavelength infrared spectra of polyvinyl chloride and* KBr *pellets.*

A, 1.4 g KBr; B, 1.4 g KBr+0.028 g<44 μ particles of PVC.

The broad absorption bands centering around 6.95 and 8.8 μ are probably introduced during the grinding operation performed on the potassium bromide. In a series of experiments, a sample of potassium bromide was ground in a mullite mortar, pressed into a pellet, and the spectrum measured. The pellet was then reground in the mortar, repressed, and the spectrum measured. The whole process was repeated a third time. Each succeeding spectrum showed a band around 9.2 μ, of the same shape and of increased intensity after each grinding. This band, therefore, can be attributed to contamination of the potassium bromide resulting from abrasion of the mortar.

It was found that an agate mortar introduced less impurity than one of either mullite or alumina. It is possible that the agate mortar shows less tendency to abrade because its surface is highly polished. The spectrum shown in figure 10 is that of a pellet made from agate-ground potassium bromide.[9]

[9] The pellets that are currently being made in this laboratory with the 325-mesh optical quality Harshaw potassium bromide and prepared in the approximately 1-percent relative humidity dry box, show a much cleaner spectrum with such small absorption bands due to water that it is now not necessary to compensate for the potassium bromide.

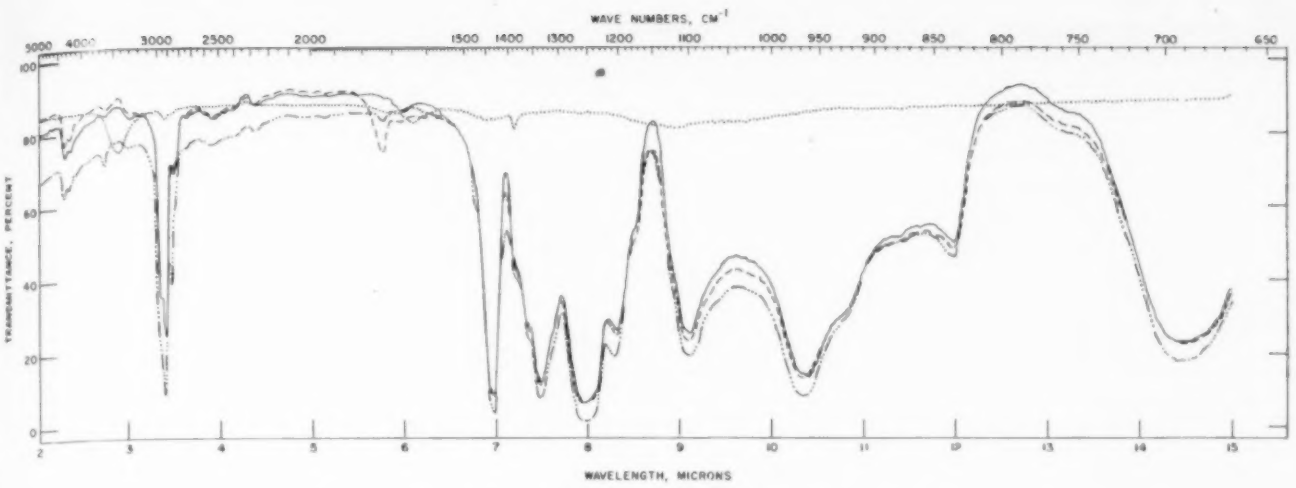

FIGURE 10. *Infrared spectra of polyvinyl chloride*-KBr *pellets.*

1.4 g KBr · · · · · · · · ·; 1.4 g KBr+0.028 g PVC compensated by 1.4 g KBr; untreated PVC (<44 μ particles) ————; ball-milled PVC– – – –; untreated PVC (1 to 3 μ particles) —— · · · ——.

5.3. Spectrum of Ball-Milled Polyvinyl Chloride in Potassium Bromide

The solid curve in figure 10 presents the compensated spectrum of a pellet containing untreated polymer 101 of relatively large particle size (polymer passing the 325-mesh sieve). The compensation of the potassium bromide is particularly noticeable in the water regions of 2.9 and 6.1 μ. This spectrum is presented here for comparison with that of polymer 101 subjected to 3 hours' ball milling prior to its incorporation in a pellet. The latter spectrum is shown in figure 10 as a dashed line which closely follows the solid line with the notable exception of the absorption band introduced at 5.78 μ. As was previously stated, the ball milling caused discoloration and changes in particle configuration. The presence of the 5.78-μ band constitutes further proof of the inadvisability of attempting comminution of the polymer in any way prior to measurement when a spectrum of the polymer in an undegraded state is desired.

5.4. Spectrum of Fine Particles of Polyvinyl Chloride in Potassium Bromide

Also shown in figure 10 is the spectrum of polymer 121, the paste resin composed of particles 1 to 3 μ in size (refer to fig. 3). The curve is similar to that representing the 325-mesh particles of polymer 101. Some differences in the two curves are probably due to the methods of preparing each polymer, e. g., the small bands present at 2.75 and 5.8 μ in the spectrum of Geon 121. The success in obtaining a spectrum of the relatively large particles so similar to the spectrum of very small particles is attributed to the apparent match in indices of refraction of the polymer and potassium bromide.

5.5. Index of Refraction Match of Polyvinyl Chloride and Potassium Bromide

The apparent match of indices of refraction of the polymer and potassium bromide was investigated. The indices of refraction of potassium bromide have been measured in the ultraviolet, visible, and/or infrared regions of the spectrum by several authors: Gyulai [14], Gundelach [15], Forrest [16], and Stephens, Plyler, Rodney, and Spindler [17]. However, the only reported measurements of the index of refraction of polyvinyl chloride were made in the visible. Schildknecht [18] reports a value of 1.54 for commercial unplasticized vinyl chloride resins and Fuoss [19] reports a value of 1.565 obtained at 40° C. The refractive index of polymer 101 was measured and found to be 1.548 at 27° C. This value nearly matches the 1.56 n_D of potassium bromide.

Methods for determining the infrared refractive indices of polyvinyl chloride were sought without much success. Determination by the prism method was not tried because it was felt that a prism of polyvinyl chloride will not be sufficiently transparent to infrared radiant energy. Efforts were made to calculate the index of refraction at 2 μ from the infrared spectrum of a thin film of the polymer. A film that exhibited interference fringes in the infrared spectrum between 2 and approximately 5 μ was selected. The index of refraction was calculated using the following equation:

$$n\lambda = 2t\eta \cos \theta,$$

where n=fringe number, λ=wavelength, t=thickness, η=index of refraction, and $\cos \theta$=cosine of the angle of incidence, taken to be 1. The thickness of the film, t, was determined by measuring the

distance between two flat calcium fluoride windows separated by a spacer of the film, following the method described by Smith and Miller [20]. A refractive index of 1.51 at 2 μ was calculated for the polymer by this method, which is admittedly subject to several errors.

The elimination of scattering of the infrared radiant energy when the polymer is pelleted with potassium bromide indicates that the infrared refractive indices of polyvinyl chloride, like the visible indices, approximate those of potassium bromide. In fact, the elimination of scatter appears to be a method for estimating the infrared indices of refraction of the polymer. Further study was undertaken to substantiate this method.

It is known that the presence of ultraviolet and visible electronic absorption bands in a material results in a characteristic variation of refractive index for wavelengths in the neighborhood and interior of the band. The shape of the resultant dispersion curve is described by Lorentz's equation. The large change in refractive index produces the phenomenon of Christiansen windows [21,22]. However, in the infrared spectral region absorption bands are associated with molecular vibrations. Not many dispersion curves have been determined for covalent compounds but from those available it is clear that, although some bands are associated with large refractive index changes, many bands affect dispersion slightly or not at all [23,24]. Price and Tetlow [22] have suggested the same conclusion from their observation of Christiansen windows in infrared spectra of mulled organic samples. Moreover, the appearance of the Christiansen filter effect in mulled organic samples has been noted in relatively few cases, and in fact, there was no indication of the presence of this effect when polyvinyl chloride was mixed with any of the various liquids mentioned in part 3. Hence, it might be hoped that the index of refraction of polyvinyl chloride will slowly decrease as longer wavelengths are approached, but that few large variations in the vicinity of absorption bands will be present.

Figure 11 presents the refractive indices of various salt crystals for the visible and infrared region of the spectrum.[10] There is some change in the indices of these salts from the visible to 2 μ but little change from 2 μ through the infrared region of interest.

Figure 12 presents the infrared spectra obtained by measuring pellets of three of these salts, each containing 0.028 g of 325-mesh polymer 101; compensation was made for the salt in each case. When potassium bromide was used as the suspending medium, the spectrum was far superior. All sample pellets were of good quality and with compensation

[10] The plot is adapted from the data presented by Joos [25].

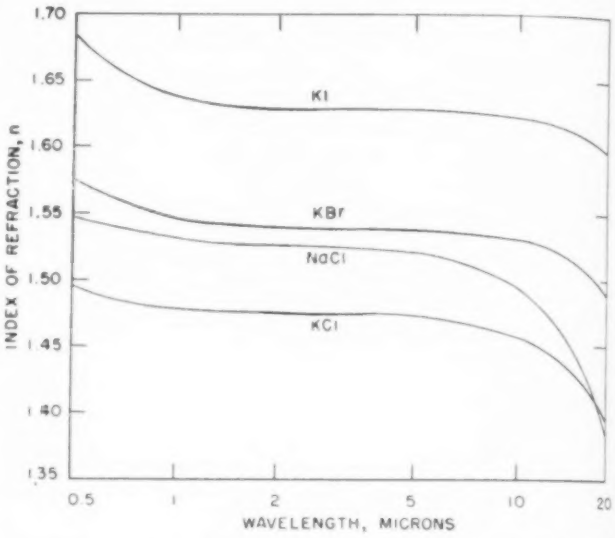

FIGURE 11. *Refractive indices of synthetic crystals.*

Adapted from data of G. Joos [25].

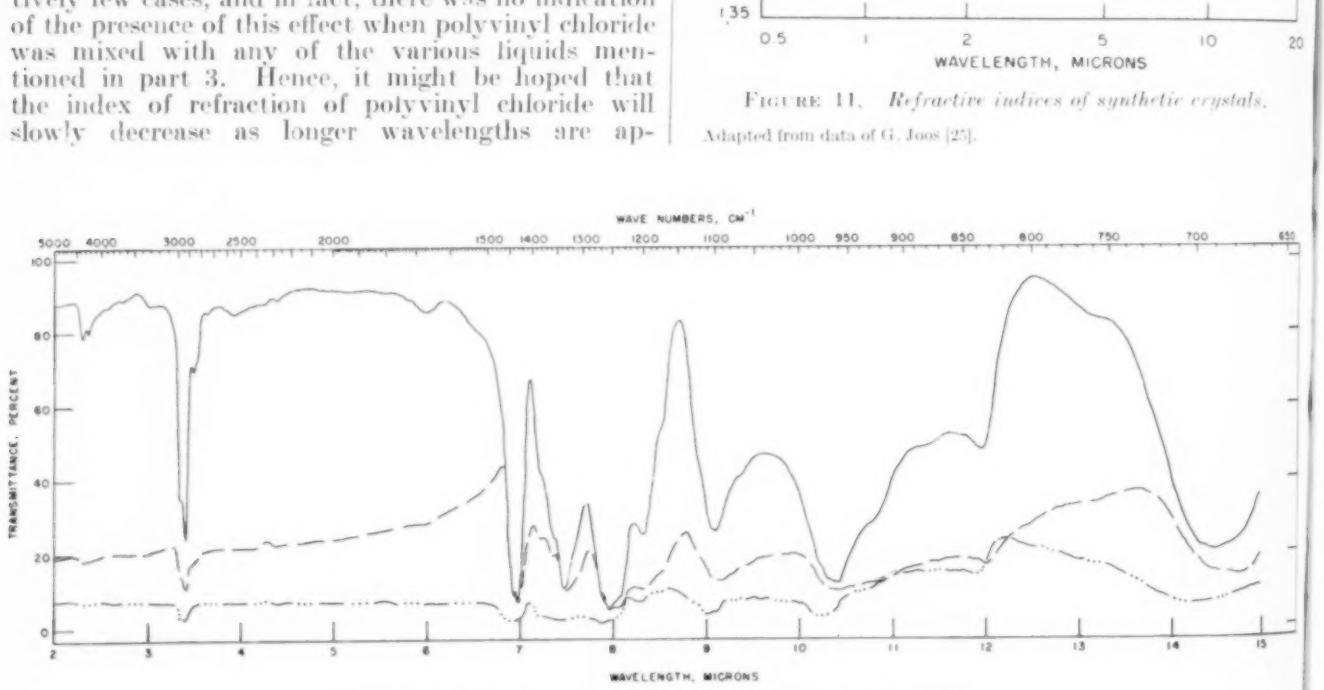

FIGURE 12. *Infrared spectra of polyvinyl chloride-salt pellets.*

Polymer particle size <44 μ. 1.4 g salt+0.028 g PVC compensated by 1.4 g salt; ————, PVC in KBr; — — —, PVC in KCl; — · — · —, PVC in

employed to eliminate impurities of the individual salts, spectra of equal quality should have been obtained if it were not a necessity to achieve a match of indices of refraction between relatively large sample particles and suspending medium. It is to be noted that although general scatter is extreme for the potassium chloride pellet, only the polymer band at 7 μ shows a Christiansen effect. This is evidence that most polyvinyl chloride absorption bands do not have rapidly changing refractive indices. The potassium bromide pellet does not show a Christiansen window even at 7 μ.

5.6. Necessity of Matching Indices of Refraction of Medium and Sample When the Sample Particles Are Relatively Large

A series of pellets was prepared using potassium chloride as the imbedding salt or matrix and incorporating other salts (potassium bromide, potassium iodide, and sodium chloride) with a range of refractive indices in order to demonstrate the necessity for matching indices of refraction of a sample with its imbedding medium. The samples of the salts to be incorporated in the potassium chloride were selected so that the particles were relatively large (325 mesh). None of these salts absorbs in the 2- to 15-μ infrared region to an appreciable extent. Thus, each pellet of the series is composed of two transparent materials and should yield a transparent pellet unless the mismatch in their indices of refraction causes scattering. Scattering does result in each case and increases with mismatch of the index of refraction of the sample salt and that of the potassium chloride. The uncompensated spectra of these mixed-salt pellets are shown in figure 13. The spectrum of sodium chloride in potassium chloride shows less scatter at the longer wavelengths where the index of refraction curves for these two salts are approaching each other (see fig. 11). It is, therefore, apparent that relatively large, solid particles can only be measured in the infrared when they are imbedded in a substance of nearly matching indices of refraction; otherwise, scattering of the radiant energy will result and obscure the spectrum.

5.7. Effect of Sample Particle Size When the Indices of Refraction of Sample and Medium Are Matched

To determine the effect of particle size on the infrared spectrum when the indices of refraction of sample and matrix are nearly matched, another series of pellets was prepared. Polyvinyl chloride was used as the sample and potassium bromide was selected as the imbedding salt as it was shown to afford the best match in indices of refraction with the polymer (see fig. 12). Figure 14 presents the compensated spectra of five pellets of polyvinyl chloride. The same weight of polymer, 0.028 g, was pelleted in each case. The dotted curve was obtained with polymer 121 and all others with polymer 101. It is of interest to observe that only the smallest particles display evidence of scatter at short wavelengths. It is known that scatter is maximum for particle diameters about equal to twice the wavelength, but for larger particles scatter varies from about half to about three-fourths of the maximum value [26]. The only significant change in the spectrum as the particle size is decreased appears to be the increase in intensity of the absorption bands.

Figure 15 shows a plot of the strong polyvinyl chloride band at 8 μ as a function of predominant particle size. The experimental points were obtained from the data shown in figure 14, and the solid line is a theoretical curve [12] for this band based on an absorption coefficient of 1,000 cm^{-1} as estimated from a spectrum of polymer 101 film. Calculations were made under the assumption of zero scatter and uniform particle size. The agreement is satisfactory.

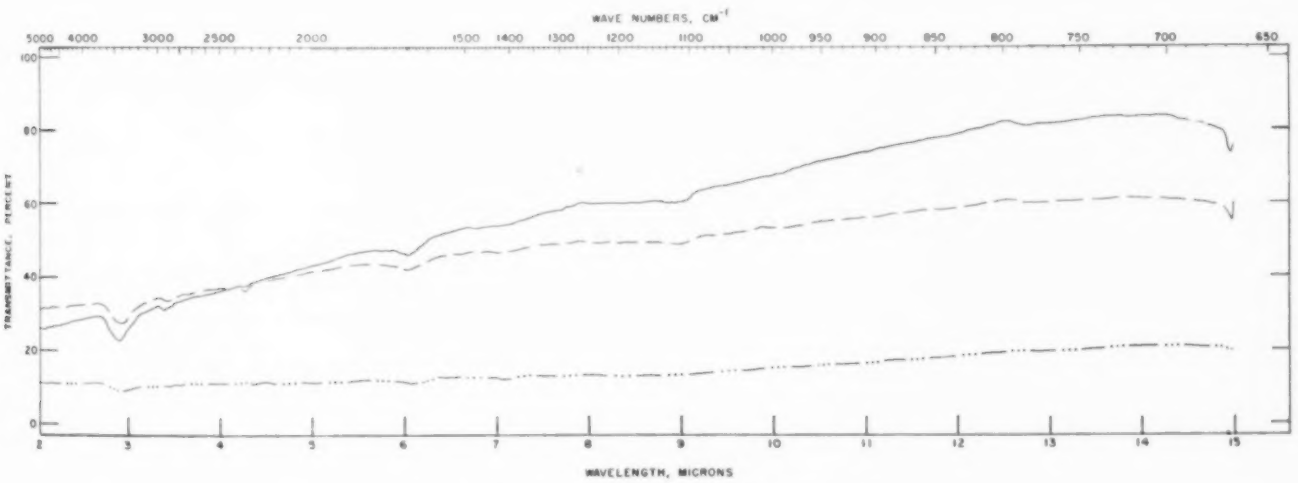

FIGURE 13. *Infrared spectra of salt-*KCl *pellets.*

Sample salt particle size <44 μ. 1.4 g KCl+0.028 g sample salt: ————, NaCl in KCl; - - - -, KBr in KCl; — · — · —, KI in KCl.

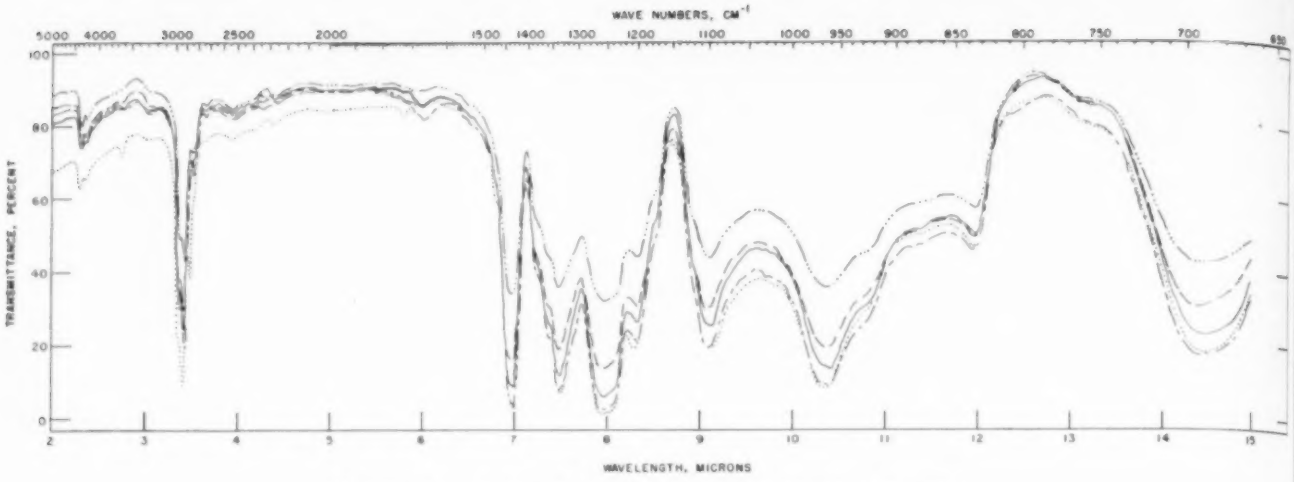

FIGURE 14. *Infrared spectra of polyvinyl chloride*-KBr *pellets.*

1.4 g KBr+0.028 g PVC compensated by 1.4 g KBr; predominant diameter of polymer particles: ——·——, 110 μ; — — —, 70 μ; ————, 30 μ; ——·——, 15 μ; · · · · · · · · · · · ·, 1 to 3 μ.

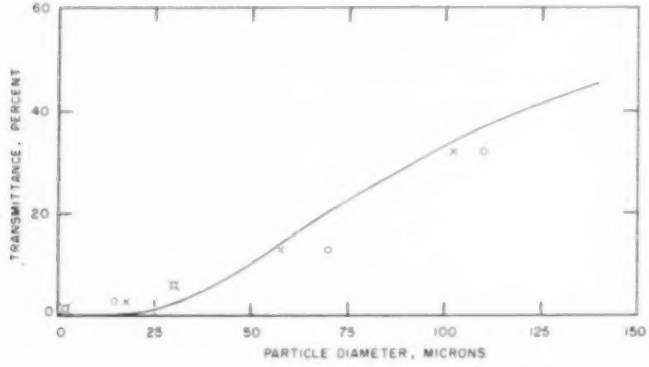

FIGURE 15. *Influence of particle size on the polyvinyl chloride band at 8 microns.*

1.4 g KBr+0.028 g PVC pellet. ○, Predominant particle size; ×, median of particle size; ————, theoretical relationship between particle size and transmission.

5.8. Spectral Measurements of Paper and Nylon Fibers

Because very large particles can be measured to obtain a credible spectrum, it should be possible to measure fibers of appreciable diameter or other solid substances that cannot be reduced to a fine particle size. For example, pellets of nylon fibers and of paper fibers were prepared, both using potassium bromide as the suspending medium; the choice of matrix was indicated by their indices of refraction in the visible. Figure 16, curve A, shows the compensated spectrum of pelleted paper fibers, which had been ground in a Kerner mill. The fibers are approximately 5 to 30 μ in diameter with the average diameter being about 10 μ; the length of the fibers is of the order of 400 μ. Curve B of this figure shows the compensated spectrum of pelleted nylon fibers, approximately 30 μ in diameter and microtomed in approximately 30-μ lengths.

The spectra of these two pelleted fibers are characteristic of spectra of their polymers and are identifiable as such.

6. Conclusion

The scope of solid phase infrared spectrocopy is broadened by the elimination of particle size restrictions heretofore placed on the sample. This applies only, however, to samples whose indices of refraction change only slightly with change in wavelength and can be matched to the indices of refraction of the suspending medium. The salts mentioned cover quite a range of refractive indices; when other crystals and numerous liquids that have infrared "windows" are taken into account, this range may be appreciably extended.

The authors express their appreciation to Francis A. Smith, Charles F. Bersch, and Walter K. Stone for valuable discussions and assistance during the conduct of the work, and to Harriet A. Baker and Margaret F. Toompas for preparation of the figures.

7. References

[1] M. M. Stimson and M. J. O'Donnell, The infrared and ultraviolet absorption spectra of cytosine and isocytosine in the solid state, J. Am. Chem. Soc. **74,** 1805 (1952).

[2] U. Schiedt and H. Reinwein, On the infrared spectroscopy of amino acids. I. A new preparation technique for infrared spectroscopy of amino acids and other polar compounds, Z. Naturforsch. [B] **7,** 270 (1952). U. Schiedt, H. An improvement on a preparation technique for the infrared photometric determination of amino acids and other polar compounds, ibid. [B] **8,** 66 (1953). See also U. Schiedt (reported by H. Hausdorff), German technique for presset potassium bromide infrared sampling, Appl. Spectroscopy **7,** 75 (1953).

[3] J. M. Hunt, M. P. Wisherd, and L. C. Bonham, Infrared absorption spectra of minerals and other inorganic compounds, Anal. Chem. 22 1478 (1950).

[4] M. Dolinsky, A technique for infrared analysis of solids insoluble in nonpolar solvents, J. Assoc. Offic. Agr. Chemists **34,** 748 (1951).

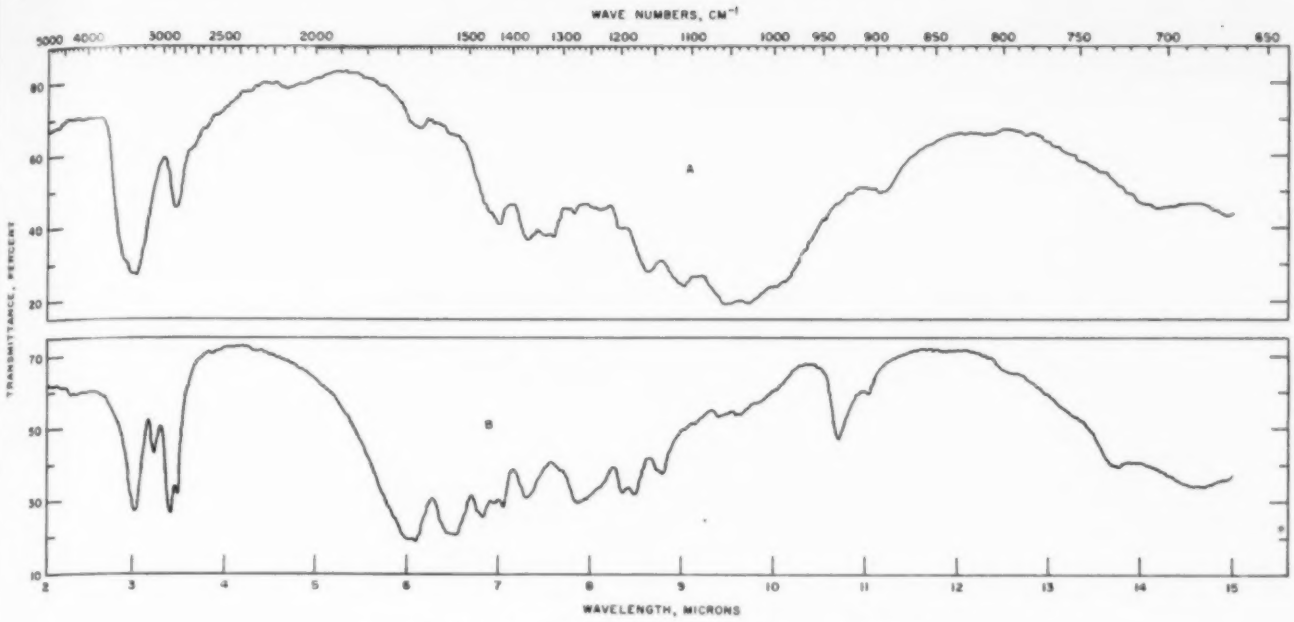

FIGURE 16. *Infrared spectra of fibers pelleted in* KBr.

A, 1.4 g KBr + 0.0050 g paper compensated by 1.4 g KBr; B, 1.4 g KBr + 0.0085 g nylon compensated by 1.4 g KBr.

[5] J. E. Tyler and S. A. Ehrhardt, Infrared spectra of evaporated films, Anal. Chem. **25,** 390 (1953).

[6] J. D. Sands and G. S. Turner, New developments in solid phase spectroscopy of elastomers and plastomers, Anal. Chem. **24,** 791 (1952).

[7] J. Lecomte, Studies in infrared spectra, Proc. Intern. Congr. Pure and Appl. Chem. 11th, London, **I,** 509 (1947).

[8] D. L. C. Jackson, Degradation of vinylidene chloride copolymers in solution, J. Soc. Chem. Ind., Trans. (London) **68,** 247 (1949).

[9] P. S. Roller, Separation and size distribution of microscopic particles—an air analyzer for fine powders, U. S. Bureau of Mines Tech. Paper No. 490 (1931).

[10] B. G. Achhammer, Polymer degradation studies by absorption and mass spectrometry, Anal. Chem. **24,** 1925 (1952).

[11] F. H. Forziati, W. K. Stone, J. W. Rowen, and W. D. Appel, Cotton powder for infrared transmission measurements, J. Research NBS **45,** 109 (1950) RP2116.

[12] J. E. Stewart, Absorption of radiant energy by solid particles in suspension, J. Research NBS **54,** 41 (1955) RP2563.

[13] L. A. Wood, N. Bekkedahl, and F. L. Roth, Measurement of densities of synthetic rubbers, J. Research NBS **29,** 391 (1942) RP1507; Ind. Eng. Chem. **34,** 1291 (1942).

[14] Z. Gyulai, The dispersion in the ultra-violet of a few alkali halides, Z. Physik **46,** 80 (1927).

[15] E. Gundelach, The dispersion of potassium bromide crystals in the infra-red Z. Physik **66,** 775 (1930).

[16] J. W. Forrest, Refractive index values for potassium bromide, J. Opt. Soc. Amer. **32,** 382 (1942).

[17] R. E. Stephens, E. K. Plyler, W. S. Rodney, and R. J. Spirdler, Refractive index of potassium bromide for infrared radiant energy, J. Opt. Soc. Amer. **43,** 110 (1953).

[18] C. E. Schildknecht, Vinyl and Related Polymers, p. 429 (John Wiley & Sons, Inc., New York, N. Y., 1952).

[19] R. M. Fuoss, Electrical properties of solids. V. Their variation at 40° C with frequency and composition in the system polyvinyl chloride-tricresyl phosphate, J. Am. Chem. Soc. **61,** 2334 (1939).

[20] D. C. Smith and E. C. Miller, Infrared absorption cells and measurement of cell thickness, J. Opt. Soc. Amer. **34,** 130 (1944).

[21] R. B. Barnes and L. G. Bonner, The Christiansen filter effect in the infrared, Phys. Rev. **49,** 732 (1936).

[22] W. C. Price and K. S. Tetlow, Infra-red Christiansen filter effect in slurries of organic crystals, J. Chem. Phys. **16,** 1157 (1948).

[23] A. H. Pfund, The dispersion of CS_2 and CCl_4 in the infrared, J. Opt. Soc. Amer. **25,** 351 (1935).

[24] M. A. Pittman Infrared dispersion of $CHCl_3$ and $CHBr_3$, J. Opt. Soc. Amer. **29,** 358 (1939).

[25] G. Joos, Physics of Solids, Part II, p. 164 (Office of Military Government for Germany, Wiesbaden, Germany, 1948).

[26] B. Goldberg, New computation of the Mie scattering functions for spherical particles, J. Opt. Soc. Amer. **43,** 1221 (1953).

WASHINGTON, December 28, 1955.

Journal of Research of the National Bureau of Standards Vol. 56, No. 4, April 1956 Research Paper 2671

Radiation From a Vertical Antenna Over a Curved Stratified Ground

James R. Wait

The problem of a radial electric dipole outside a concentrically stratified spherical conductor, such as the earth, is formulated. The solution is facilitated by considering the analogous nonuniform transmission line for the radial modes. The general result is then transformed to a Watson-type residue or azimuthal mode series, which reduces to the well-known result for the homogeneous earth as a special case. Following a method introduced recently by Bremmer, the residue series is converted to an alternative expansion, which is more suitable at short distances. The leading term of this new expansion corresponds to the case of the transmitter and receiver over a plane stratified conducting earth.

1. Introduction

In an earlier paper by the author [1] [1] expressions were derived for the fields of a vertical electric dipole over a plane stratified ground. In a further paper [2], the solution was extended to arbitrary antenna heights and numerical values of the attenuation factor were given. In the latter paper it was mentioned that the effect of the earth's curvature could be accounted for. It is the purpose of this paper to develop the theory for propagation over a curved earth with concentric stratifications.

The method of solution is a direct extension of Watson's [3] method to obtain a solution for the electric dipole radiating over a homogeneous sphere. It therefore does not seem necessary to outline the steps in the derivation in detail. A particular novel feature of the formulation, however, is that the boundary conditions at the surface of the sphere are specified by a surface impedance. The final expressions for the fields are then also applicable to propagation over other modified surfaces, such as a sphere with azimuthal periodic corrugations. Using a method suggested recently by H. Bremmer,[2] an expression for the field is then obtained that is very suitable for computation when the receiver is near the optical horizon. Finally, some numerical results are presented for various frequencies employing typical values of the ground constants over both a homogeneous and stratified earth.

2. Formal Solution

The source of the field is considered to be an electric current element Ids oriented in the radial direction to the spherical earth of radius a_1. Choosing a spherical coordinate system (r,θ,ϕ), the surface of the earth is then defined by $r=a_1$, and the dipole or current element is located at $r=b$ and $\theta=0$. The fields can now be expressed in terms of a Hertz vector, which has only a radial component U, as follows:

$$\left.\begin{aligned} E_r &= k^2+\frac{\partial^2}{\partial r^2}(rU) \\ E_\theta &= \frac{1}{r}\frac{\partial^2}{\partial r\partial\theta}(rU) \\ H_\phi &= -i\epsilon\omega\frac{\partial U}{\partial\theta} \end{aligned}\right\} \text{ for } r>a_1, \tag{1}$$

where $k=2\pi/$free-space wavelength, and ϵ is the dielectric constant of free space, $(=8.854\times10^{-12})$, in mks units. A time factor $\exp(i\omega t)$ has been implied. The function U satisfies the equation

$$(\nabla^2+k^2)U=C\frac{\delta(r-b)\delta(\theta)}{2\pi r^2\sin\theta}, \tag{2}$$

where the δ's are the Dirac delta or impulse function. The factor $2\pi r^2\sin\theta$ is the Jacobian of the transformation from rectangular to spherical coordinates. The constant is chosen so that U has the proper singularity at the dipole, that is

$$U\to\frac{e^{-ikR}}{4\pi i\omega\epsilon R}Ids \text{ for } R\to0, \tag{3}$$

where $R=[r^2+b^2-2br\cos\theta]^{1/2}$, $\epsilon=8.854\times10^{-12}$, and therefore $C=(i/\omega\epsilon)Ids$.

The field U is now written as the sum of two parts U_e+U_s, where U_e has the proper dipole singularity at $R=0$, and U_s is finite at that point. As U_s is a solution of the homogeneous wave equation, it can be written in the form

$$U_s=\frac{ikC}{4\pi}\sum_{n=0}^{\infty}(2n+1)A_n h_n^{(2)}(kr)P_n(\cos\theta), \tag{4}$$

where $h_n^{(2)}(kr)$ is the spherical Hankel function of the second kind, which assures outgoing waves at infinity, and $P_n(\cos\theta)$ is the Legendre function. The corresponding representation for U_e is [4]

[1] Figures in brackets indicate the literature references at the end of this paper.
[2] Personal communication.

$$U_e=\frac{ikC}{8\pi}\sum_{n=0}^{\infty}(2n+1)h_n^{(1)}(kr)h_n^{(2)}(kb)P_n(\cos\theta)\quad\text{for}\quad r<b$$
$$=\frac{ikC}{8\pi}\sum_{n=0}^{\infty}(2n+1)h_n^{(2)}(kr)h_n^{(1)}(kb)P_n(\cos\theta)\quad\text{for}\quad r>b \tag{5}$$

The coefficients A_n are now found from the boundary condition, that

$$E_\theta=-ZH_\phi\quad\text{at}\quad r=a_1, \tag{6}$$

which can be rewritten

$$\left[\frac{1}{r}\frac{\partial}{\partial r}rU=Zi\epsilon\omega U\right]_{r=a_1}. \tag{7}$$

In other words, it is assumed that the surface of the earth exhibits the property of surface impedance. Z is taken to be equal to the ratio of the tangential electric and magnetic fields for a vertically polarized plane wave at grazing incidence on a plane stratified earth. This step in the analysis leads to a great simplification, and it is justified in the appendix. It then readily follows that

$$A_n=-\frac{h_n^{(1)}(ka_1)}{h_n^{(2)}(ka_1)}\left[\frac{\frac{1}{x}\frac{d}{dx}\log xh_n^{(1)}(x)-\frac{i\Delta}{x}}{\frac{1}{x}\frac{d}{dx}\log xh_n^{(2)}(x)-\frac{i\Delta}{x}}\right]_{x=ka_1}h_n^{(2)}(kb), \tag{8}$$

where $\Delta=\epsilon\omega Z/k=Z/120\pi$ and where $h_n^{(1)}(x)$ is the spherical Hankel function of the first kind. The total field is then of the form

$$U=\sum_{n=0}^{\infty}(2n+1)f(n)P_n(\cos\theta). \tag{9}$$

Following the process developed by Watson [3], the summation is transformed into the following contour integral:

$$I=i\int_{c_1+c_2}\frac{ndn}{\cos n\pi}f\left(n-\frac{1}{2}\right)P_{n-1/2}[\cos(\pi-\theta)], \tag{10}$$

where the contour c_1+c_2 encloses the positive real axis, as illustrated in figure 1. Noting that the poles of the integrand are located at $n=1/2, 3/2, 5/2, \ldots$, etc., it can be readily verified by the theorem of residues that this integral is equivalent to eq (9). Now, since $f(n-1/2)$ is an even function of n, the part of the contour c_1 above the real axis can be replaced by the contour c_1', which is located just below the negative real axis. The contour $c_1'+c_2$ is now entirely equivalent to L, a straight line running along just below the real axis. Replacing $n-1/2$ by ν, the contour representation for U takes the form

$$U=-i\int_L\frac{(\nu+1/2)}{\sin\nu\pi}f(\nu)P_\nu[\cos(\pi-\theta)]d\nu. \tag{11}$$

It is to be noted that this manipulation of the contours is simplified because $f(n-1/2)$ is an even function of n as a consequence of the method of formulation. In the usual treatment for the homogeneous sphere, $f(n-1/2)$ is not an even function of n, and the deformation of the contour becomes more intricate.

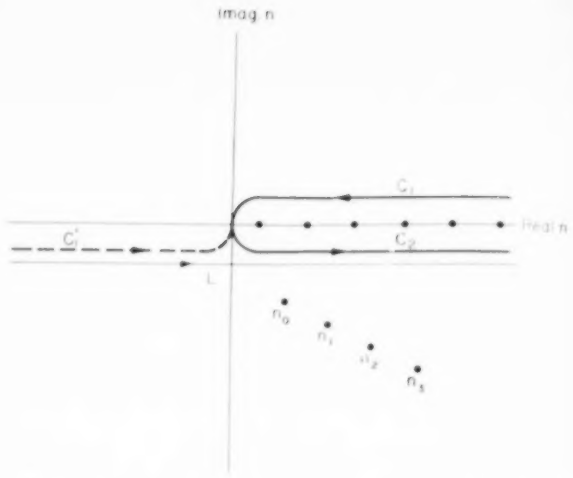

FIGURE 1. *Complex n plane showing the contours and the zeros of cos nπ and zeros of the denominator of equation* (8).

The next step in the analysis is to close L by an infinite semicircle in the negative half-plane. The contribution from this portion of the contour vanishes as the radius of the semicircle approaches infinity. The reasoning for this fact follows directly from Watson's argument for the homogeneous sphere. The value of the integral for U along the contour L is now equal to the sum of the residues of the integrand evaluated at the poles ν_s of $f(\nu)$ located in the lower half-plane. It then follows that U is proportional to

$$\sum_{s=0}^{\infty}\frac{(\nu_s+1/2)h_{\nu_s}^{(2)}(kb)h_{\nu_s}^{(2)}(kr)P_{\nu_s}[\cos(\pi-\theta)]}{\sin(\pi\nu_s)\left[\frac{\partial M(\nu)}{\partial\nu}\right]_{\nu=\nu_s}[h_{\nu_s}^{(2)}(ka_1)]^2} \tag{12}$$

where the function $M(\nu)$ is defined by

$$M(\nu)=\left[\frac{1}{x}\frac{d}{dx}\log xh_n^{(2)}(x)-i\frac{\Delta}{x}\right]_{x=ka_1} \tag{13}$$

and the poles ν_s are the solutions of $M(\nu)=0$. Again, as a result of the formulation, the equation here for the determination of the roots is relatively simple. Making the usual approximation [1] that $h_n^{(2)}(x)$ can be represented by Hankel functions of order 1/3, eq (13) can be replaced by

$$\delta e^{i\pi/3}\frac{H_{2/3}^{(2)}[(1/3)(-2\tau_s)^{3/2}]}{H_{1/3}^{(2)}[(1/3)(-2\tau_s)^{3/2}]}=-(-2\tau_s)^{-1/2}, \tag{14}$$

where

$$\delta=-i\frac{120\pi}{(ka_1)^{1/3}Z}\text{ and }\tau_s=\frac{\nu_s-ka_1}{(ka_1)^{1/3}}. \tag{15}$$

For a homogeneous earth whose propagation constant is γ_1, it follows that

$$Z=120\pi\frac{\gamma_0}{\gamma_1}\left[1-\frac{\gamma_0^2}{\gamma_1^2}\right]^{1/2}, \tag{16}$$

with $\gamma_0=ik$, and therefore

$$\delta=-\frac{i}{(ka_1)^{1/3}}\frac{\gamma_1^2/\gamma_0^2}{[(\gamma_1^2/\gamma_0^2)-1]^{1/2}}, \tag{17}$$

which is identical to the value given by Bremmer [4]. For a two-layer ground whose upper stratum of thickness l has propagation constant γ_1, the surface impedance Z is given by (see appendix)

$$Z=120\pi\frac{\gamma_0}{\gamma_1}\left[1-\frac{\gamma_0^2}{\gamma_1^2}\right]^{1/2}Q, \tag{18}$$

where

$$Q=\tanh[P+(\gamma_1^2-\gamma_0^2)^{1/2}l], \tag{19}$$

and

$$P=\tanh^{-1}\left[\frac{\gamma_1^2}{\gamma_2^2}\left(\frac{\gamma_2^2-\gamma_0^2}{\gamma_1^2-\gamma_0^2}\right)^{1/2}\right] \tag{20}$$

with γ_2 as the propagation constant of the lower medium. The correction factor Q, which approaches unity for $l\to\infty$, can be evaluated with the aid of charts of hyperbolic functions of complex argument. The expression for Q for a stratified ground for any number of layers has been given previously along with some numerical values for special cases [5].

Equation (12) for U can now be considerably simplified by replacing the Legendre function by its leading term in its asymptotic expansion and the functions $h_\nu^{(2)}(kb)$ and $h_\nu^{(2)}(kr)$ by their Hankel approximations to lead to

$$U=2U_0\sqrt{-2\pi iX}\sum_{s=0}^{\infty}f_s(h_1)f_s(h_2)\frac{e^{-i\tau_sX}}{2\tau_s-1/\delta^2} \tag{21}$$

with

$$f_s(h_i)=\left[\frac{X_i^2-2\tau_s}{-2\tau_s}\right]^{1/2}\frac{H_{1/3}^{(2)}[\frac{1}{3}(X_i^2-2\tau_s)^{3/2}]}{H_{1/3}^{(2)}[\frac{1}{3}(-2\tau_s)^{3/2}]} \tag{22}$$

and where

$$U_0=\frac{Ids e^{-ika_1\theta}}{4\pi i\omega\epsilon a_1\theta}, \qquad h_1=r-a_1,$$

$$h_2=b-a_1, \qquad X=(ka_1)^{1/3}\theta,$$

and

$$X_i=(ka_1)^{1/3}(2h_i/a_1)^{1/2} \quad \text{for} \quad i=1,2.$$

The preceding equations are identical in form to that obtained for the homogeneous earth as given by Watson [3], Bremmer [4], Friedman [6], and others. It is important to note that the quantities p, δ, and the roots τ_s are dependent on the electric constants and the nature of the stratification of the earth. Bremmer [4] has given very adequate formulas for τ_s in terms of powers of δ. These can be used directly for the stratified earth. They can also be used for a sphere with a corrugated surface if the appropriate value of the surface impedance is employed [7].

3. Modified Flat Earth Formula

The so-called residue series for U could be used for calculations for propagation over a curved earth. The series, however, converges poorly for distances near the optical horizon. It would be desirable to transform the residue series formula to a new type of expansion where the first term corresponds to the radiation of a dipole over a plane stratified earth. Succeeding terms would then be preferably in proportion to inverse powers of ka_1. In the limiting case when ka_1 tends to infinity, the expression U should correspond to the situation treated previously. A method of obtaining expansion formula of this type is mentioned briefly by Bremmer in his book [4]. Very recently he has described to the author an alternative procedure, which he illustrated for the case when the transmitter and receiver are located on the surface of a homogeneous spherical earth. His method will be employed here in the case when the transmitter and receiver are not both on the earth. Furthermore, as will be shown, the method also is applicable to stratified and corrugated surfaces. The first step is to express the field in terms of a contour integral as follows:

$$\frac{iU(\rho)}{2\rho^{1/2}U_0}=\frac{1}{2\pi i}\int_{c-i\infty}^{c+i\infty}\frac{\pi^{1/2}f(p,h_1)f(p,h_2)e^{p\rho}dp}{1+e^{i\pi/3}p^{1/2}A(p)}, \tag{23}$$

where $\rho=iX/2\delta^2$ and where $A(p)$ and $f(p,h)$ are chosen as follows:

$$A(p)=\frac{H_{2/3}^{(2)}\left(\frac{p^{3/2}}{3\delta^3}\right)}{H_{1/3}^{(2)}\left(\frac{p^{3/2}}{3\delta^3}\right)} \tag{24}$$

and

$$f(p,h_i)=\left[\frac{X_i^2+(p/\delta^2)}{(p/\delta^2)}\right]^{1/2}\frac{H_{1/3}^{(2)}[\frac{1}{3}(X_i^2+p/\delta^2)^{3/2}]}{H_{1/3}^{(2)}[\frac{1}{3}(p/\delta^2)^{3/2}]}, \tag{25}$$

for $i=1, 2$; and c is some positive constant.

It can be noted that the poles p_s of the integrand are determined by the solution of

$$H_{1/3}^{(2)}\left[\frac{p_s^{3/2}}{3\delta^3}\right]+e^{i\pi/3}p_s^{1/2}H_{2/3}^{(2)}\left[\frac{p_s^{3/2}}{3\delta^3}\right]=0. \tag{26}$$

If p_s is replaced by $2\delta^2\tau_s e^{i\pi}$ this equation is identical to eq (14) for the determination of the roots τ_s. It can be readily verified that the sum of the residues evaluated at the poles p_s leads back to eq (21).

Recognizing that the right-hand side of eq (23) is in the form of an inverse Laplace Transform, it can

be written in Heaviside's operational notation [8] as follows:

$$\frac{iU(\rho)\bar{1}}{2\rho^{1/2}I'_0}=F(p), \tag{27}$$

where

$$F(p)=\frac{\pi^{1/2}pf(p,h_1)f(p,h_2)}{1+e^{i\pi/3}p^{1/2}A(p)} \tag{28}$$

and

$$\bar{1}=\begin{cases}1 \text{ for } \rho>0\\ 0 \text{ for } \rho<0.\end{cases}$$

The technique is now to expand $F(p)$ in an asymptotic expansion in powers of $1/p$ and then to invert each term to obtain series expansion for ρ in powers of δ^3. It is convenient for the moment to consider $h_2=0$ so that $f(p,h_2)=1$. Each of the Hankel functions is now expanded in an asymptotic expansion, with due regard being paid to the phase of arguments. Note that

$$+\pi>\frac{3}{2}\arg.\ p_s-3\arg.\ \delta-3\pi>-2\pi,$$

which suggests replacing the arguments z by $ze^{-3i\pi}$ and then employing the relation

$$H_\nu^{(2)}(ze^{-3i\pi})=-\frac{\sin 2\pi\nu}{\sin \pi\nu}H_\nu^{(2)}(z). \tag{29}$$

On making this conversion, the validity of the asymptotic expansions is established. It then follows that

$$F(p)=\frac{\pi^{1/2}pf(p,h_1)}{1-ip^{1/2}\left[1+i\frac{\delta^3}{2p^{3/2}}+\frac{5}{8}\frac{\delta^6}{p^3}+\cdots\right]} \tag{30}$$

$$f(p,h_1)=e^{-(z_1-z_2)i}\left[1+\frac{\delta^2N_1^2}{p}\right]^{-1/4}\left\{1-i\frac{5}{72}\left[\frac{1}{z_2}-\frac{1}{z_1}\right]+\frac{335}{10368}\frac{1}{z_2^2}-\frac{385}{10368}\frac{1}{z_1^2}+\frac{25}{5184}\frac{1}{z_1z_2}\right\} \tag{31}$$

plus terms in $\frac{1}{z_1^3}$, etc., with

$$z_1=\frac{1}{3}\left[\frac{p}{\delta^2}\right]^{3/2}\left[1+\frac{N_1^2\delta^2}{p}\right]^{3/2}e^{-3i\pi}$$

and

$$z_2=\frac{1}{3}\left[\frac{p}{\delta^2}\right]^{3/2}e^{-3i\pi}.$$

To further simplify the above expression for $f(p,h_1)$, the factor $(1+N_1^2\delta^2/p)^{3/2}$ is expanded in a binominal series, and terms containing N_1^4, N_1^6, etc. are neglected. After some algebraic manipulation, it follows that

$$f(p,h_1)\simeq e^{-\alpha p^{1/2}}\left[1-\frac{i\alpha\delta^3}{2p}-\frac{5}{8}\frac{\alpha\delta^6}{p^{3/2}}\right] \tag{32}$$

plus terms containing $\alpha^2\delta^6$, $\alpha^3\delta^9$, etc., where $\alpha=kh_1\Delta$. When this formula for $f(p,h_1)$ is substituted into eq (30), it is readily shown that

$$\frac{F(p)}{i\pi^{1/2}}=-\frac{ipe^{-\alpha p^{1/2}}}{1-ip^{1/2}}+\delta^3\left[\frac{i}{2(1-ip^{1/2})^2}-\frac{\alpha}{2(1-ip^{1/2})}\right]e^{-\alpha p^{1/2}}+\delta^6\left[\frac{5}{8}\frac{1}{p^{3/2}(1-ip^{1/2})^2}-\frac{i}{4p(1-ip^{1/2})^3}+\frac{\alpha}{4p(1-ip^{1/2})^2}+\frac{5i\alpha}{8p^{3/2}(1-ip^{1/2})}\right]e^{-\alpha p^{1/2}} \tag{33}$$

plus terms containing δ^9, δ^{12}, etc.

The final step in the analysis is to find the corresponding functions of ρ for each term on the right-hand side of the above equation. The necessary operational pairs can be derived from the basic relation [9],

$$M(g,\rho)\bar{1}=\frac{e^{-\alpha p^{1/2}}}{1+gp^{1/2}}-1 \tag{34}$$

where

$$M(g,\rho)=erfc\left(\frac{\alpha}{2p^{1/2}}\right)-e^{\left(\frac{\alpha}{g}+\frac{\rho}{g^2}\right)}erfc\left(\frac{\alpha}{2\rho^{1/2}}+\frac{\rho^{1/2}}{g}\right)$$

with

$$erfc(z)=\frac{2}{\pi^{1/2}}\int_z^\infty e^{-x^2}dx.$$

For example,

$$\frac{e^{-\alpha p^{1/2}}}{(1-ip^{1/2})^2}=\left[g\frac{\partial}{\partial g}M(g,\rho)+M(g,\rho)\right]_{g=-i}1 \tag{35}$$

so that

$$\frac{i\pi^{1/2}e^{-\alpha p^{1/2}}}{(1-ip^{1/2})^2}=\left\{i\pi^{1/2}erfc\left[\frac{\alpha}{2\rho^{1/2}}\right]+2\rho^{1/2}e^{-\alpha^2/4\rho}-i\pi^{1/2}(1+2\rho-i\alpha)e^{-(\rho-i\alpha)}erfc\left[\frac{\alpha}{2\rho^{1/2}}+i\rho^{1/2}\right]\right\}\bar{1} \tag{36}$$

The other pairs can be derived in a similar manner by further differentiations with respect to the param-

eter g and then setting $g=-i$. The final result after collecting like terms is

$$\frac{U(\rho)}{2U_0}=e^{-\rho^2/4\rho}-i(\pi\rho)^{1/2}e^{-(\rho-i\alpha)}erfc\left[\frac{\alpha}{2\rho^{1/2}}+i\rho^{1/2}\right]$$

$$+\delta^3\rho^{1/2}\left[\rho^{1/2}e^{-\alpha^2/4\rho}-\frac{i\pi^{1/2}(1+2\rho)}{2}e^{-(\rho-i\alpha)}erfc\left(\frac{\alpha}{2\rho^{1/2}}+i\rho^{1/2}\right)\right.$$

$$\left.+\frac{i\pi^{1/2}}{2}(1+i\alpha)erfc\,\frac{\alpha}{2\rho^{1/2}}\right)\Bigg] \quad (37)$$

plus terms containing δ^6, δ^9, etc.

The coefficient of the δ^6 term is not written out here as it is quite cumbersome and in itself would not be suitable for computation. It is constructive at this stage to express $U(\rho)$ in terms of the parameter w defined by

$$w=\rho\left(1+\frac{h_1}{\Delta a_1\theta}\right)^2, \quad (38)$$

whence

$$\frac{U(\rho)}{2U_0}\simeq e^{-ikh_1^2/2a_1\theta}\left\{1-i(\pi\rho)^{1/2}e^{-w}erfc(iw^{1/2})\right.$$

$$+\delta^3\left[\rho-i(\pi\rho)^{1/2}\frac{(1+2\rho)}{2}e^{-w}erfc(iw^{1/2})\right]\Bigg\}$$

$$+\delta^3\left[\frac{i(\pi\rho)^{1/2}}{2}(1+ikh_1\Delta)erfc\left(\frac{-ikh_1^2}{2a_1\theta}\right)^{1/2}\right] \quad (39)$$

For the homogeneous earth, the factor $\Delta=(\gamma_0^2/\gamma_1^2)(\gamma_1^2/\gamma_0^2-1)^{1/2}$, and if a_1 the radius tends to infinity or $\delta=0$, the remaining first term corresponds to the well-known formula for the attenuation factor of a dipole over a flat earth [10]. ρ is then the numerical distance of Sommerfeld [11]. It is interesting to note that the form of the first term is identical to the result obtained by Hufford [12], using an integral-equation formulation. When the ground is stratified such that $\Delta=\epsilon\omega Z/k$, where Z is the surface impedance, the first term corresponds to the result obtained previously for the dipole over the plane stratified earth [1, 2].

It now appears that, for small heights such that $kh_1^2/2a\theta$ is small compared to one, the height gain function is simply $1+i\alpha$, which is a common factor of at least the first three terms in the expansion in powers of δ^3. To this approximation the final result is expressed conveniently as

$$\frac{U(\rho)}{2U_0}=W(\rho)=G\left\{F_0(\rho)-\frac{\delta^3}{2}[1-i(\pi\rho)^{1/2}-(1+2\rho)F_0(\rho)]\right.$$

$$\left.+\delta^6\left[1-i(\pi\rho)^{1/2}(1-\rho)-2\rho+\frac{5}{6}\rho^2+\left(\frac{\rho^2}{2}-1\right)F_0(\rho)\right]\cdots\right\}, \quad (40)$$

where

$$F_0(\rho)=1-i(\pi\rho)^{1/2}erfc(i\rho^{1/2})\,e^{-\rho}$$

$$G\simeq(1+i\alpha)(1+i\beta)\text{ with }\beta=kh_2\Delta.$$

At distances from the antenna greater than a few wavelengths the quantity $U(\rho)$ is proportional to the vertical component of the electric field, and correspondingly $2U_0$ is proportional to the field of an identical source over a flat perfectly conducting earth. The field strength E, in millivolts per meter, at a distance D_{km}, in kilometers, is then given by

$$E=\frac{300}{D_{km}}|W(\rho)| \quad (41)$$

for a dipole transmitter whose strength is such that it would radiate 1 kw over a perfectly conducting flat ground.

To illustrate the nature of the results, calculations are carried out for E as a function of D_{km} over a homogeneous spherical earth of radius 6,373 km at frequencies of 30, 150, and 750 Mc. These curves are illustrated in figure 2, where it is indicated that the relative dielectric constant of the ground is 4 and the conductivity is 10^{-2} mho/m. The flat-earth formula (i. e., $\delta\to 0$) is designated as the zero order or 0th approximation. The results for including the first and second curvature corrections are designated as first- and second-order approximation, respectively. Finally, the field strengths obtained from the residue series are shown for comparison and designated by "Res." In this latter case many terms of the series were required, and it is reassuring to notice that curvature corrected flat-earth formulas merge with the residue-series formula. The results of these calculations would lend confidence to the use of eq (40) for stratified media if the

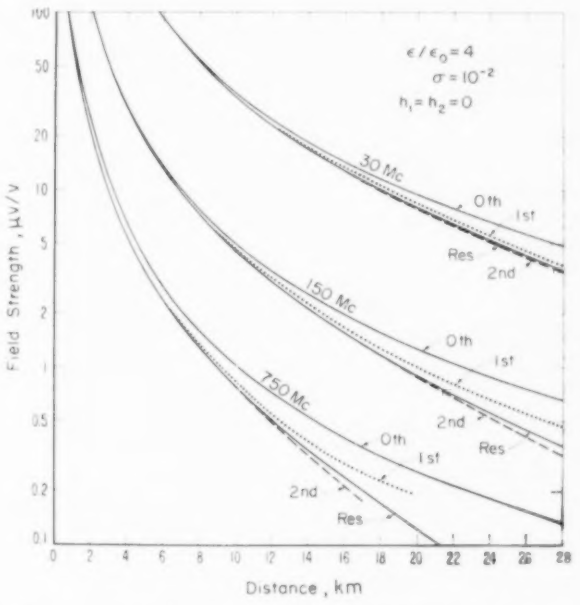

FIGURE 2. *Field-strength versus distance curves for a transmitter that radiates 1 kilowatt.*

The flat-earth and curvature corrected curves are shown along with the residue series-calculated curve.

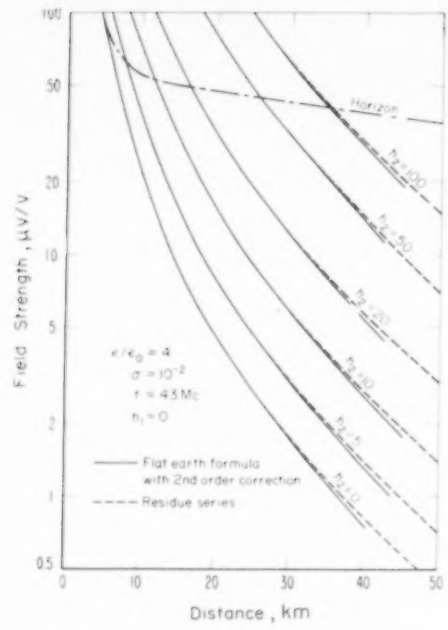

FIGURE 3. *Field-strength versus distance curves for various receiving-antenna heights.*

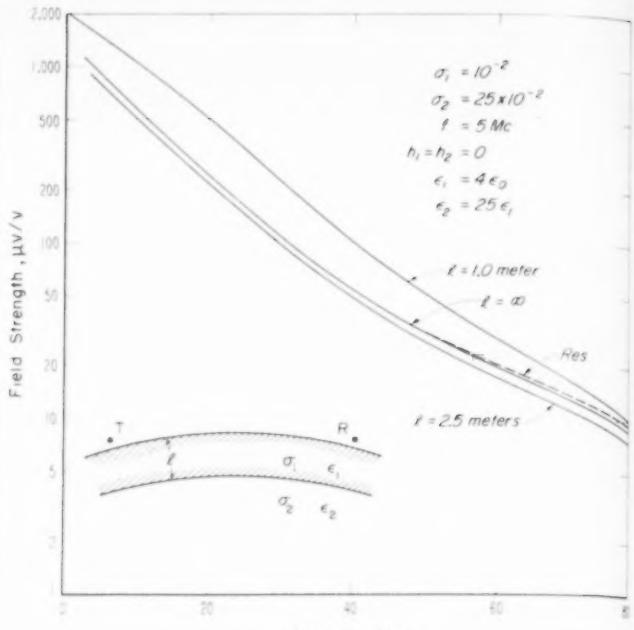

FIGURE 4. *Example of the field-strength–distance curves for a two-layer stratified ground for several values of the thickness of the upper stratum.*

appropriate value of the numerical distance ρ and curvature parameter δ are employed. As a further check on the curvature corrected formula used in conjunction with the height-gain function, calculations are carried out for various receiver heights h_2 with the transmitter height h_1 equal to zero. These results are shown in figure 3 for a frequency of 43 Mc, relative dielectric constant of 4, conductivity of 10^{-2}, and h_2=0, 5, 10, 20, 50, and 100 m. The solid curves correspond to the second-order curvature corrected flat-earth formula, whereas the dashed curves are based on the cumbersome but more exact residue series [4]. As a matter of interest, the line corresponding to the optical horizon is shown. It is apparent that the agreement between the two methods of calculation is very good at moderate ranges. No doubt a third-order correction involving a term proportional to δ^9 would improve the discrepancy at greater ranges. It is doubtful, however, if calculations of higher order correction terms are justified because the residue series becemes more convenient at larger ranges.

The computations for stratified ground are somewhat more involved, and, furthermore, even for a two-layer ground, additional parameters to be considered are conductivity σ_2 and dielectric constant ϵ_2 of lower stratum, and thickness l of upper stratum. As an example, the lower medium is taken to be 25 times better conducting than the upper stratum. For convenience, the dielectric constants are also taken to be in the same ratio. The second-order curvature corrected results for a frequency of 5 Mc is shown in figure 4, where the case $l=\infty$ corresponds to a homogeneous ground of electric constants σ_1 and

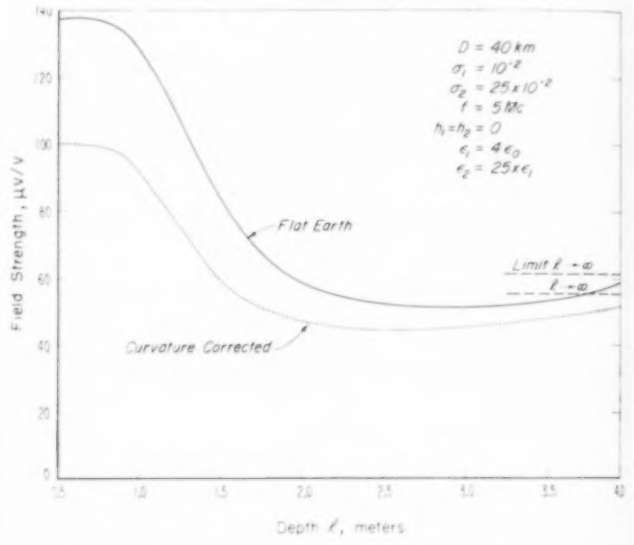

FIGURE 5. *Field strength at a distance of 40 kilometers on a two-layer stratified ground as a function of the thickness of the upper stratum.*

ϵ_1. The curve marked Res. corresponds to the residue series calculation for the homogeneous earth. If the thickness of the upper stratum is greater than about 2.5 m, the field corresponds quite closely to that expected over a homogeneous ground. To show in a little more detail, the nature of the dependence on stratification, the field at 40 km is shown plotted in figure 5 as a function of l in meters. Both the flat-earth and the second-order curvature corrected results are included.

4. Concluding Remarks

It is apparent that the theory of Watson [3], Bremmer [4], and others, for propagation of radio waves over a spherical homogeneous earth can be generalized to propagation over a concentrically stratified sphere. The derivation in this paper is very straightforward as a result of choosing an approximate boundary condition, which specifies the surface impedance at the surface of the sphere. Although the theory was developed for a homogeneous atmosphere, there is little reason to doubt that a similar analysis can be carried out for an inhomogeneous atmosphere following the development of Friedman [6]. For the case of normal refraction (absence of ducting), the results in the present paper can be employed directly by admitting the concept of the effective earth radius [4], where a_1 is replaced by a modified value a_1^e.

While the attention here has been mainly confined to propagation of radio waves over a stratified sphere, the results are applicable to the study of surface waves on corrugated spherical surfaces of the type that can be characterized by a surface impedance.

5. Appendix 1. Surface Impedance of a Stratified Conducting Sphere

The surface impedance at the surface of a sphere of radius a_1 consisting of a concentric core of radius a_2 will be derived. The propagation constants of the outer shell and the core are γ_1 and γ_2, respectively, and the intrinsic impedances are η_1 and η_2, respectively. Under the assumption that the source is a vertical antenna the field can be represented as a superposition of transverse magnetic (TM) spherical waves of order n. The surface impedance Z^n for such a TM wave is defined by

$$Z^n=[-E_\theta^n/H_\phi^n]_{r=a_1}. \tag{42}$$

The medium between the limits $r=a_1$ and a_2 can now be regarded as a nonuniform transmission line [13] of length $l=a_1-a_2$. The characteristic impedance of the line looking inward is

$$\eta_1\frac{\hat{I}_n'(\gamma_1 r)}{\hat{I}_n(\gamma_1 r)}=M(\gamma_1 r), \tag{43}$$

where $\hat{I}_n$ is Schelkunoff's notation for modified spherical Bessel functions of order n, and the prime indicates a differentiation with respect to the argument $\gamma_1 r$. Similarly, the characteristic impedance looking outward is

$$-\eta_1\frac{\hat{K}_n'(\gamma_1 r)}{\hat{K}_n(\gamma_2 r)}=N(\gamma_1 r), \tag{44}$$

where $\hat{K}_n$ is the modified spherical Hankel function of order n. The line is considered to be terminated by an impedance

$$\left[\eta_2\frac{\hat{I}_n'(\gamma_2 r)}{\hat{I}_n(\gamma_2 r)}\right]_{r=a_2}=P(\gamma_2 a_2). \tag{45}$$

From the theory of nonuniform transmission lines it follows that

$$Z^n=M(a_1)\frac{1+q_e(a_2)A_eB_e}{1+q_h(a_2)A_hB_h}, \tag{46}$$

where q_e and q_h are reflection coefficients at $r=a_2$ for the E_θ^n and H_ϕ^n field components and are given by

$$q_e=\frac{1/P(a_2)-1/M(a_2)}{1/P(a_2)+1/N(a_2)} \tag{47}$$

and

$$q_h=\frac{P(a_2)-M(a_2)}{P(a_2)+N(a_2)} \tag{48}$$

The quantities A and B are transmission factors given by

$$\left.\begin{aligned} A_e&=\frac{a_1\hat{I}_n'(\gamma_1 a_2)}{a_2\hat{I}_n'(\gamma_1 a_1)}, & B_e&=\frac{a_2\hat{K}_n'(\gamma_1 a_1)}{a_1\hat{K}_n'(\gamma_1 a_2)}\\ A_h&=\frac{a_1\hat{I}_n(\gamma_1 a_2)}{a_2\hat{I}_n(\gamma_1 a_1)}, & B_h&=\frac{a_2\hat{K}_n(\gamma_1 a)}{a_1\hat{K}_n(\gamma_1 a)}. \end{aligned}\right\} \tag{49}$$

Under the restriction that the thickness of the shell ($l=a_2-a_1$) is small compared to a_1, the above formulas can be greatly simplified. For example, noting that $I_n(x)$ satisfies the equation

$$\frac{d^2\hat{I}_n(x)}{dx^2}=\left[1+\frac{n(n+1)}{x^2}\right]\hat{I}_n(x), \tag{50}$$

it readily follows that the function $M(x)$ satisfies

$$\left\{M^2(x)+\eta_1\frac{dM(x)}{dx}=\left[1+\frac{n(n+1)}{x^2}\right]\eta_1^2\right\}x=\gamma_1 r. \tag{51}$$

A good approximate solution is

$$M(\gamma_1 r)\simeq\eta_1\left[1+\frac{n(n+1)}{(\gamma_1 r)^2}\right]^{1/2}, \tag{52}$$

because dM/dx is small when $|\gamma_1 r|\gg 1$. Now the values of n are not known precisely, but the important ones correspond to the roots ν_s, which are close to the value ka_1. It therefore follows that

$$M(\gamma_1 r)\simeq\eta_1\left[1+\frac{ka_1(ka_1+1)}{(\gamma_1 r)^2}\right]^{1/2}\simeq\eta\left[1-\frac{\gamma_0^2}{\gamma_1^2}\right]^{1/2}, \tag{53}$$

since $k=i\gamma_0$, $ka_1\gg 1$ and $a_1/r\simeq 1$ in the range $a_2\leq r\leq a_1$. With similar reasoning it follows that

$$N(\gamma_1 r)\simeq\eta_1\left[1-\frac{\gamma_0^2}{\gamma_1^2}\right]^{1/2} \quad \text{for} \quad a\leq r\leq a \tag{54}$$

and

$$P(\gamma_2 a_2)\simeq\eta_2\left[1-\frac{\gamma_0^2}{\gamma_2^2}\right]^{1/2}. \tag{55}$$

The transmission factors are then written

$$A_e\simeq A_h\simeq B_e\simeq B_h\simeq e^{-(\gamma_1^2-\gamma_0^2)^{1/2}l} \tag{56}$$

with $l=a_1-a_2$. The surface impedance then takes the form

$$Z^s\simeq\eta_1\left[1-\frac{\gamma_0^2}{\gamma_1^2}\right]^{1/2}\frac{\dfrac{\gamma_1^2}{\gamma_2^2}\left[\dfrac{\gamma_2^2-\gamma_0^2}{\gamma_1^2-\gamma_0^2}\right]^{1/2}+\tanh\left[(\gamma_1^2-\gamma_0^2)^{1/2}l\right]}{1+\dfrac{\gamma_1^2}{\gamma_2^2}\left[\dfrac{\gamma_2^2-\gamma_0^2}{\gamma_1^2-\gamma_0^2}\right]^{1/2}\tanh\left[(\gamma_1^2-\gamma_0^2)^{1/2}l\right]}. \tag{57}$$

It is to be noted that Z^s is precisely the ratio Z of the tangential electric and magnetic fields for a vertically polarized wave at grazing incidence on a two-layer stratified ground [5]. It, therefore, seems justified to employ the approximate boundary eq (7) at least for application to propagation of radio waves over the surface of a stratified ground with the normal earth curvature.

6. Appendix 2. Alternative Approach to the Height-Gain Function

It is possible to study the effect of raising the receiver and/or the transmitter by starting with a more accurate representation for the height-gain function:

$$f(p,h_i)=\frac{h_\nu^{(2)}(kr)}{h_\nu^{(2)}(ka)},$$

where

$$\nu=ka+(ka)^{1/3}\left[-\frac{p}{2\delta^2}\right] \tag{58}$$

with $r=h_i+a$; $f(p,h_i)$ is now expanded in a MacLaurin series as follows:

$$f(p,h)=1+kh_i\left[\frac{\dfrac{d}{dx}h_\nu^{(2)}(x)}{h_\nu^{(2)}(x)}\right]_{x=ka}+\frac{k^2h_i^2}{2}\left[\frac{\dfrac{d^2}{dx^2}h_\nu^{(2)}(x)}{h_\nu^{(2)}(x)}\right]_{x=ka}+\cdots \tag{59}$$

Now employing the relation

$$\frac{1}{x}\frac{d}{dx}\log xh_\nu^{(2)}(x)\simeq\frac{i\Delta}{x} \tag{60}$$

and the differential equation

$$\frac{d^2}{dx^2}+\frac{2}{x}\frac{d}{dx}+\left[1-\frac{\nu(\nu+1)}{x^2}\right]h_\nu^{(2)}(x)=0, \tag{61}$$

it follows that

$$f(p,h_i)\simeq 1+\left(i\Delta kh_i+\frac{h_i}{a}\right)-\frac{i\Delta k^2h_i^2}{ka}+\frac{k^2h_i^2\Delta}{2}. \tag{62}$$

It then follows that a more representative height-gain function $G'(\rho)$ in place of the function G is given by the operator

$$G'(\rho)\simeq 1+ikh_i\Delta-i\frac{k^2h_i^2\Delta}{ka}+\frac{k^2h_i^2\Delta}{2}\frac{\partial}{\partial\rho}+\cdots \tag{63}$$

The field $E(\rho,h)$ is then related to the field $E(\rho,0)$ on the ground by $E(\rho,h)=G'(\rho)E(\rho,0)$. The third term of the expansion is negligible when $kh<(ka)^{1/3}$ because $|\Delta|$ is somewhat less than unity and the fourth term is negligible when

$$kh_i^2/D\ll 1.$$

The function $G'(\rho)$ to this approximation is then identical to the height-gain function G obtained earlier.

7. References

[1] J. R. Wait, Radiation from a vertical dipole over a (plane) stratified ground, Trans. Inst. Radio Engrs. **AP-1,** 9 (1953); **AP-2,** 144 (1954).

[2] J. R. Wait, Theory of electromagnetic surface waves over geological conductors, Geofis. pura e appl. **28,** 47 (1954).

[3] G. N. Watson, The diffraction of radio waves by the earth, Proc. Roy. Soc. (London) [A] **95,** 546 (1919).

[4] H. Bremmer, Terrestrial radio waves (Elsevier Publishing Co., 1949).

[5] J. R. Wait, Propagation of radio waves over a stratified ground, Geophysics **18,** 416 (1953).

[6] B. F. Freidman, Propagation in a non-homogeneous atmosphere, in Theory of electromagnetic waves (Interscience Publishers, New York, N. Y., 1951).

[7] R. S. Elliott, Spherical surface wave antennas. Paper presented at URSI Symposium on Electromagnetic Theory at Ann Arbor, Mich. (to be published in Trans. Inst. Radio Engrs.).

[8] H. J. Josephs, Heaviside's electric circuit theory (Methuen & Co. Ltd., London, 1946).

[9] G. A. Campbell and R. M. Foster, Fourier integrals for practical application, p. 92, No. 811 (1948).

[10] K. A. Norton, The calculation of the ground wave field intensity, Proc. Inst. Radio Engrs. **29,** 723 (1941).

[11] A. N. Sommerfeld, Uber die Ausbreitung der Wellen in der drachtlosen Telegraphie, Ann. Physik **81,** 1135 (1926).

[12] G. A. Hufford, An integral equation approach to the problem of wave propagation over an irregular surface, Quart. Appl. Math. **9,** 391 (1952).

[13] S. A. Schelkunoff, Electromagnetic waves (Van Nostrand Co., Inc., New York, N. Y., 1943).

BOULDER, August 30, 1955.

Recent Publications of the National Bureau of Standards

Journal of Research of the National Bureau of Standards, volume **56**, No. 2, February 1956 (RP2648 to RP2655 incl.). Annual subscription $4.00.

Technical News Bulletin, volume **40**, No. 2, February 1956. 10 cents. Annual subscription $1.00.

Basic Radio Propagation Predictions for May 1956. Three months in advance. CRPL 138. Issued February 1956. 10 cents. Annual subscription $1.00.

Research Papers

Journal of Research, volume 56, number 2, February 1956. Single copies of the Journal vary in price. Single copies of Research Papers appearing in the Journal are not available for sale. The Superintendent of Documents, U. S. Government Printing Office, Washington 25, D. C., will reprint 100 or more copies of a Research Paper. Request for the purchase price should be mailed promptly to that office.

RP2648. Residual entropy of linear polymers. H. N. V. Temperley.

RP2649. Molecular weights of thermally degraded polymethyl methacrylate. Victor Hart.

RP2650. Thermal expansion of binary alkaline-earth glasses. Herman F. Shermer.

RP2651. Dielectric relaxation for a three-dimensional rotator in a crystalline field: theory for a general six-site model. Benjamin M. Axilrod.

RP2652. A matrix with real characteristic roots. Karl Goldberg.

RP2653. Reflection and transmission of gamma radiation by barriers: semianalytic Monte Carlo calculation. Martin J. Berger and John Doggett.

RP2654. An examination of the helium vapor pressure scale of temperature using a magnetic thermometer. E. Ambler and R. P. Hudson.

RP2655. Calculation of thermodynamic functions for polyatomic molecules. Harold W. Woolley.

Miscellaneous Publications

M217. Annual report 1955. 55 cents.

Circulars

C562. Bibliography of research on deuterium and tritium compounds 1945 to 1952. Lawrence M. Brown, Abraham S. Friedman, and Charles W. Beckett. 50 cents.

C564. Tables of thermal properties of gases. Joseph Hilsenrath, Charles W. Beckett, William S. Benedict, Lilla Fano, Harold J. Hoge, Joseph F. Masi, Ralph L. Nuttall, Yeram S. Touloukian, Harold W. Woolley. $3.75.

C567. Guide to instrumentation literature. W. G. Brombacher, Julian F. Smith, and Lyman M. Van der Pyl. 75 cents.

Publications in Other Journals

Reference samples of isotopic abundance. Fred L. Mohler. Science (1515 Massachusetts Ave. NW., Washington 5, D. C.) **122**, No. 1364, 334 (Aug. 1955).

Specific heats of collagen and leather. Joseph R. Kanagy. J. Am. Leather Chemists' Assoc. (Dept. of Leather Research, Univ. of Cincinnati, Cincinnati 1, Ohio) **50**, No. 10, 444 (Sept. 1955).

Textiles at the National Bureau of Standards. W. D. Appel. Proc. Am. Assoc. Textile Chemists Colorists (44 E. 23d St., New York 10, N. Y.) **44**, No. 23, 795 (Nov. 1955).

Ultrasonic switch aids diversity reception. G. Franklin Montgomery. Electronics (330 W. 42d St., New York 36, N. Y.) **28**, 169 (Nov. 1955).

Geometric factors in electrical measurements relating to corrosion and its prevention. W. J. Schwerdtfeger and Irving A. Denison. Corrosion (1061 M & M Building, Houston 2, Texas) **2**, 25 (Oct. 1955).

Compressibility of binary alkali borate and silicate glasses at high pressures. C. E. Weir and L. Shartsis. J. Am. Ceram. Soc. (2525 N. High St., Columbus 2, Ohio) **38**, No. 9, 299 (Sept. 1955).

Mechanisms of alkali-aggregate reaction. Robert G. Pike, Donald Hubbard, and Herbert Insley. J. Am. Concrete Inst. (18263 W. McNichols Rd., Detroit 19, Mich.) **27**, No. 1, 13 (Sept. 1955).

Variability of wool content in part wool blankets. Emanuel Horowitz and W. S. Connor. ASTM Bulletin (1916 Race St., Philadelphia 3, Pa.) No. 208, 42 (Sept. 1955).

Determination of sulfur in rubber vulcanizates. E. W. Zimmerman, V. E. Hart, and Emanuel Horowitz. Anal. Chem. (1155 16th St. NW., Washington 6, D. C.) **27**, No. 10, 1606 (Oct. 1955).

Publications for which a price is indicated are available only from the Superintendent of Documents, U. S. Government Printing Office, Washington 25, D. C. (foreign postage, one-third additional). Reprints from outside journals are not available from the National Bureau of Standards but can often be obtained from the publishers.

UNITED STATES
GOVERNMENT PRINTING OFFICE
DIVISION OF PUBLIC DOCUMENTS
WASHINGTON 25, D. C.

OFFICIAL BUSINESS

PENALTY FOR PRIVATE USE TO AVOID PAYMENT OF POSTAGE, $300 (GPO)

Journal of Research of the National Bureau of Standards Vol. 56, No. 4 April 1956

Contents

		Page
New descriptions and analyses of the third and fourth spectra of zirconium, Zr III and Zr IV. C. C. Kiess.	RP2663	167
Frequency conversion with positive nonlinear resistors. Chester H. Page.	RP2664	179
Electrical resistivity of vitreous ternary lithium sodium silicates. Simon W. Strauss.	RP2665	183
Isothermal compressibilities of alkaline earth oxides at 21° C. C. E. Weir.	RP2666	187
Improved synthesis of sodium D-glucuronate-6-C^{14} and of D-glucose-6-C^{14}. R. Schaffer and H. S. Isbell.	RP2667	191
Ideal gas thermodynamic functions of the isotopic hydrogen cyanides. Joe C. Bradley, Lester Haar, and Abraham S. Friedman.	RP2668	197
Surge voltage breakdown of air in a nonuniform field. J. H. Park and H. N. Cones.	RP2669	201
Index of refraction and particle size as factors in the infrared spectrophotometry of polyvinyl chloride. Mary Reiney Harvey, James E. Stewart, and Bernard G. Achhammer.	RP2670	225
Radiation from a vertical antenna over a curved stratified ground. James R. Wait.	RP2671	237

Single copies of the above Research Papers are not available for sale, but the Superintendent of Documents, U. S. Government Printing Office, Washington 25, D. C., will reprint 100 or more copies, and request for the purchase price should be mailed promptly to that Office.

[A list of recent NBS publications is given on page 3 of the cover.]

For sale by the Superintendent of Documents, U. S. Government Printing Office, Washington 25, D. C. Price 60¢ (single copy). Subscription price: $4.00 a year; $1.25 additional for foreign mailing. Single copies vary in price.

UNITED STATES GOVERNMENT PRINTING OFFICE, WASHINGTON : 1956